Development of a Novel Fiber-Reinforced Composite Utility Pole

by

Qianjiang Wu

Submitted in partial fulfilment of the requirements

for the degree of Master of Applied Science

at

Dalhousie University

Halifax, Nova Scotia

May 2023

Table of Contents

List of Tables

List of Figures

Abstract

The objective of the project outlined in this thesis is to develop a novel utility pole with comparable performance to commercially available fiber-reinforced polymer (FRP) poles. The novel pole is made of 3D E-glass-fabric-epoxy composite reinforced with wood dowels, referred to as wood dowel-reinforced 3D hybrid composite (WC3DFRP). The compressive and flexural properties of WC3DFRP are evaluated. Two WC3DFRP and two 2D FRP poles are fabricated using hand layup method. The poles are tested as per the standard and their responses are compared.

Additionally, robust finite element models are developed in the LS-DYNA environment and calibrated based on the experimental results.

Finally, a simplified analytical calculation method is developed so practicing engineers could determine the stiffness of WC3DFRP poles accurately and quickly.

The results demonstrate the superiority of the developed 3D pole over the conventional 2D poles. Additionally, numerical simulation results agree with the experimental results very closely.

List of Abbreviations and symbols Used

3DFGF	Three-dimensional fiberglass fabric
ABS	Acrylonitrile butadiene styrene
CAD	Computer-aided design
CLC	Combined loading compression
CTE	Coefficient of thermal expansion
CZM	Cohesive zone model
Exp	Experimental
FE	Finite Element
FEM	Finite element method
FRP	Fiber-reinforced polymers
GFRP	Glass fiber reinforced polymers
GRG	Generalized Reduced Gradient
ID	Identification
LVDT	Linear variable differential transformer
MS	Microsoft
OD	Outside diameter
OPT	Optimization
PVA	Polyvinyl alcohol

PVC	Polyvinyl chloride
SRI	Selective reduced-integrated
Tshell	Thick Shell
UD	Unidirectional
WC3DFRP	Wood dowel-reinforced 3D hybrid composite
A	The average cross-sectional area of the top and bottom areas of the pole
$A_{i,j}$	Extensional stiffness matrix with matrix indices i and j
$A_{Ply}, A_{Pillar}, A_{Dowel}, A_{Air}$	Cross-sectional areas of ply, pillar, dowel and empty channel, respectively.
a	Length measured from constrain to load point
$A_{i,j}$	Extensional stiffness matrix
$B_{i,j}f$	Coupling stiffness matrix
$D_{i,j}$	Bending stiffness matrix
D_i, D_o	Inside and outside diameters of the cross-section of poles
D_B, D_T	Outer diameters at the bottom and top of poles
d_B, d_T	Inner diameters at the bottom and top of poles
E	Elastic modulus
E_c	Compressive modulus

E_{Ply} , E_{Pillar} , E_{Dowel}, E_{Air}	Elastic modulus of ply, pillar, dowel and air in principal material direction (1-direction), respectively
$E_{f.}$	Flexural modulus
E^{f}	Estimated flexural modulus
E_{ij}	Elastic moduli terms i and j.
E_L,E_T	Elastic modulus of wood in the longitudinal and tangential directions
E_x	Effective elastic modulus of laminate
$E_{3D,x}$, $E_{3D,1}$	Estimated effective elastic modulus of 3D poles in the global x-axis and material principal direction 1.
F	Load (force)
FL	Failure
$F_{1,\lambda}$, $F_{2,\lambda}$ and $F_{12,\lambda}$	Failure strengths in tension, compression and shear
F^{cu}	Estimated ultimate compressive strength
G_{12}, G_{23},G_{31}	Shear moduli
G_{LT}, G_{LR}	Shear moduli in material 1,2 and 1,3 directions
G_{xz}	Estimated through-thickness shear modulus
h	Estimated coupon's thickness
I	Area moment of inertia
K	Effective length factor

l_g	Coupon's gauge length in the compression test
L_f	Supported span length in three-point bending test
m	Cosine of the transformed angle
M_{max}	Maximum bending moment
n	Sine of the transformed angle
P_{ult}	Ultimate load
Q_{ij}	Components i, j of stiffness matrix of lamina.
Q_{ij}^{k}	Components i, j of the stiffness matrix of the lamina of the k_{th} layer of laminate
D_B, D_T	Pole's top and bottom diameters
r	Radius of gyration
R_x, R_y, R_z	Rotational degrees of freedom
S	Slenderness ratio
$S_{21}, S_{12}, S_{31}, S_{32}$	In-plane and out-of-plane shear strengths
t	Thickness
U_x, U_y, U_z	Translational degrees of freedom
V	Volume
V_{NP}	The volume of the non-prismatic 2D poles
V_p	The volume of the prismatic 2D poles

w	Coupon's width
$X_C.X_T$	Compression and tension strengths of lamina along the fiber direction
Y_C,Y_T	Compression and tension strengths of lamina transverse to fiber direction
Z_C, Z_T	Through-thickness compression and tension strengths of the lamina
ε	Strain
ε^0	mid-plane strains
σ	Stress
σ_{max}	Maximum stress
σ_{ult}	Ultimate strength
σ_λ	Applied stress in tension or compression
ν_{12}, ν_{21}	In-plane Poisson's ratios
τ_{12}	In-plane shear stress
γ_{12}	In-plane shear stain
θ	Fiber angle in degree
δ_{max}	Maximum deflection
δ_f	Flexural deflection
ρ	Material density
κ	Mid-plane curvatures

z_k	Through-thickness coordinate of layer k of a laminate measured from the mid-plane of the laminate

Acknowledgement

I would like to thank all those who helped and contributed to completing this thesis.

First and foremost, I would like to express my sincere appreciation to my academic supervisor, Dr. Farid Taheri, for his guidance, encouragement, and support throughout my entire master's program. His expertise, industrial experiences and dedication to his craft were instrumental in shaping this thesis into its final form.

Second, I would like to extend my appreciation to the members of my thesis committee, Dr. Jarjoura and Dr. El Naggar, for their time, effort and constructive suggestions. Their suggestions have been incredibly valuable in improving the quality of my thesis.

Third, I would like to express my gratitude to all the technicians who helped in the experimental part of my project, particularly Mark Leblanc, Brian Kennedy, Peter Jone, Jonathan MacDonald and Jesse Keane.

I would also like to acknowledge the opportunity and financial support provided by Mitacs (through their Accelerate program) and our industrial partner, Sonideft Inc.

I am very grateful to my parents, who have supported me financially and emotionally since the beginning of my studying in Canada. My fiancée, Jia Yu, helped and supported me in my experiments in accomplishing this milestone in my life.

Finally, I wish to thank all my colleagues, especially Mr. Ke Wang and Dr. Elnaz Mottaghian, for supporting and helping me with my thesis.

Without the help and support of these individuals, this thesis would not have been possible.

Chapter 1: Introductions

1.1. Background

The first recorded utility poles were constructed from wood for transmitting telegraphs in 1844 in Washington, D.C.(North American Wood Pole Council, n.d.). According to Mankowski et al. (2002), the number of wood utility poles in the US was estimated to range between 160 million to 180 million, with southern pine, Douglas-fir and western redcedar being the most used species of wood for pole construction. Wood also has the lowest cost compared with steel and concrete. Besides, trees are renewable resources and absorb carbon dioxide when grown. Concrete and steel are also commonly used materials for utility poles. Concrete utility poles are strong and have good resistance to natural erosions and rots. However, their drawbacks include comparatively heavier weight and higher cost, which have made them not so popular in North America. Steel poles are about 50% to 70% lighter than comparable wood poles (Love et al., 2021). Besides, the steel poles are 100% recyclable(Love et al., 2021). The disadvantages of steel poles are their comparatively higher cost and vulnerability to corrosion (Love et al., 2021).

Fiber-reinforced polymer composites (FRPs) are materials that consist of two or more different materials, consisting of strong and stiffer reinforcing fibers and less stiff and weaker matrix. Some of the commonly used fiber materials are E- and S-Glass, carbon and aramid. Epoxy and polyester are the commonly used matrix materials. FRPs have a wide range of applications in civilian to military industries, including but not limited to ships, airplanes, automobiles and wind turbine blades. Most FRP applications utilize a laminated structure, consisting of two or multiple layers of 2D FRP. One layer of FRP is called a lamina or a ply. Figure 1-1 shows the formation of a laminate from fibers and matrix.

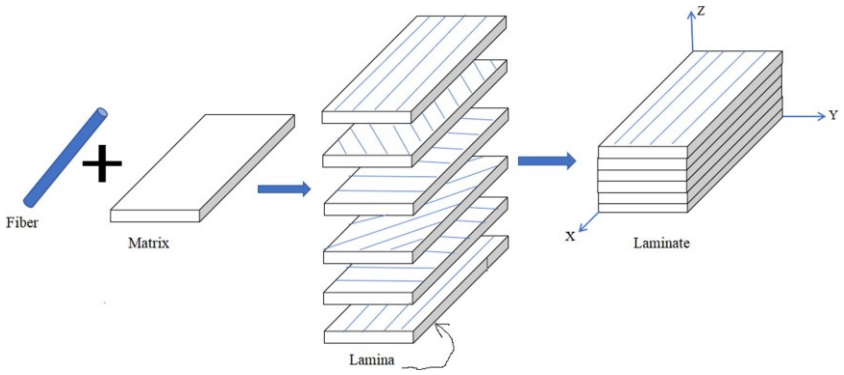

Figure 1-1 Schematic representation of the formation of a laminate (Mognhod et al., 2021).

Glass fiber reinforced polymers (GFRP), the most widely used composite in various industries, are also used for manufacturing FRP utility poles because of their lower cost compared to other types of FRPs(EL-Fiky et al., 2022). The first application of GFRP was in marine boats in the early 1940s(Palucka & Bensaude-Vincent, 2002). Twenty years later, the first utility pole made of GFRP was installed in Hawaii (Love et al., 2021). The pole lasted about 50 years before being removed due to U.V. exposure degradation (Love et al., 2021).

In Canada, FRP pole design has been adopted in CSA C22.3 - Overhead Systems, (CSA, 2020). The development of FRP poles in the US could be based on the standard ACMA/UCSC UP01-18-2019 produced by the American National Standards Institute (ANSI) or Engineering Practice NO.104 by the American Society of Civil Engineers (ASCE) (ANSI, 2019; ASCE, 2019). Due to the lower popularity of concrete and steel poles compared to wood poles in North America, the scope of discussion is limited to wood and FRP poles in the following sections of this chapter.

1.2. Advantages of FRP Poles

Wood utility poles are vulnerable to decay when subjected to severe weather conditions. In May 2022, Hydro One (previous Ontario Hydro) and Hydro-Québec lost about 1900 and 1125 wood poles, respectively due to a series of windstorms (McClearn, 2023). In September of the same year, Nova Scotia Power claimed they had to remove more than 2000 damaged wood poles due to Hurricane Fiona (McClearn, 2023). The

damaged poles caused a power outage in about 525,000 homes and businesses across Nova Scotia (MacDonald & Alam, 2022).

In addition to natural disasters, wood poles may fail due to the natural decay of the wood material. Morrell et al. (2007) concluded based on their survey that in a total of 52,375 removed wood poles for all causes annually in the Pacific Northwest, more than half of them (56%) were removed due to the decay. The agents that cause the decay of wood poles include ultraviolet light, insects, and decay fungi, which become more problematic when the poles are within a humid environment (Morrell (2012). Therefore, decay occurs especially faster in poles installed along the coastal lines because of the combined effect of high humidity and frequent rainfall, which help the fungal enzymes attack the poles. Figure 1-2 shows the rotted part of a wood pole underneath the groundline due to the fungi attack.

Figure 1-2 A wood pole rotted below the groundline due to the fungi attack (Jackson, 2012).

In contrast, FRP poles are much less affected by material decay due to their inherent nature. Nowadays, the expected service life of GFRP poles which have been treated with UV and fire inhibitors has been estimated to be over 80 years (Love et al., 2021). The expected service life of wood poles ranges between 40 to 56.8 years (Rey & Morrell, 2016).

Besides, wood poles require inspection and maintenance once every 10 years compared with a meagre amount of maintenance required for FRP poles. An industry-leading composite pole manufacturer, R.S. Technology Inc., claims no maintenance is required in the 120-year life cycle of their poles (R.S. Technologies Inc., n.d.).

The classification standard (e.g., transmission, distribution, and light/illumination) for wood poles in Canada is specified in the National Standard of Canada CSA-015 (CSA, 2015). However, there exists no such standard for FRP poles. Due to the difference in the material responses of wood and FRP, FRP pole manufacturers can adjust their pole dimensions to accommodate the specific loading designated for each class of wood poles (ASCE, 2019). Owing to the high specific strength of GFRP, a class 1 wood pole is about three times heavier compared to an equivalent GFRP pole, as claimed by R.S. Technologies Inc. (n.d.).

GFRP poles from R.S. Technologies Inc. are designed modularly, bringing various advantages over the wood and traditional monolithic GFRP poles. The modular system allows more feasible transportation since modules can be transported in a nested configuration, as seen in Figure 1-3. Besides, modular poles with different sizes can be combined to have various overall lengths and rigidity to meet different applications (e.g., for power transmission and distribution). Moreover, in an event of a catastrophic failure of a modular pole, only the failed module(s) would need to be replaced instead of the entire pole.

Figure 1-3 Transportation of the nested 38.1m modular poles (ASCE, 2019).

1.3. Manufacturing Methods of FRP Utility Poles

1.3.1. Pultrusion

The pultrusion manufacturing method is one of the commonly used methods for manufacturing FRP poles in the industry because it is a highly automated process with a fast production rate. In this process, fiber yarns are pulled from the yarn creels to a resin bath through a yarn guide. Sometimes, multidirectional mats or fiber cloths are added to improve the multidirectional strengths, as seen in Figure 1-4. Subsequently, the resin-impregnated fibers are taken into a die to shape into a desired cross-section. The die is also heated to expedite the cure period of the resin upon the forming process. Consequently, the resin is fully solidified when the impregnated fibers leave the die. Subsequently, the pultruded FRP is cut into the desired lengths. There is also another variation of the resin wetting system, in which the resin is directly injected into the die, producing more effectively consolidated pultruded sections. The limitations of pultrusion are that the pultruded article would be prismatic (i.e., with a constant cross-section), and is most suited for the fabrication of components that have unidirectionally (uniaxially) laid fibers. Hence, the FRP poles manufactured using this process have a prismatic shape and are not effective in taking multidirectional and complex loading states.

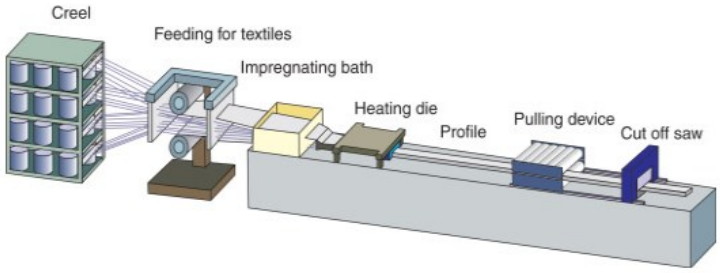

Figure 1-4 Schematic representation of the pultrusion process (Riedel, 2012).

1.3.2. Filament winding

Filament winding is the most commercially used manufacturing method for fabricating FRP poles. It is highly automated and can precisely lay fibers at the desired angle for each

layer. The mandrel's surface is first treated with a mold release compound so the filament wound part could be easily removed from the mandrel. Similar to pultrusion, fiber yarns are pulled from creels to a resin bath for impregnation. Then, the resin-impregnated fiber yarns are pulled through the bath and rolled on the mandrel through the payout eye (delivery point), as seen in Figure 1-5. As the mandrel rotates and the payout eye moves back and forth through the guide rail, the laminated structure is laid onto the mandrel. The FRP is extracted from the mandrel after it has been cured. The limitations of this manufacturing process are that the low fiber angles, from 0° to 15° and a uniform thickness of the final product are difficult to obtain (Mazumdar, 2002).

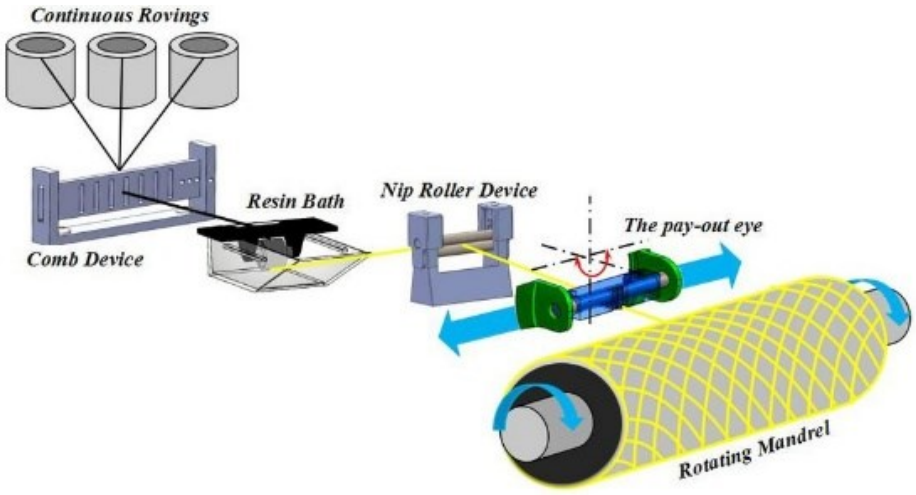

Figure 1-5 Schematic representation of the filament winding process (Ma et al., 2019).

1.4. Testing Methods of FRP Composite Utility Poles

Utility poles can be classified by their applications (e.g., transmission, distribution, and light/illumination). Transmission poles are used to draw high-voltage power from power plants to the transformer substations to reduce the voltage. Then, the reduced-voltage power is sent from the substations to consumers using the distribution poles. Although as mentioned in section 1.2. no standard exists for classifying FRP poles, CSA-Overhead Systems (2020) specifies that FRP poles could use the same minimum load factors as steel poles. The load factor multiplies the poles' applicable loads to obtain the

assumed load. The applicable loads could be the vertical load due to the pole's weight and the force due to the supporting attachments on the pole (e.g., guy wires and transmission wires, especially due to ice/snow accretion), transverse load due to wind pressure applied to the transmission cables and "longitudinal" load due to the tension changes of the transmission cables. Figure 1-6 illustrates the customary directions for describing utility poles' load directions.

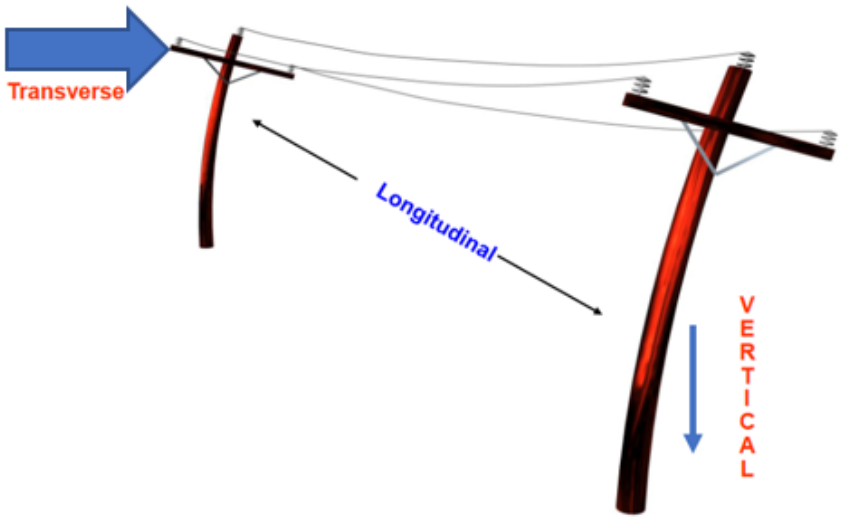

Figure 1-6 Illustration of the customary load directions for the utility poles (Murray & Sipler, n.d.).

The suggested testing methods for FRP poles include full-scale static flexural and dynamic tests, cross-sectional hoop tests, wall pull-through tests and more (see ASCE, 2019). A full-scale flexural test until the destruction is performed to validate the pole's stiffness and ultimate strength. This test follows the standard static test procedures for the wood poles as per ASTM D1036-99 (ASTM, 2017). According to the standard, the pole is constrained from its bottom end at a length equal to 10% of its total length plus 0.6 m (ASCE, 2019). Then a load is applied perpendicular to the pole at 0.6 m below the pole tip, and the deflection is measured at the tip (ASCE, 2019). Figure 1-7 illustrates a full-scale flexural test of an FRP pole.

Figure 1-7 Illustration of the full-scale flexural test of an FRP pole based on the ASTM D1036-99 (ASCE, 2019).

Mohamed (2000) conducted a fundamental investigation of the relationship between the GFRP poles' performances and their layup sequence using the flexural testing method. Various stacking sequences, including three laminations, one with all fibers laid in the longitudinal direction, fibers laid circumferentially and the combinations of the two directions were tested. The highest ultimate load-to-mass ratio achieved was 0.47 kN/kg using $[90/0_6/90]$ layup configuration (0: along the axial direction, and 90: along the hoop direction (Ibrahim, 2000).

1.5. 3D Glass Fabric

Currently, FRP poles are constructed using 2D laminates. Here, a novel design is established based on the incorporation of a recently developed 3D E-glass fabric in epoxy resin, a combination which has never been attempted by the utility pole industry. The 3D fabric as seen in Figure 1-8, consists of two plies of bidirectional woven fabrics, which are interwoven by vertical fibers (or pillars). The length of the pillars governs the space that is created between the two fabrics. In other words, once the entire fabric is impregnated by a resin, the pillars are awakened from their collapsed state, creating the specified gap between the two bidirectional fabrics. The fabric can be selected based on the desired gap

(i.e., between 2 to 21 mm). Due to the woven nature of pillars to fabric connection, the overall stiffness and interlaminar strength of the composite made of this 3D fabric are much improved compared with an equivalent 2D FRP laminate.

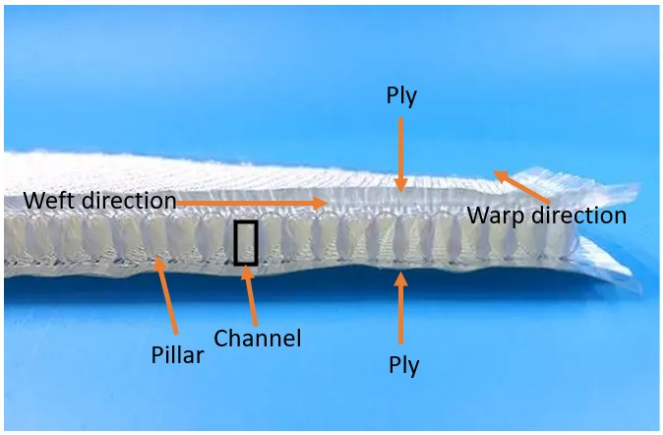

Figure 1-8 Illustration of component names in the 3D glass fabric (China Beihai Fiberglass Co., n.d.).

The hollow row of spaces created by the plies and pillars are referred to as channels in this thesis. The warp direction for the plies is along the channels perpendicular to the weft direction as shown in Figure 1-8. In developing WC3DFRP, wooden dowels are inserted into those empty channels prior to the impregnation of the cloth, thereby creating an even stiffener and stronger 3D hybrid composite material. The advantages of using wood were briefly discussed in section 1.1. The objective of this thesis is to evaluate the feasibility of using the developed 3D hybrid material for the fabrication of poles having stiffer responses compared with the 2D poles but with the same weight. Therefore, scaled 2D and 3D poles are designed and fabricated to assess the response of the proposed design against the latest commercially designed 2D modular poles. Finally, a simple equation is developed by which pole designers can estimate the equivalent stiffness of the suggested 3D poles.

Chapter 2: Introduction to Classical Lamination Theory

This chapter will introduce the background used to develop the calculations of the composite lamina and laminates used in this thesis. Besides, the singular type (i.e., the Maximum stress) and the interactive (Tsai-Hill) failure theories are also briefly described.

2.1. Macro-mechanics of the composite lamina

A fiber-reinforced plastic composite (FRP) lamina's principal material coordinate system is independent of the global coordinate system. In a unidirectional (UD) lamina, its principal material direction-1 is along the fibres, 2 is orthogonal to the fibres, and 3 is orthogonal to the plane of 1 and 2 (i.e., through-the-thickness), as illustrated in

Figure 2-1. Hence the principal material direction of a lamina can be varied across a laminate. The global coordinate system with x,y and z directions is used as a reference coordinate system for convenient calculation.

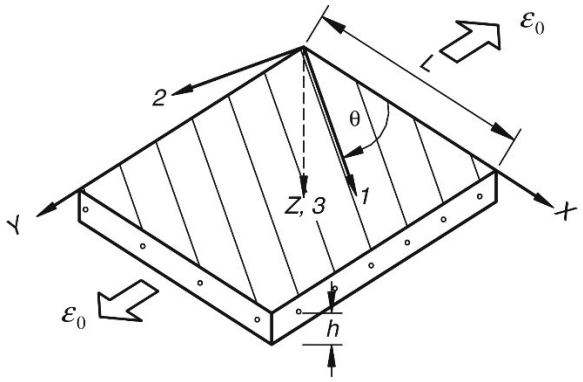

Figure 2-1 Illustration of a unidirectional lamina's principal material coordinate system in a global coordinate system (Ye & Zhang, 2012).

To assess the laminated composite's mechanical properties, each lamina within the lamination must be characterized first. The stress-strain relation of a thin lamina under plane stress is represented by Equation 2-1 (Daniel & Ishai, 2005).

$$\begin{Bmatrix}\sigma_{11}\\ \sigma_{22}\\ \tau_{12}\end{Bmatrix}=\begin{bmatrix}Q_{11} & Q_{12} & 0\\ Q_{12} & Q_{22} & 0\\ 0 & 0 & Q_{66}\end{bmatrix}\begin{Bmatrix}\varepsilon_{11}\\ \varepsilon_{22}\\ \gamma_{12}\end{Bmatrix} \quad \text{Equation 2-1}$$

where the σ_{11}, σ_{22} and ε_{11}, ε_{22} are the normal stresses and strains in principal material 1 and 2 directions; τ_{12} and γ_{12} are the in-plane shear stress and strain in material 1 and 2 directions, respectively and Q_{ij} is the stiffness component of the lamina, where i and j are the matrix entry indices (*i*=*j*= 1, 2, 6). The Q_{ij} terms can be calculated using the following relations using the lamina's engineering constants(Daniel & Ishai, 2005):

$$\begin{aligned} Q_{11} &= \frac{E_1}{1-v_{12}v_{21}}\\ Q_{22} &= \frac{E_2}{1-v_{12}v_{21}}\\ Q_{12} &= Q_{21} = \frac{v_{21}E_1}{1-v_{12}v_{21}} = \frac{v_{12}E_2}{1-v_{12}v_{21}}\\ Q_{66} &= G_{12} \end{aligned} \quad \text{Equation 2-2}$$

where the E_1 and E_2 are the elastic moduli of the lamina in principal material 1 and 2 directions, respectively, and G_{12} is the in-plane shear modulus of the material. The Poisson's ratio v_{12} represent the change in deformation in 2-direction under the applied loading in 1-direction and v_{21} would be in reverse, respectively. The value of v_{21} can be calculated using the following compatibility equation(Daniel & Ishai, 2005).

$$\frac{v_{12}}{E_1} = \frac{v_{21}}{E_2} \quad \text{Equation 2-3}$$

In cases when the directions of the applied loads do not align with the lamina's material axes, the stress-strain relation of the lamina can be transformed from the material axes to the loading (global) axes (x, y). Therefore, the stress-strain relationship after the transformation can be written as seen in Equation 2-4.

$$\begin{bmatrix}\sigma_x\\ \sigma_y\\ \tau_s\end{bmatrix} = \begin{bmatrix}Q_{xx} & Q_{xy} & 2Q_{xs}\\ Q_{yx} & Q_{yy} & 2Q_{ys}\\ Q_{sx} & Q_{sy} & 2Q_{ss}\end{bmatrix}\begin{bmatrix}\varepsilon_x\\ \varepsilon_y\\ \frac{1}{2}\gamma_s\end{bmatrix} \quad \text{Equation 2-4}$$

where τ_s and γ_s represent the in-plane shear stress and strain in the loading x-y axes, respectively. The terms of the transformed stiffness matrix in the global axis can be calculated using the following relationships:

$$\begin{aligned}
Q_{xx} &= m^4Q_{11} + n^4Q_{22} + 2m^2n^2Q_{12} + 4m^2n^2Q_{66}\\
Q_{yy} &= n^4Q_{11} + m^4Q_{22} + 2m^2n^2Q_{12} + 4m^2n^2Q_{66}\\
Q_{xy} &= m^2n^2Q_{11} + m^2n^2Q_{22} + (m^4 + n^4)Q_{12} - 4m^2n^2Q_{66}\\
Q_{xs} &= m^3nQ_{11} - mn^3Q_{22} - mn(m^2 - n^2)Q_{12} - 2mn(m^2 - n^2)Q_{66}\\
Q_{ys} &= mn^3Q_{11} - m^3nQ_{22} + mn(m^2 - n^2)Q_{12} + 2mn(m^2 - n^2)Q_{66}\\
Q_{ss} &= m^2n^2Q_{11} + m^2n^2Q_{22} - 2m^2n^2Q_{12} + (m^2 - n^2)^2Q_{66}
\end{aligned} \quad \text{Equation 2-5}$$

where m= cos θ and n = sin θ. The angle θ, as seen in

Figure 2-1, is measured counter-clockwise from the x-axial to the 1-axis (Daniel & Ishai, 2005).

2.2. Lamina failure theories

The maximum stress failure criterion is a limit theory, meaning that the material's failure depends on the applied stress to reach the failure strength in any primary or principal material direction. When a thin lamina is subjected to in-plane stresses that are not along the principal material axes, the stress would have to be transformed into the material axes before applying the failure criterion. The calculations of the criterion show the following:

$$\sigma_\lambda = \frac{F_{1,\lambda}}{\cos^2\theta}$$

$$\sigma_\lambda = \frac{F_{2,\lambda}}{sin^2\,\theta} \quad \text{Equation 2-6}$$

$$\sigma_\lambda = \frac{F_{12,\lambda}}{\sin\theta\cos\theta}$$

where σ is the applied stress, F_1, F_2 and F_{12} represent the failure strengths corresponding to the material axes 1 and 2 and notation λ is set either to tension, compression or in-plane shear.

An interactive theory predicts a material's failure based on its overall failure instead of comparing each stress component using one equation. Therefore, this failure theory will be used as a failure criterion for optimizing both the thickness and fiber angle of the lamina in this thesis. For a thin lamina, the Tais-Hill failure criterion is based on this theory, which can be represented by the following equation:

$$\frac{1}{F_\lambda^2} = \frac{m^4}{F_{1,\lambda}^2} + \frac{n^4}{F_{2,\lambda}^2} + \left[\frac{1}{F_{12,\lambda}^2} + \frac{1}{F_{1,\lambda}^2}\right] m^2 n^2 \qquad \text{Equation 2-7}$$

2.3. Macro-mechanics of composite laminates

The stiffness of a laminate is affected by the laminate's stacking sequence and the stiffness of each constituent lamina. In general, the resultant forces and moments in a laminate can be calculated by the following relationship (Daniel & Ishai, 2005):

$$\begin{bmatrix} N \\ M \end{bmatrix} = \begin{bmatrix} A & B \\ B & D \end{bmatrix} \begin{bmatrix} \varepsilon^o \\ \kappa \end{bmatrix} \qquad \text{Equation 2-8}$$

where N and M are the resultant forces and moments on a laminate, and ε^0 and κ are the mid-plane strains and curvatures of the laminate, respectively. The A, B and D are the material's extensional, coupling and bending stiffness matrices, respectively. These matrices are calculated using the following relationships (Daniel & Ishai, 2005):

$$\begin{aligned} A_{ij} &= \sum_{k=1}^{n} Q_{ij}^k (z_k - z_{k-1}) \\ B_{ij} &= \frac{1}{2}\sum_{k=1}^{n} Q_{ij}^k (z_k^2 - z_{k-1}^2) \\ D_{ij} &= \frac{1}{3}\sum_{k=1}^{n} Q_{ij}^k (z_k^3 - z_{k-1}^3) \end{aligned} \qquad \text{Equation 2-9}$$

where k is the layer number starting from the bottom of the laminate, as can be seen in Figure 2-2. The Q_{ij}^{k} represents the stiffness components of the k_{th} layer lamina, whose coordinate z_k is measured from the mid-plane of the laminate in the z-direction.

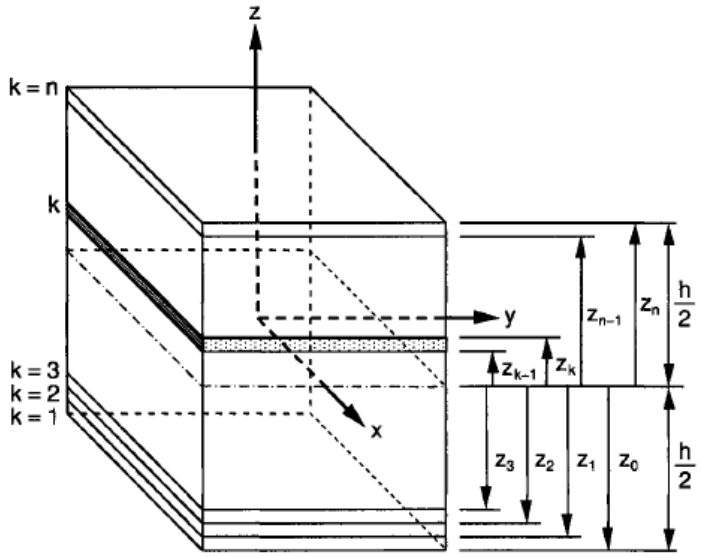

Figure 2-2 Illustration of the coordinate system and notations used in Equation 2-9 (Daniel & Ishai, 2005).

Chapter 3: Evaluation of the Mechanical Properties of the Dowel-reinforced 3D Hybrid Composite Material

In this chapter, the procedures used to evaluate the mechanical properties of the wood dowel-reinforced 3D hybrid composite (hereafter referred to as WC3DFRP) are described. The properties were evaluated using the standard three-point flexural test and compression test. In addition, finite element (FE) models were constructed to simulate the tests and also tune the mechanical properties for use in the FE model of WC3DFRP poles.

3.1. Flexural test

3.1.1. Specimen preparation

The WC3DFRP used in preparing the specimens used in three-point flexural and compressive tests is the same; therefore, only the fabrication of the WC3DFRP specimens used in the flexural test is described in this section.

The 3D glass fabric was cut into 200 x 150 mm (in the weft and warp directions, respectively), for each test category. Each piece of fabric was weighed to calculate the amount of required epoxy (i.e., equal to 1.3 times the weight of the fabric). This amount is adequate for saturating the fabric (without excessive resin that could fill the empty cavities of the 3D fabric), and resin wastage (i.e., resin remaining in the mixing cup and brush).

It is important to note that the dowels used were 3.175 mm in diameter, slightly larger than the width and height of the fabric channels of the untreated fabric. Therefore, the dowels had to be carefully inserted into every other channel along the warp direction.

A 7 mm thick aluminum plate was cleaned with acetone and was covered with a layer of breather cloth followed by a layer of peel ply (with a slightly larger dimension than the breather material). West System 105 room-cured resin and 206 hardener (WEST SYSTEM, 2014) were used to prepare the 3D FRP. The resin and hardener were mixed thoroughly with a ratio of 5:1, and the mixture was then brushed onto the peel ply. The wood core inserted fabric was placed on the peel ply, and resin was applied to its top surface. The

fabric was then carefully flipped, and resin was applied to its dry (top) surface (see Figure 3-1). Another layer of peel ply was placed on top of the resin-saturated fabric. The use of peel plies provides a better surface finish and helps to reduce the void content in the cured composite.

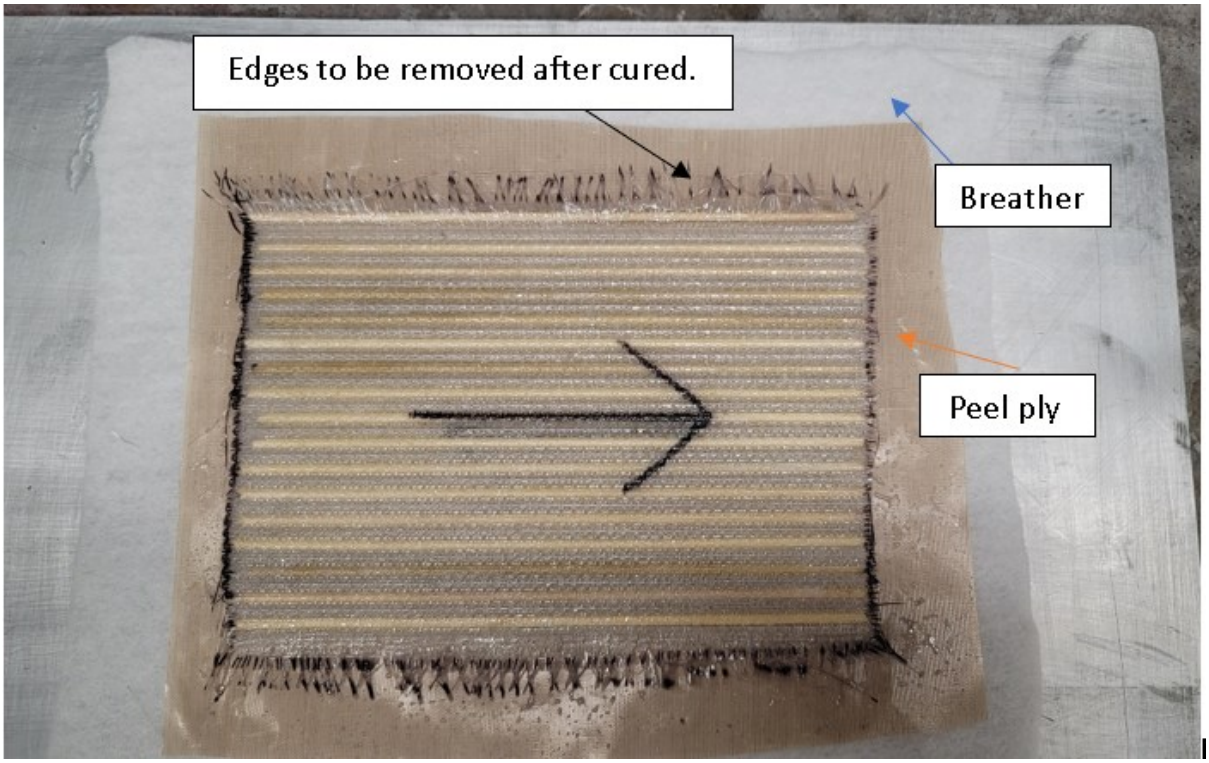

Figure 3-1 WCGFRP being prepared.

A second layer of a breather cloth was placed on the top, followed by the placement of a heavy steel plate on top of the assembly. The breather cloths absorb excess resin; however, since the resin amount was established after a series of trial and error, it was not in an amount to fully adhere the breather cloth to the steel plate and it could be removed fairly easily after the curing period. After waiting 24 hours for the resin to fully cure at room temperature, the peel plies on both sides were peeled off to expose the cured 3DWCFRP panel. The extra edge fibers of the panels were then trimmed using a rotary diamond saw, and the panel was then cut into appropriate size specimens as per ASTM-D7264 (2015) for the bending test, and ASTM-D6641 (2017), for the compressive test. As

can be seen in Figure 3-2, each specimen or coupon included one empty channel at mid-width, neighboured by two dowels-inserted channels and a half-width empty channel on the exterior edges. Five coupons were extracted from the panels for each test category, with 150 mm length for the three-point bending test and 140 mm for the compressive test as per the ASTM standards.

Figure 3-3 shows the coupons ready for the flexural and compressive tests.

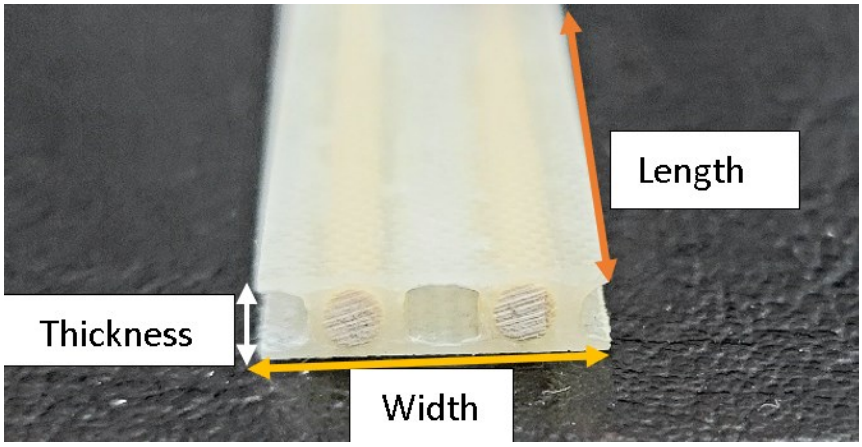

Figure 3-2 Coupon's cross-section.

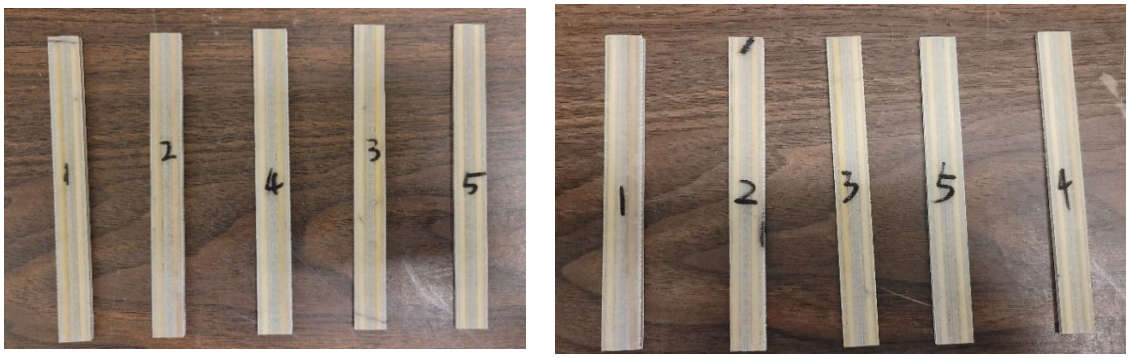

(a) (b)

Figure 3-3 Prepared specimens for (a) flexural test and (b) compressive test.

3.2. Three-Point Flexural Test

3.2.1. Test method

The bending test was carried out following procedure A of ASTM-D7264 (2015). Table 3-1 shows the coupon dimensions. Each value is an average of three readings taken at three different locations on the coupon (at the two ends and the mid-span).

Table 3-1 Flexural test specimen dimensions

Number	Length (mm)	Thickness (mm)	Width (mm)
1	153.2	3.9	14.9
2	153.2	3.9	15.0
3	153.1	4.0	14.9
4	153.4	4.0	16.0
5	153.5	4.0	14.8

The tests were conducted using an MTS servo-hydraulic universal testing machine, using a three-point bending test fixture with a support span of 128 mm in the configuration shown in Figure 3-4. The radius of the load nose and support nose was measured as 7.1 mm and 4.6 mm, respectively. The loading speed was set to 1 mm/min as per the standard. The first test was performed with a maximum allowable actuator displacement set at 10 mm, and the initial failure was observed to occur at 9.2 mm actuator displacement. To capture the full response of the remaining specimens, the maximum actuation displacement was increased to 25 mm.

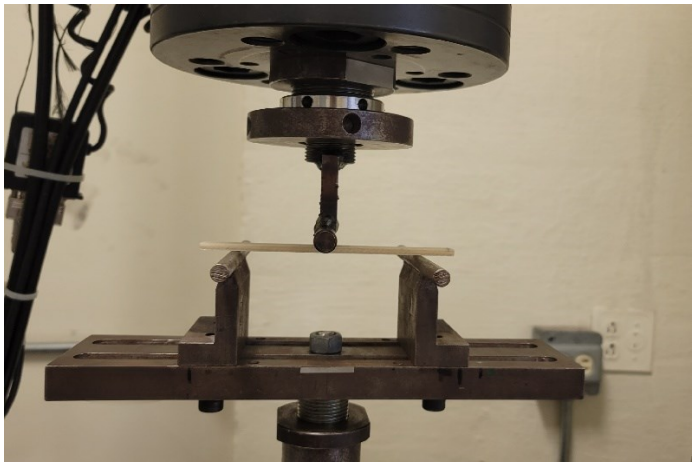

Figure 3-4 Three-point flexural test setup.

3.2.2. Numerical models

It should be noted that the main objective of conducting the flexural and compressive tests was to obtain the basic mechanical properties required for the finite element analysis of the full composite poles fabricated with the 3D dowel-reinforced FRPs. Moreover, the other objective was to evaluate the performance of several composite-related and contact-related algorithms of the FE software using smaller-size models. Therefore, a preliminary finite element model was constructed to mimic the flexural test, by which the required mechanical properties were tuned against the experimental results. Due to the symmetry in geometry and boundary conditions, only a quarter model of the specimen had to be constructed, as illustrated in

Figure 3-5, in which the symmetry boundary conditions are also illustrated.

The model was constructed using LS-DYNA commercial finite element software and was solved explicitly using consistent units of MPa, mm, g, and msec (corresponding to stress, length, mass and time, respectively). The geometric dimensions with the unit in mm of the unit cell of the fabric used to construct the model are illustrated in Figure 3-6.

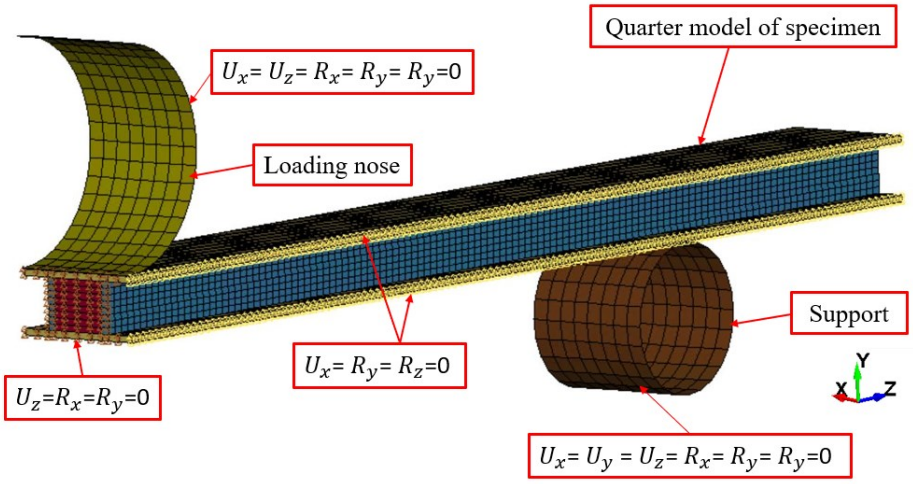

Figure 3-5 The quarter symmetry model of the flexural test specimens and the imposed boundary conditions

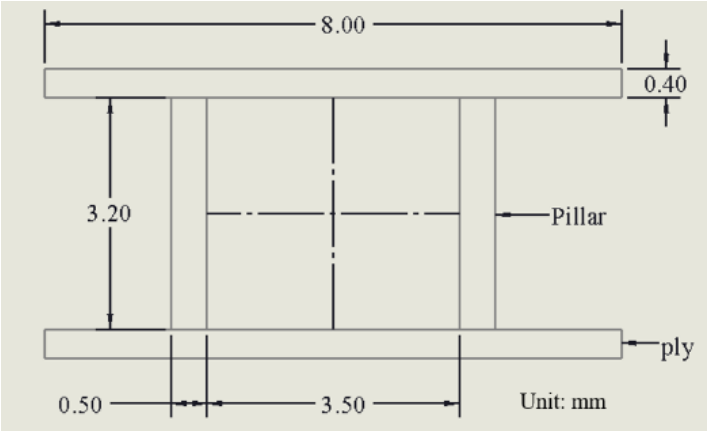

Figure 3-6 The dimensions of the 3D fabric unit cell used in the numerical model.

To prevent the potential shear-locking phenomenon that commonly occurs in fully integrated elements, the selective reduced-integrated (SRI) Tshell element (ELFORM=2) of LS-DYNA was used for modelling the plies and pillars. The benefits of using the SRI formula essentially provide a balance in numerical accuracy and computational efficiency. The dowels were modelled using the solid element with SRI formulation (ELFORM= -2) which also accounts for poor aspect ratio and has a very accurate formulation compared with the other solid elements of the software.

Since the dowels and 3D FRP are bonded together with epoxy resin, hence, the contact interface was modelled using an appropriate contact algorithm. For that, the "CONTACT_AUTOMATIC_SURFACE_TO_SURFACE_CONTACT_TIEBREAK" of LS-

DYNA was incorporated. This algorithm has the option of incorporating the cohesive zone model (CZM) to account for the potential delamination of dowel/pillars and dowel/plies interfaces. The values of the CZM parameters were obtained from (Mohamed & Taheri, 2017), and tabulated in Table 3-2.

The CONTACT_AUTOMATIC_SURFACE_TO_SURFACE algorithm was incorporated to simulate the contact between the loading nose-to-specimen and support nose-to-specimen interfaces. All frictional coefficients of this contact were set to 0.3. It is also crucial to account for the potential contact of the loading nose and the dowel after the top fabric layer is ruptured, which was observed during the tests. Therefore, the "CONTACT_ERODING_SURFACE_ TO_SURFACE" was incorporated to preserve the contact between the dowel and plies if elements representing the plies are eroded (or deleted).

Table 3-2 Summary of the epoxy-related parameters required by the CZM contact algorithm.

Normal failure stress (MPa)	Shear failure stress (MPa)	Mode I energy release rate (KJ/m^2)	Mode II energy release rate (KJ/m^2)	Penalty stiffness (N/mm^3)
59	23	1	1.5	3500

The 3D fabric and pillar materials were modelled using MAT_054_ENHANCED _COMPOSITE_DAMAGE material model of LS-DYNA, which is capable of assessing the damage evolution using the ultimate strain values. The mechanical properties used in this model are shown in Table 3-3.

The mechanical properties of the dowel were estimated based on the published results and were also tuned using the experimental results. The dowel wood was modelled using one of LS-DYNA's orthotropic materials, namely MAT_143_WOOD. Initially, the mechanical properties of American ash (Forest Service & Products Laboratory, 2010) were used for the dowels; the properties were then calibrated by comparing the numerical results against the experimental results. It should be noted that this material model requires mechanical properties along the grain, in tangential, and radial directions. However, visual inspection makes it nearly impossible to distinguish the tangential and radial directions in

a given dowel because dowels have round cross-sections, and the directions are not discernable. Therefore, the tangential and radial directions were assumed in the directions facing the pillars and plies, respectively.

Table 3-3 Refined material properties used in flexural and compressive models.

	$\boldsymbol{\rho}$ ($\boldsymbol{g/mm^3}$)	$\boldsymbol{E_{11}}$ (M$\boldsymbol{Pa}$)	$\boldsymbol{E_{22}}$ (M$\boldsymbol{Pa}$)	$\boldsymbol{\upsilon_{21}}$	$\boldsymbol{G_{12}}$ (M$\boldsymbol{Pa}$)	$\boldsymbol{G_{23}}$ (M$\boldsymbol{Pa}$)	$\boldsymbol{G_{31}}$ (M$\boldsymbol{Pa}$)
Ply	0.00175	9000	9000	0.05	1000	1000	1000
	$\boldsymbol{X_C}$ (M$\boldsymbol{Pa}$)	$\boldsymbol{X_T}$ (M$\boldsymbol{Pa}$)	$\boldsymbol{Y_C}$ (M$\boldsymbol{Pa}$)	$\boldsymbol{Y_T}$ (M$\boldsymbol{Pa}$)	$\boldsymbol{S_{12}}$ (M$\boldsymbol{Pa}$)	ε_{T1}	ε_{C1}
	153	179	153	179	30	0.08	-0.04
	$\boldsymbol{\rho}$ ($\boldsymbol{g/mm^3}$)	$\boldsymbol{E_{11}}$ (M$\boldsymbol{Pa}$)	$\boldsymbol{E_{22}}$ (M$\boldsymbol{Pa}$)	$\boldsymbol{\upsilon_{21}}$	$\boldsymbol{G_{12}}$ (M$\boldsymbol{Pa}$)	$\boldsymbol{G_{23}}$ (M$\boldsymbol{Pa}$)	$\boldsymbol{G_{31}}$ (M$\boldsymbol{Pa}$)
Pillar	0.00175	3000	1000	0.05	1000	1000	1000
	$\boldsymbol{X_C}$ (M$\boldsymbol{Pa}$)	$\boldsymbol{X_T}$ (M$\boldsymbol{Pa}$)	$\boldsymbol{Y_C}$ (M$\boldsymbol{Pa}$)	$\boldsymbol{Y_T}$ (M$\boldsymbol{Pa}$)	$\boldsymbol{S_{12}}$ (M$\boldsymbol{Pa}$)	ε_{T1}	ε_{C1}
	80	80	80	80	30	0.054	-0.054
	$\boldsymbol{\rho}$ ($\boldsymbol{g/mm^3}$)	$\boldsymbol{E_L}$ (M$\boldsymbol{Pa}$)	$\boldsymbol{E_T}$ (M$\boldsymbol{Pa}$)	$\boldsymbol{G_{LT}}$ (M$\boldsymbol{Pa}$)	$\boldsymbol{G_{LR}}$ (M$\boldsymbol{Pa}$)	$\boldsymbol{\upsilon_{12}}$	$\boldsymbol{X_C}$ (M$\boldsymbol{Pa}$)
Dowel	0.0006	11330	974.38	1099.01	1665.51	23671	51.1
	$\boldsymbol{X_T}$ (M$\boldsymbol{Pa}$)	$\boldsymbol{Y_C}$ (M$\boldsymbol{Pa}$)	$\boldsymbol{Y_C}$ (M$\boldsymbol{Pa}$)	$\boldsymbol{S_{12}}$ (M$\boldsymbol{Pa}$)			
	51.1	6.5	8	13.2			

Figure 3-7 shows the principal directions of the FE model's constituents corresponding to the principal material direction of the 3D fabric and dowels material properties reported in Table 3-3. In other words, the A, B, and C seen in the figure correspond to the orthogonal principal material directions 1, 2 and 3, respectively. As stated in the previous section, the

pillar fibers are oriented at 30° with respect to the through-thickness axis of the fabric. This orientation is accommodated by specifying the angle as one of the input parameters to the material model. The footnotes L, T and R shown in the elastic modulus of the dowel represent the wood's longitudinal, tangential, and radial directions corresponding to A, B and C in Figure 3-7.

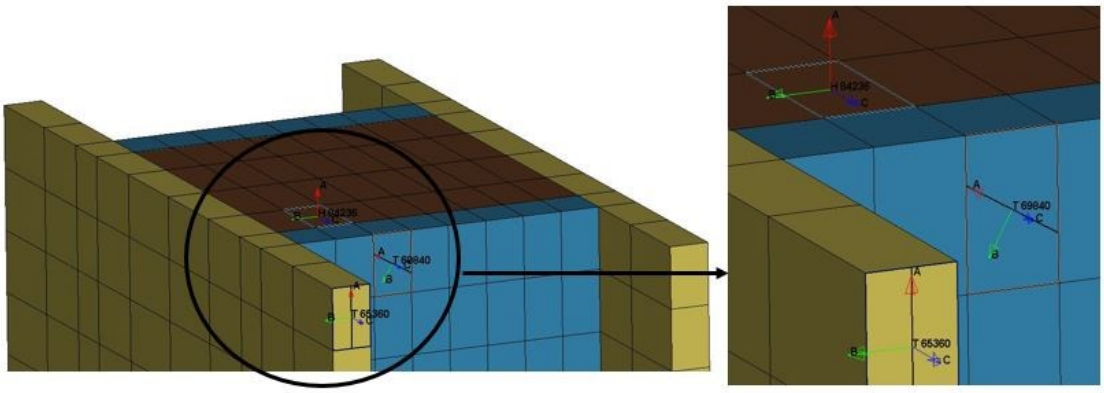

Figure 3-7 Material directions identified by the arrows in LS-DYNA preprocessor.

3.2.1. Results and discussions

Figure 3-8 shows the experimental results for the five specimens tested in a three-point bending configuration and also the FE model's predictions. As can be seen, the results are quite close. The test results, including the calculated properties using the results, are summarized in Table 3-4. As can be seen, specimen 2 failed at the lowest ultimate load and deflection, whereas specimen 4 exhibited the highest ultimate load (137 N). Even though specimen 4 had a higher capacity than specimen 2, it had the lowest flexural modulus, E_f. The flexural rigidity, $E_f I$, is the parameter used in the design and analysis of components subjected to bending. For the given configuration, it can be calculated using Equation 3-1:

$$E_f I = \frac{FL^3}{48\delta} \qquad \text{Equation 3-1}$$

where F is the load, L is the support span, I is the area moment of inertia and δ is the deflection corresponding to load F (taken at the linear portion of the load vs. deflection curve). The differences in load-deflection curves are attributed to potential fabrication-

related anomalies such as non-uniform void and resin distribution that are invariably developed in any hand layup process.

The comparison of the average experimental results and those produced by the numerical simulation is reported in Table 3-5 with a maximum error of 10.5% in the predicted modulus of rigidity, thus, confirming the integrity of the developed FE model. However, the numerically predicted flexural stiffness is slightly lower than the average stiffness of the actual material.

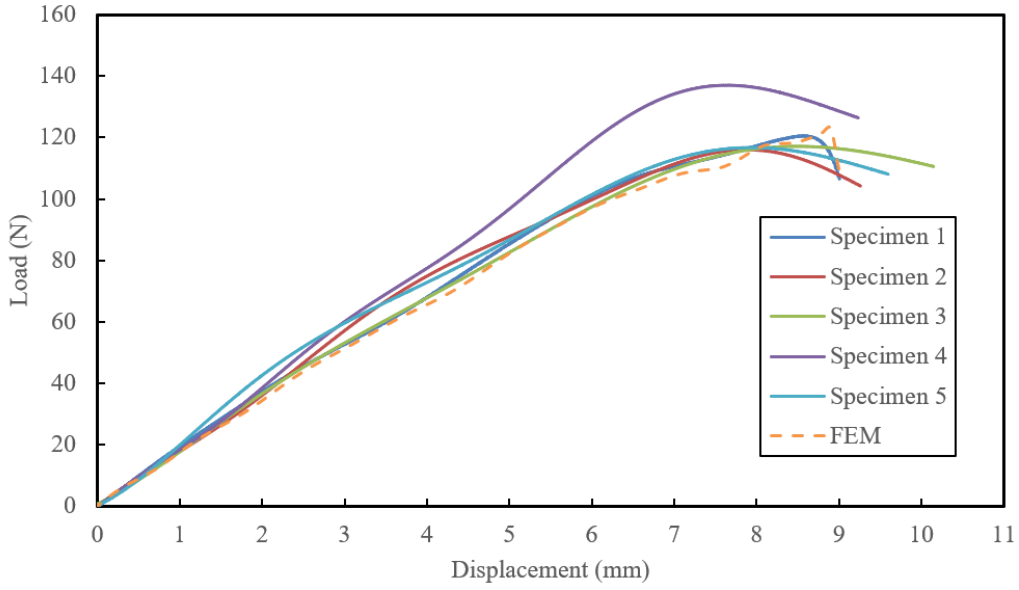

Figure 3-8 Comparison of the experimental and numerical load-displacement curves.

Table 3-4 Summary of three-point flexural results.

Specimens ID	Ultimate. Load (N)	Ultimate. Displacement (mm)	E_f (MPa)	Moment of inertia, I (mm4)	Rigidities (N·mm^2)
1	120.5	8.6	10,009.1		662,605.6
2	116.0	7.3	10,316.8		682,974.0
3	117.1	8.5	10,230.0	66.2	677,226.3
4	137.0	7.6	9,853.5		652,304.1
5	116.7	7.5	10,926.1		723,306.6

Table 3-5 Comparison of the average experimental values again the numerically predicted

	Max Load (N)	Max. Disp. (mm)	E_f (MPa)	Flexural Rigidity (N·mm^2)	% Error
Exp	134.0	8.6	10,267.1	679,683.3	10.5
FEM	128.0	8.9	9188.42	608,273.1	

Figure 3-9 illustrates the damage developed in the actual specimen and the predicted damage by the numerical model. In Figure 3-9(c) and (d), the elements that are in red, blue and brown represent the plies, pillars and dowel, respectively. As seen, the FE model could successfully simulate the ply and pillar failures by deleting some of the highly stressed elements in the damaged region. As can be seen in Figure 3-9(a), the ply region on top of the empty channel, located at the mid-span and mid-width, is the most vulnerable region. A good agreement is seen between the actual and FE model's prediction. The micro failure located on the tension side of the pillar was also captured by the model, as seen in Figure 3-9(c) and Figure 3-9(d).

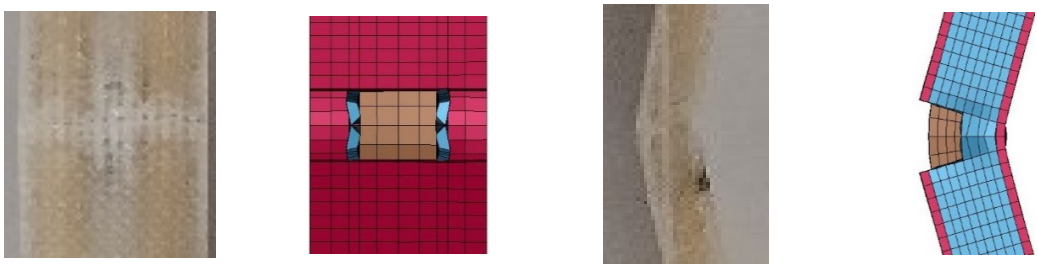

(a) (b) (c) (d)

Figure 3-9 Comparison of the post-failure damage on the actual specimen and the numerically predicted – top views (a) Actual (b) numerical; side view (c) actual (d) numerical.

3.3. Compression test

3.3.1. Test method

As briefly stated, the compression test was conducted in accordance with the ASTM D6641(2017), using the Combined Loading Compression (CLC) fixture (see Figure 3-10). Five coupons were tested. The dimensions of the coupons are listed in Table 3-6. As in the

bending test, all measurements were taken at their locations, and the average values were reported.

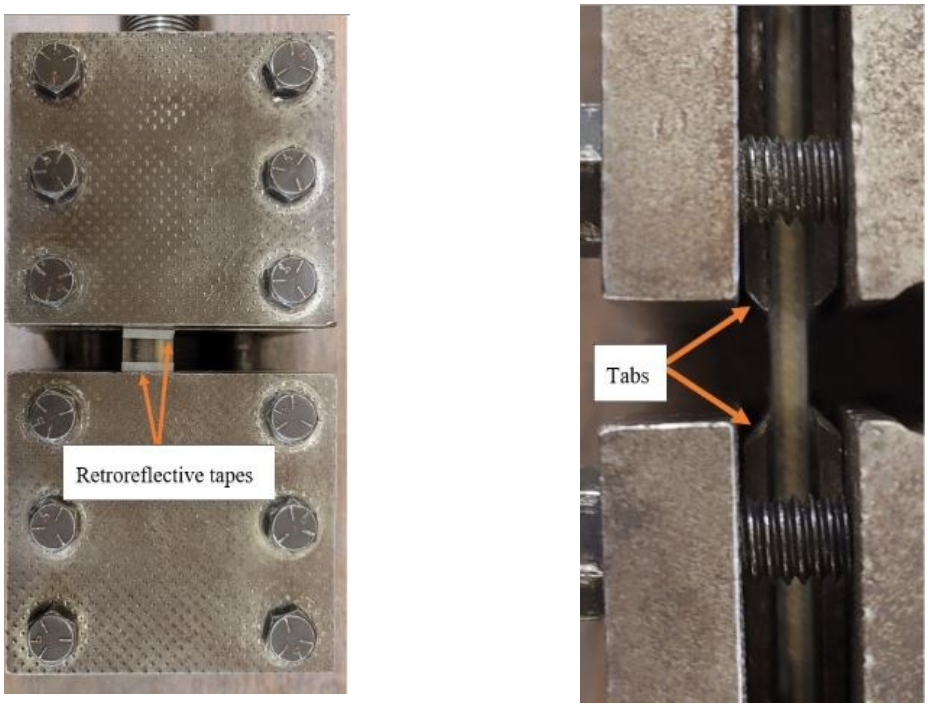

(a) (b)

Figure 3-10 Front (s) and side (b) views of compression test coupon secured by the CLC fixture

Table 3-6 Dimensions of the compressive test coupons.

Specimen ID	Length (mm)	Width (mm)	Thickness (mm)
1	140.2	15.2	3.9
2	140.3	14.6	4.0
3	140.1	15.0	4.1
4	140.3	14.7	4.1
5	140.3	16.0	4.0

A laser extensometer, shown in Figure 3-11, was used to record the material's deformation within the gauge length between the two 3 mm wide reflective tapes mounted

in parallel, as shown in Figure 3-10. The gauge length was set at 13 mm as per the below equation given in the standard.

$$h \geq \frac{l_g}{0.9069\sqrt{(1-\frac{1.2F^{cu}}{G_{xz}})(\frac{E^f}{F^{cu}})}} \qquad \text{Equation 3-2}$$

where l_g is the gauge length, F^{cu} is the estimated ultimate compressive strength, G_{xz} is the estimated interlaminar shear modulus and E^f is the estimated flexural modulus. Rough estimates were established for $F^{cu} = 50$ MPa and $G_{xz} = 1000\,MPa$. Then, by inputting $E^f = 6{,}199.9$ MPa as stated in Equation 3-2 and $l_g = 13\,mm$ to the rest of the unknowns in Equation 3-2, the estimated h has to be at least equal to or greater than 1.2 mm. Therefore, the 4 mm-thickness coupons satisfy the requirement. Each coupon was carefully placed in the fixture, and the longitudinal edges of the specimen were ensured to be parallel to the longitudinal edges of each half of the fixture. Both the coupon and fixture were carefully adjusted to make sure the tapes appeared within the gauge area. Each tab's position was also adjusted to align them to the outer bounds of the tapes, as shown in Figure 3-10. All the bolts were then evenly tightened in a cross pattern to secure the coupon and fixture's position. Finally, the fixture was mounted on the machine's support plate, as shown in Figure 3-11. The test was performed at a rate of 1.3 mm/min until failure was observed.

The same Tshell and solid elements used in the flexural model were used to construct the compression specimen model. In this model, the contacts between the dowel and plies, dowel and pillars interfaces were modelled using the "CONTACT_ERODING_SURFACE_TO_SURFACE" algorithm, which differed from the flexural model. The rest of the contact settings and material parameters remained unchanged.

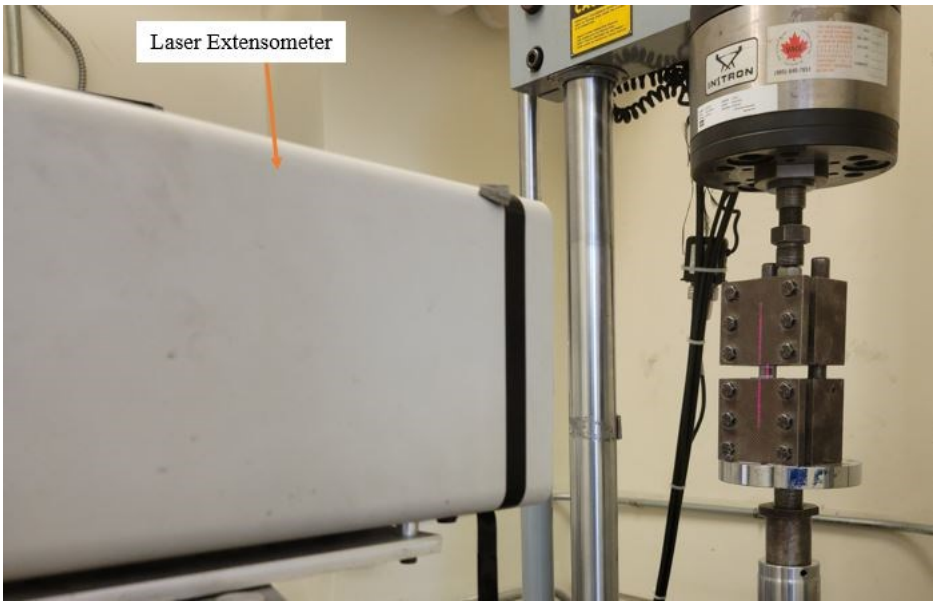

Figure 3-11 Compression test set up.

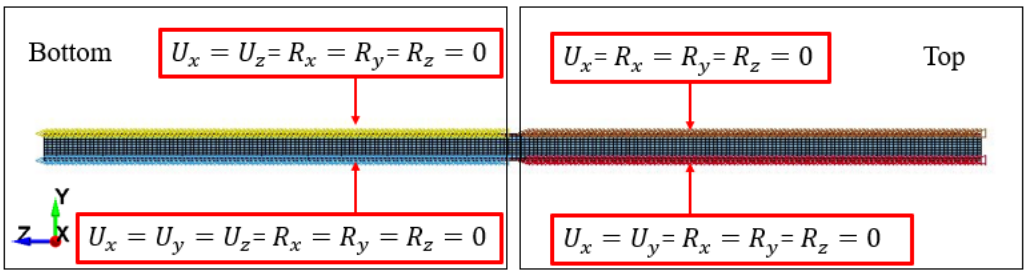

Figure 3-12 Boundary conditions of the FE model depicting the compression coupon.

3.3.2. Results and discussions

The compression model was analyzed using the same tuned mechanical properties established in the previous section. The numerical results are compared against the experimental results in Figure 3-13.

As can be seen, the numerical predictions follow the trend in the load-displacement curve observed experimentally very closely. Specimen 4 exhibited the highest ultimate load, while specimen 2 showed the lowest. Specimen 1 underwent the largest displacement and could maintain the load after attaining its ultimate strength by deforming

approximately 0.03 mm before it failed, while specimen 2 failed the earliest. The discrepancies in the experimental results are attributed to the presence of nonuniformly distributed void content invariably developed when composites are not subjected to vacuum during their curing stage. The numerical model showed an elastic response up to a displacement of 0.1 mm, after which it deformed nonlinearly as the dowels failed.

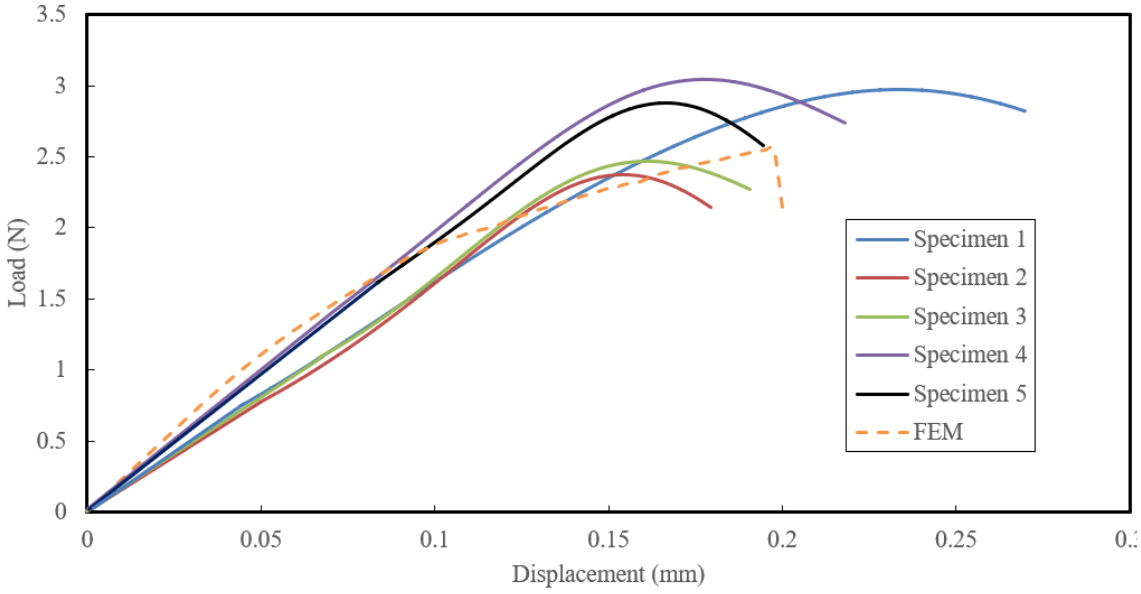

Figure 3-13 Comparison of the experimental and numerical load-displacement curves

Table 3-7 Summary of significant results in the compression test. summarizes the experimental results as well as the numerically predicted values. The ultimate compressive strength and elastic modulus are calculated using the basic mechanics of materials equations:

$$\sigma_{ult} = \frac{P_{ult}}{wt} \quad \text{and} \quad E_c = \frac{\sigma}{\varepsilon} \qquad \text{Equation 3-3}$$

where σ and ε are the strength and strain values on the elastic region of the curve, respectively, P_{ult} is the ultimate load, and w and t are the width and thickness of the specimen's cross-section, respectively.

Interestingly, specimen 1 had the second-lowest elastic moduli, while it exhibited the most ductile response. The standard deviation of the maximum strength is 7.7 MPa, which

is believed to be reasonable considering the complexity of the material configuration and experiment.

Table 3-7 Summary of significant results in the compression test.

Specimen IDs	Elastic modulus, E_c (MPa)	Ultimate Load (N)	Failure strength (MPa)	Ultimate strain (mm/mm)	Ultimate Strength Std Dev
1	8,427.6	2,977.3	74.1	0.017	
2	8,445.3	2,370,0	59.7	0.012	
3	8,466.5	2,467.4	63.5	0.013	7.7
4	9,792.1	3,041.6	78.3	0.016	
5	9,686.1	2,878.7	72.3	0.014	

The average values of the experimental and numerical results are also compared and reported in Table 3-8 Comparison of the average experimental values and the numerically predicted values.

Table 3-8 Comparison of the average experimental values and the numerically predicted values

	Elastic modulus, E_c (MPa)	Ultimate Load (N)	Ultimate Strength (MPa)	Ultimate Strain (mm/mm)	% Error in Elastic modulus
Exp	8,963.5	2,747.0	69.5	0.015	9.9%
FEM	8080.0	2,556.0	61.4	0.017	

The comparison of the the elstic modulus obtained from the experimental results and that from the numerical results shows a difference of 9.9%. The experimental strain values were calculated using the gauge-length displacement values recorded by the extensometer. The numerically calculated ultimate strains were obtained based on the displacements of

the nodes corresponding to the positions of the reflective tapes, sampled at one timestep before the specimen's failure.

Figure 3-14 compares the experimentally observed numerically predicted failure modes. The FE model's colour scheme is the same as that described for the three-point bending model. As seen in Figure 3-14(b), the numerical model could predict the ply failure fairly accurately. The numerical model could also capture the shear crimping that occurred in the dowel (see Figure 3-14(c) and Figure 3-14(d)). As seen in Figure 3-14(d), the elements corresponding to the plies and pillars are deleted around the kink region in the dowel, which resembles quite closely to the experimental observation.

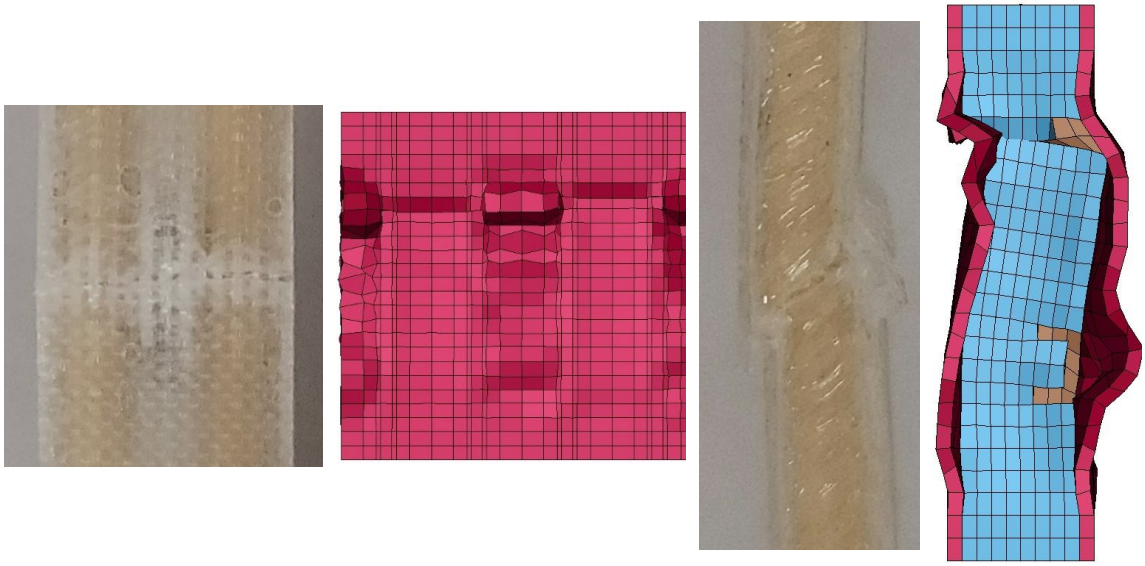

(a) (b) (c) (d)

Figure 3-14 Compression of the experimental and numerically predicted compressive failure of a WCGFRP coupon (a) Experimental front view (b) numerical front view (c) Experimental side view. (d) numerical side view

Chapter 4: Design of Scaled Poles

This chapter discusses the development of two types of scaled-down composite poles that are made of conventional 2D FRP (i.e., glass-epoxy) and the introduced WC3DFRP material. In addition, the test setup data, including fixture design and loading scheme and data acquisition, are also discussed. The fabricated FRP and WC3DFRP scaled-down poles are referred to as 2D and 3D poles, hereafter in this chapter.

The 2D poles have a modular design. In brief, the advantages of modular poles over conventional prismatic poles include easier transportation, less maintenance cost when replacing the modules and improved versatility in assembling the modules to meet different in-service conditions. The 3D poles would have to be prismatic due to the inherent and complex configuration of the 3D fabric.

4.1. 2D Scaled pole design

Development of an FRP pole requires a comprehensive consideration of experimental resources, classic lamination theory and design limitations. The final geometry of a pole results from a compromise between the theoretical design and the experimental response assessment, which would invariably include human errors taking place during the testing of the pole in a laboratory environment.

4.1.1. Preliminary Laminate design and optimization

In contrast to geometrical optimization, orthotropic materials optimization remains a challenging task for finite element (FE) software. However, NISA Suite 2019 provides a structural optimization module (the OPT module), applicable to laminated composite materials. Unlike the conventional geometrical optimization often used in relation to isotropic materials, OPT is capable of optimizing both the thickness and fiber angle of each lamina of a given laminate.

It should be noted that, at the time of this optimization, the geometrical design of the 2D pole was still in the early stages, and therefore, the pole geometry used in this

optimization does not reflect the actual pole design constructed and tested in the lab. Nevertheless, the optimized results were utilized to guide the final laminate design.

The optimization analysis in NISA is based on a working model, and OPT only supports the use of 2D composite shell elements (NKTP=32) instead of the preferred 3D layered solid composite element (NKTP=7), which is not supported by OPT. Consequently, a prismatic fiber-reinforced polymer (FRP) pole was considered using the shell element, with a physical diameter of 44 mm and a height of 600 mm. The unidirectional E-glass/Epoxy was employed with the estimated mechanical properties, as shown in Table 4-1. As customarily assumed when designing poles, 10% of the total pole length was assumed to be embedded in the ground; therefore, all nodes within that portion of the length were fully constrained. The pole was subjected to a lateral load of 10,366 N applied at 30 mm below the tip. This load was selected based on the theoretical assessment using the Tsai-Hill failure criterion, as the load that would initiate the failure of the pole.

Table 4-1 Estimated mechanical properties of the unidirectional composite used in NISA OPT.

E_{11} (MPa)	E_{22} (MPa)	E_{33} (MPa)	G_{12} (MPa)	G_{23} (MPa)	G_{31} (MPa)
39,700	8,500	8,500	4,200	4,200	8,400
X_C (MPa)	X_T (MPa)	Y_C (MPa)	Y_T (MPa)	Z_C (MPa)	Z_T (MPa)
686	990	155	58	283	58
S_{21} (MPa)	S_{31} (MPa)	S_{32} (MPa)	υ_{12}	ρ ($\frac{g}{mm^3}$)	
27	27	27	0.3	0.001746	

Table 4-2 presents the preliminary laminated layup sequence, with the material angle measured with respect to the pole's axial direction; the axial direction also serves as the material principle (along the x-axis) in this model, as seen in

Figure 4-1. The layer number starts from inside to outside of the pole.

Table 4-2 Summary of the layup sequence and thicknesses of the laminate before optimization.

Layer number	1	2	3	4	5	6
Thickness (mm)	1	1	1	0.4	1	0.8
Fiber angle (°)	0	0	0	45	0	90
Layer number	7	8	9	10	11	12
Thickness (mm)	1.2	0.4	1.2	0.4	1.2	0.6
Material angle (°)	0	-45	0	45	0	0

After the model was fully constructed (including the boundary conditions) in the Display IV environment (i.e., the preprocessor), the model was then imported to OPT to utilize the optimization code. The Generalized Reduced Gradient (GRG) optimization algorithm was used in cooperation with the volume cost function for the minimization. The stress constraint was set to the Tasi-Hill failure criterion, which limits failure-causing stresses occurring at the Gauss integration points of each element. The algorithm could adjust both the ply thickness and material angle to test the performance of the OPT algorithms. To help the convergency of the optimization function, the adjustable bound was set to ±0.6 mm for the thickness and 360° for the angle. The optimized stacking sequence of the laminate is reported in Table 4-3. All the layers' angles were optimized close to the nearest practical degree (practical in terms of fabrication practicality and minimization of material wastage). Although the total thickness was increased by 0.4 mm after the optimization, the maximum pole tip deflection was greatly reduced (by about 30%, from 53 mm to 37 mm), as seen in Table 4-4. This improvement is attained by increasing the pole's extensional stiffness, which was optimized by aligning the fibres mainly along the axial direction of the pole and through the thickness. The analytical procedure for establishing the extensional stiffness is documented in Chapter 2.

Figure 4-1 shows the pole's stress contours in the principal direction of the material on the outer layer of the pole after the optimization, in which the maximum compressive

(negative) stress is identified by the dark-blue contour, and the maximum tensile stress is in red. The actual deflection was scaled up threefold for better visualization.

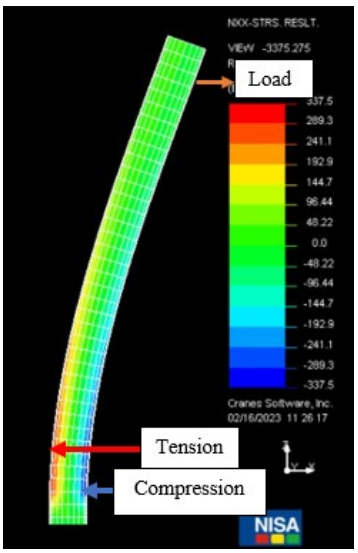

Figure 4-1 Post-optimization stress contours in the principal material direction on the outer lamina of the pole.

Table 4-3 Summary of the layup sequence and thicknesses of the laminate after optimization.

Layer number	1	2	3	4	5	6
Thickness (mm)	0.6	1.2	0.4	1.2	0.4	1.2
Material angle (°)	0	0	349	0	360	360
Layer number	7	8	9	10	11	12
Thickness (mm)	1.2	1	0.4	1	1	1
Material angle (°)	0	0	0	349	0	0

Table 4-4 Performance comparison of before and after the optimization.

	Total thickness (mm)	Maximum deflection at tip (mm)	Deflection reduced (%)
Before optimization	10.2	52.8	30
After optimization	10.6	37.0	

4.1.2. Further numerical analysis using LS-DYNA FE software

As discussed in the previous section, NISA OPT employed a mathematical method to determine the optimal solution for the given problem. However, in the context of laminated composite materials, it is important to also consider the pole's strength in the hoop direction, which helps prevent local buckling failure resulting from ovalization, especially at the ground line boundary. Additionally, it is essential to investigate the interlaminar failures because laminated materials' weakest link is their interlaminar strength; this requires the use of the layered 3D element. From a material modelling perspective, in comparison to NISA, LS-DYNA offers a more sophisticated material model for modelling composites. Not only does the material model incorporate more sophisticated failure criteria, but it also has the capability of degrading and eroding (deleting) the critically stressed elements.

Nevertheless, despite the sophisticated failure criteria for in-plane failure assessment, if one wants to assess the interlaminar failure, as briefly mentioned earlier, one would have to use the 3D solid layered element, which only allows examination of material failures using the Maximum Stress Failure criterion. Therefore, to investigate the optimal stacking sequence for a laminate with a constant thickness, a model was constructed in LS-DYNA, using its 3D solid elements. The layup consisted of unidirectional (UD) E-glass fibers and biaxial [0/90] glass fabrics to examine the potential for interlaminar failure. The model considered a prismatic pole with the dimensions and boundary conditions presented in Table 4-5. The material properties of the UD and biaxial fabrics were selected based on the reported material properties by Chen et al. (2022) and those in ALT Composite Pty Ltd (n.d), respectively, as outlined in Table 4-6. To enable through-thickness stresses, the MAT_059_SOLID_COMP-OSITE_FAILURE_SOLID_MODEL of LS-DYNA was uti-lized. This material model includes eight failure modes: normal tension and compression failures in the orthogonal directions, and in-plane and out-of-plane shears. The corresponding stresses can be obtained as additional history variables in each element and are only saved upon request. To save these variables, the DATABASE_EXTENT_BINARY was invoked, with the NEIPH parameter set to 18. NEIPH controls the number of history variables to be saved for post-processing.

Table 4-5 Geometries and test setups used in LS-DYNA.

Geometry	Length (mm)	Inner diameter (mm)	Thickness (mm)
	2000	48	2.6
Boundary conditions	Pole embedment height (mm)	Distance of load from the tip (mm)	Load magnitude (N)
	200	100	793

Table 4-6 Mechanical properties of the materials used in LS-DYNA models.

UD	E_{11} (MPa)	E_{22} (MPa)	E_{33} (MPa)	G_{12} (MPa)	G_{23} (MPa)	G_{31} (MPa)
	37,650	9,233	9,233	3,228	3,131	3,228
	X_C (MPa)	X_T (MPa)	Y_C (MPa)	Y_T (MPa)	Z_C (MPa)	Z_T (MPa)
	725	1,075	283	58	283	58
	S_{21} (MPa)	S_{31} (MPa)	S_{32} (MPa)	$\nu 21$	ρ ($\frac{g}{mm^3}$)	
	118	118	94	0.069	0.001746	
Biaxial [0/90]	E_{11} (MPa)	E_{22} (MPa)	E_{33} (MPa)	G_{12} (MPa)	G_{23} (MPa)	G_{31} (MPa)
	14,200	14,200	14,200	2,770	5,550	2,770
	X_C (MPa)	X_T (MPa)	Y_C (MPa)	Y_T (MPa)	Z_C (MPa)	Z_T (MPa)
	216	243	216	243	216	243
	S_{21} (MPa)	S_{31} (MPa)	S_{32} (MPa)	$\nu 21$	ρ ($\frac{g}{mm^3}$)	
	42	42	34	0.28	0.001746	

Seven laminated configurations were modelled and compared by examining the failure modes in each layer. The configurations included [$+_2/0_5/+_2$], [$+_4/0_5$], [$90/0_{11}/90$], [$+_7$], [0_{13}],

[+/0_9/+] and [+/90/0_7/90/+], where [+] represents a biaxial [0/90] fabric, and 0° is aligned with the pole axial direction. Table 4-7 summarizes the results of the analyses for the seven designs. In this table, "P" denotes that all layers of the laminate pass the imposed stresses, while "FL" indicates that the laminate is deemed failed due to the failure of one or more of its laminae. As seen, both the [0_{13}](with $[A_{11}] = 99\ kN/mm$) and [+/0_9/+](with $[A_{11}] = 81\ kN/mm$) designs passed the test, indicating that, the extensional stiffness dominates the pole's deflection performance in the cantilever pole test.

Furthermore, these analyses highlight the risk of interlaminar failures when stacking two plies with dissimilar angles, as observed by comparing the [+/0_9/+] and [90/0_{11}/90] designs.

Figure 4-2 shows the onset of delamination failure in the [+7] design. In this plot, "1" indicates the element is intact, while "0" signifies the interlaminar failure of the element. Element 44039 failed due to delamination failure during the last time step of the analysis.

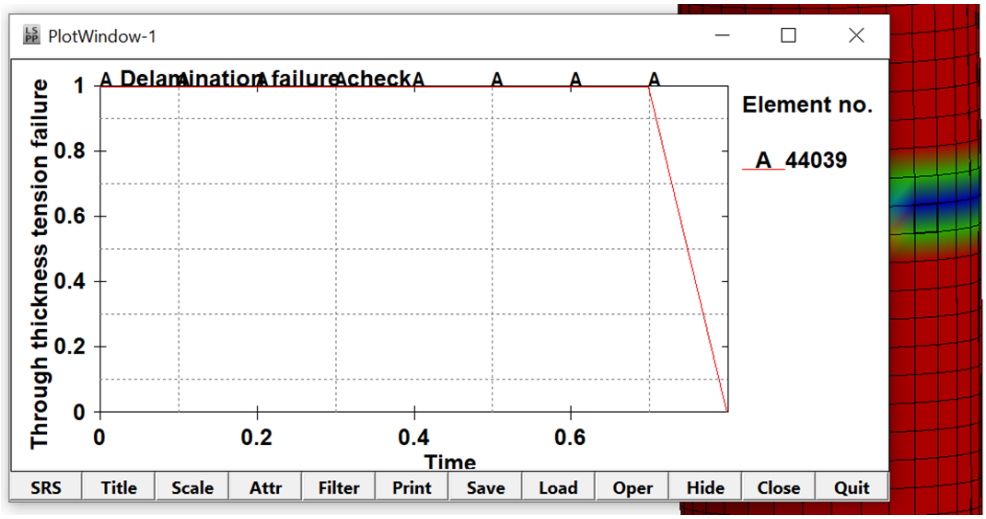

Figure 4-2 Variation in the interlaminar failure index on one of the models' element (1 = intact; 0 = failure).

Table 4-7 Numerical failure indices for various laminated designs.

	$[+_2/0_5/+_2]$	$[+_4/0_5]$	$[90/0_{11}/90]$	$[+_7]$	$[0_{13}]$	$[+/0_9/+]$	$[+/90/0_7/90/+]$
Longitudinal tension failure	FL	FL	P	FL	P	P	FL
Transverse tension failure	P	P	FL	P	P	P	FL
In-plane shear failure	FL	FL	P	FL	P	P	FL
Through-thickness tension failure	FL	FL	FL	FL	P	P	FL
Through-thickness shear failure	P	P	P	P	P	P	FL
Longitudinal compression failure	FL	FL	P	FL	P	P	FL
Transverse compression failure	P	P	P	P	P	P	P
Through-thickness compression failure	FL	P	FL	P	P	P	FL

4.1.3. Influence of element formulation

The last section of this chapter compares the predictions of models using 3D (solid) and 2D (shell) element formulations. This is done to assess the computation efficiency of the elements, which would be important in future analyses when combined nonlinear and environmental loadings will be considered. As discussed previously, both NISA and LS-DYNA software confirmed that laying all the fibers along the axial direction of the pole is the optimal design choice. However, to prevent local buckling around the base of the pole, strengthening the laminate in the hoop direction would be necessary. Among the evaluated laminated designs, $[+/0_9/+]$ was selected as the optimal design; this laminate was considered for further assessing the accuracy of the numerical results and the modelling approach. Therefore, the performance of the selected design was examined using the solid and Tshell elements of LS-DYNA. Note that LS-DYNA offers over 45 shell formulations, one of which is the Tshell (or thick-shell), which is an 8-node shell element with 2D stress state like a shell. The thickness of the element is constrained by a penalty function between the top and bottom nodes; thus, the thickness can only be affected by membrane strain (like a thin shell).

The comparison was initiated by comparing the maximum tip deflection and maximum compressive stress of the selected pole design evaluated by the two elements' formulations against the analytically established values based on the Euler-Bernoulli beam theory. Specifically, the maximum deflection was calculated using the formula for determining the deflection of a cantilever beam using the following equation (Hibbeler, 2016):

$$\delta_{max} = \frac{Fa^2}{6EI}(3L - a) \qquad \text{Equation 4-1}$$

where δ_{max} is the maximum deflection, F is the applied lateral load, and E is the elastic modulus of the pole, and the other parameters are shown in

Figure 4-3.

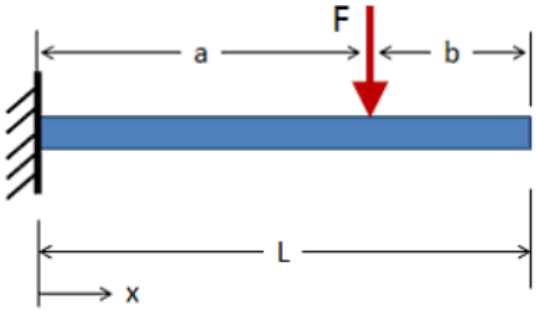

Figure 4-3 Schematic diagram of a cantilevered pole, laterally loaded with a compressive force.

Since the designed FRP pole is a thin-wall structure, the value of elastic modulus, E, was estimated using the following equation (Daniel & Ishai, 2005):

$$E \approx E_x = \frac{1}{[A_{11}]^{-1}T} \qquad \text{Equation 4-2}$$

where E_x is the effective elastic modulus of the laminate in the principal direction of the material, T is the total thickness of the laminate, and $[A_{11}]^{-1}$ is the extensional laminate compliance matrix entry at $i = 1\ and\ j = 1$ (as described in Chapter 2).

The area moment of inertia, I, of the pole was calculated by the following equation (Hibbeler, 2016):

$$I = \frac{\pi}{64}(D_o^4 - D_i^4) \qquad \text{Equation 4-3}$$

where D_i and D_o are the inside and outside diameters of the cross-section.

The same model with [+/0$_9$/+] layup used in the last section was used for additional analysis in this section. The comparison of the numerically evaluated maximum deflection using the solid and Tshell elements of LS-DYNA and the analytical solution is shown in Table 4-8.

As can be seen, both the solid and Tshell elements provide sufficiently accurate results with 0.7% and 2.8% margins of errors, respectively, compared with the analytical solution.

Table 4-8 Comparison of the numerically predicted and analytical maximum tip deflection and bending moment of the pole.

	Solid elements	Tshell elements	Analytical	Solid elements % error	Tshell elements % error
Maximum deflection (mm)	349.3	361.8	352	0.7%	2.8%
Maximum bending stress (MPa)	133	116	137.3	3.2%	15.5%

The value of the maximum compressive bending stress developed in the pole was subsequently calculated analytically based on Equation 4-4 and compared against the numerically predicted values in Table 4-8 Comparison of the numerically predicted and analytical maximum tip deflection and bending moment of the pole..

$$\sigma_{max} = \frac{M_{max}\left(\frac{D_o}{2}\right)}{I} \qquad \text{Equation 4-4}$$

In the above equation, D_o is the outside diameter of the pole, and M_{max} is the maximum bending moment.

The maximum numerically predicted compressive stress is developed immediately above the base region boundary of the FE model. The results reported in Table 4-8 reveal that the model constructed with the solid element maintained its accuracy compared to the analytical models, with only a 3.2% error margin, while the model using the shell element produced a larger error margin (15.5%).

Since the analytical calculations are only based on the pole's extensional elastic modulus, the actual performance of these two types of elements in the modelling of the FRP cannot be completely judged with the above analysis. Nonetheless, both element types demonstrated close agreements. Although the mode constructed with Tshell-element was shown to be slightly less accurate than the solid-element model, it is significantly more efficient in terms of CPU time consumption, yielding a 3,865% improvement in CPU consumption compared to the solid model, as shown in Table 4-9. Consequently, the model with Tshell element was selected to conduct all remaining numerical analyses.

Table 4-9 CUP time comparison between solid and Tshell elements.

	Solid elements	Tshell elements	Improvement %
CPU Time (sec)	989	25	3,856

4.1.4. Modular pole design

The modular design was implemented in this pole due to the numerous benefits outlined in Chapter 1. Due to the limitations of the experimental setup and fabrication, the maximum length of each module was set to 1000 mm, with a maximum of two modules to construct the pole. The modular design was compared to the current commercial pole design offered by RS Technologies Inc. (Tilbury, ON and St. George, UT), a leading industrial manufacturer and supplier of FRP utility structural systems. In other words, the performance of the designed modular pole was evaluated against equivalent designs by RS Technologies and other scaled pole designs reported in the existing literature.

Due to the time-consuming process of customizing a mandrel necessary for fabricating the FRP modules, both modules were designed in such a way that they could be fabricated using one mandrel. In other words, the two modules were designed such that they had the same lower cross-section diameter but different lengths, with the bottom module being smaller in length to achieve better buckling capacity. Control of the overlap region in the modular design was crucial for two reasons. Firstly, the overlap region is the second highest-stressed area after the ground line base region because the top module's base would tend to expand under loading. Secondly, overdesigning the overlap length would increase the cost. According to (ASCE, 2019), the overlap region's length should be at least 1.5 times the diameter of the upper module at the bottom. Therefore, the overlap length can be calculated by the following equation:

$$overlap\ length = L - \frac{t}{\tan(\theta)} \qquad \text{Equation 4-5}$$

where L is the pole's length, t is the pole thickness, θ is the tapered angle in degree. The detailed calculations can be found in Appendix A. A schematic diagram identifying the parameters used in the calculations is shown in

Figure 4-4.

The diameter of the cross-section at the top of each module, D_T, can be evaluated based on the base diameter, D_B, by the following equation (see also

Figure 4-4):

$$D_T = D_B - 2L\ tan(\theta) \qquad \text{Equation 4-6}$$

The dimensions of the modular poles calculated according to Equation 4-5 and Equation 4-6 are reported in Table 4-10. The detailed calculations can be found in Appendix B. As seen, the D_B is 54.2mm and the designed overlap is 135.2mm. By multiplying the D_B by 1.5, the required overlength is 81.3mm, which is well-below the designed overlap length.

Table 4-10 The Proposed modular pole design's dimensions.

Module	Length (mm)	D_T (mm)	D_B (mm)	Thickness (mm)	tapered angle (°)	Overlap length (mm)
Top	1000	47.2	54.2	2.6	0.2	135.2
Bottom	880	48.1				

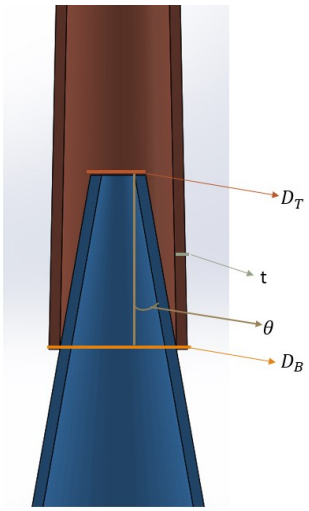

Figure 4-4 Schematic diagram of the overlap region and its parameters
(angle θ has been exaggerated for better visual).

Table 4-11 illustrated the values of the key parameters of the proposed pole and the equivalent one based on RS technologies. The key parameters are the slenderness ratio, taper angle, and ratios of top and bottom diameters to the thickness.

Table 4-11 Comparison of the proposed design key parameters with the equivalent commercially available pole.

	Designed Top module	RS Top module	Designed Bottom module	RS bottom module
Slenderness ratio	117.4	117.3	99.8	90.7
Taper	7	20.2	6.9	20.3
D_T/t	18.2	21.8	18.5	29.2
D_B/t	20.8	33.1	20.8	40.3

The slenderness ratio is calculated using the following equation (Hibbeler, 2016):

$$S = \frac{KL}{r} \qquad \text{Equation 4-7}$$

where S is the slenderness ratio, K=2 is the effective length factor and r is the radius of gyration, which can be calculated by the following equation (Hibbeler, 2016):

$$r = \sqrt{\frac{I}{A}}$$ Equation 4-8

where A is the average cross-sectional area of the tip and base areas of the pole modules.

Taper is an industrial terminology describing the change in poles' diameter per unit length, which can be calculated by the following equation(ASCE, 2019):

$$Taper = \frac{(D_B - D_T) * 1000}{L}$$ Equation 4-9

where the 1000 is a scaling factor to make taper a relatively large number for visualization. The detailed calculations can be found in Appendix C.

Subsequently, after the assemblage of the two modules of the proposed design, the entire pole's parameters were compared against the full-sized commercial pole (RS Technologies) and two scaled poles from the existing studies, as reported in Table 4-12.

Table 4-12 Comparison of the proposed pole design with the commercial pole and scaled poles from other studies.

	Proposed design (assembled)	RS Technologies	Pole #1(Altanopoulos et al., 2021)	Pole (Ibrahim, 2000)
Slenderness ratio	165.7	219.2	127.7	83.0
D_{avg}/t	20.7	27.5	19.4	65.5

4.2. 3D Scaled pole design

4.2.1. Preliminary coupon-level investigation

As discussed in the previous chapter, one of the novelties of this project is the incorporation of 3D fabric in developing stiff and long-lasting poles, which has never been attempted in past. Another novelty of the work is the incorporation of wooden dowels to (a) reinforce the fabric, thereby enhancing its overall stiffness, and (b) facilitate the

incorporation of the 3D fabric in the fabrication of cylindrical structural members. Therefore, before attempting the design, three-point bending tests were conducted to investigate the extent of stiffness enhancement that could be attained by incorporating the reinforcing dowels. As the main objective of the test was to acquire a sense of the dowels' contribution to the cylindrical geometry, the test coupons were cut directly from a cylinder, similar to the 3D pole's geometry. For that purpose, a cylinder made of WC3DFRP, and one made of 3DFRP (i.e., the unreinforced version of the WC3DFRP one) were fabricated. An ABS pipe was coated with a release agent to be used as the mandrel, using the method outlined in section 5.3.1. Then, the dowel-reinforced fabric was prepared using the same procedure described in section 4.1. Subsequently, the WC3DFRP cylinder was fabricated using a similar procedure used to fabricate the 2D pole, which will be described in detail in the next chapter. Fabrication of the 3D cylinder made of 3DFRP was similar to the WC3DFRP cylinder, except that the dowels were taken out at the time when the resin was half-cured. After fabrication, three coupons were extracted from each 3D cylinder. Each specimen had a width that included eight channels of the fabric. Half of the channels in the WC3DFRP coupons contained dowels, as seen in Figure 4-5, while all the channels in the 3DFRP coupons were empty.

The three-point flexural tests were performed in the same manner as discussed in section 3.2.1. Figure 4-6 shows the test setups for the two types of coupons with their curvature facing upward. The comparison of the results obtained for the two different materials is shown in Figure 4-7. As can be seen, the response of the 3DFRP is significantly improved by the incorporation of the dowels. Indeed, the dowels improved the stiffness and strength of the FRP by approximately 300% and 500%, respectively.

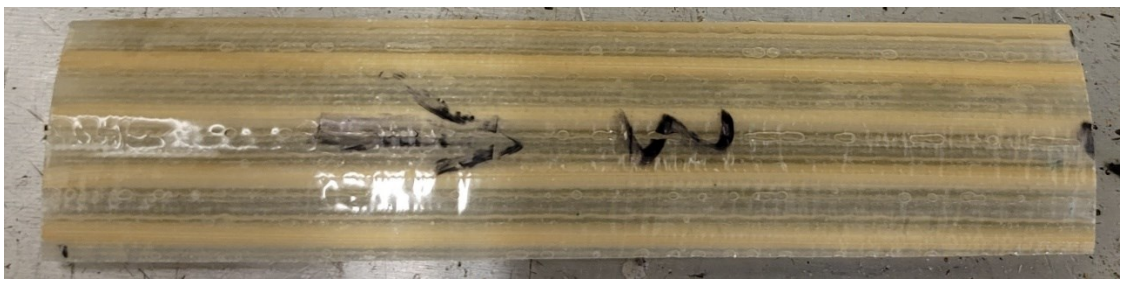

Figure 4-5 Illustration of WC3DFRP coupon's configuration for the preliminary bending test.

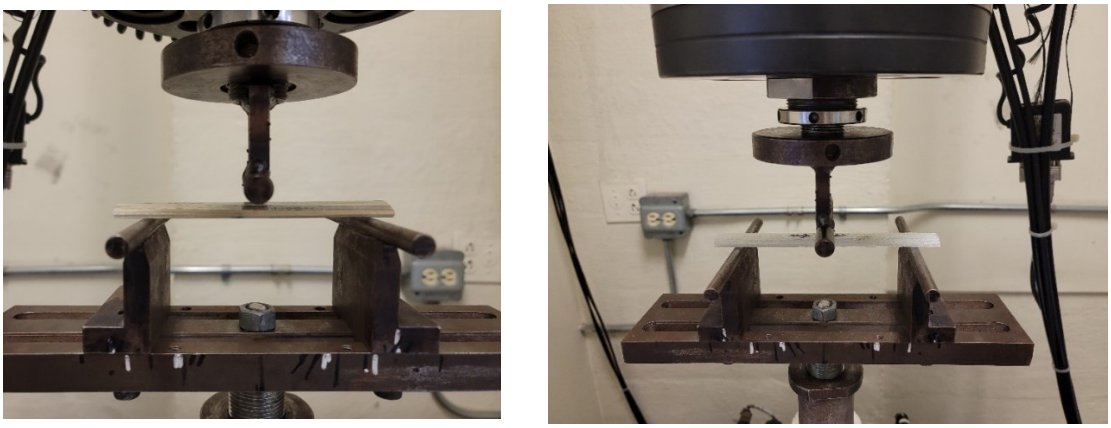

(a) (b)

Figure 4-6 Three-point flexural test setups for (a) WCGFRP and (b) 3DFRP coupons.

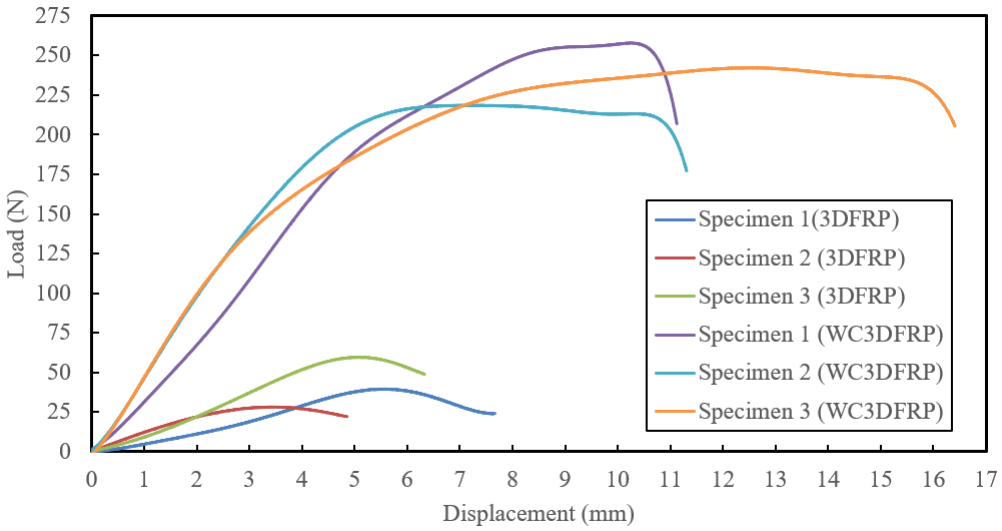

Figure 4-7 Responses of WCGFRP and 3DFRP coupons in the three-point flexural test.

4.2.2. Design compromise

In a tapered pole design, the diameter of the top and bottom of the pole would differ. This means that when constructing a pole with WC3DFRP material, the number of channels on the top portion would be fewer than the number of channels on the bottom portion. This would require partial cutting of the dowels along the length of the pole, which

would not only make fabrication impractical but also negatively affect the contribution of the dowels, leading to inconsistent stiffness along the length of the pole. As a result, a prismatic pole design had to be used as a compromise. The design procedure will be discussed in detail in a future chapter.

Table 4-13 shows the dimensions of the prismatic poles. An ABS pipe with a length of 1200 mm and a diameter of 48.5 mm was chosen as the mandrel.

Table 4-13 Dimensions of the proposed 3D poles.

	Length (mm)	OD (mm)	Thickness (mm)	Slenderness ratio
3D pole	1000	56.5	4	115.5

Chapter 5: Fabrication of the Poles

5.1. Mandrel design

5.1.1. Material selection and design

Developing a mandrel for fabricating axisymmetric composite structural members requires careful consideration of machinability and the ability to release the cured composite from the mandrel. An Acrylonitrile Butadiene Styrene (ABS) and a stainless-steel pipe were used to test the releasability of one layer of biaxial glass fabric-epoxy. To improve releasing of the composite from the mandrel, three layers of polyvinyl alcohol (PVA) mold release agent were evenly brushed to the surface of the mandrels. After laying the composites on the pipes, however, it was nearly impossible to release the specimens from the pipes at room temperature without damaging them. To address this challenge, a method was attempted by taking advantage of the difference in the coefficient of thermal expansion (CTE) of the mandrel materials and the FRP. The CTE of ABS and steel are 80×10^{-6}/°C (Polymershapes, n.d.) and 11×10^{-6}/°C (AISC, 1994) respectively. Al-Falah et al., (2014) reported FRP's CTE as 26.6×10^{-6}/°C, which is higher than steel but lower than ABS. These values suggest that the release of FRP could be facilitated by increasing the temperature of the steel pipe and decreasing that of the ABS pipe. Since the glass transition temperature of the room-cured West system 105 epoxy is relatively low at 65 °C (WEST SYSTEM, 2014), to prevent the potential damage to the composite material during mandrel removal, it would be advantageous to use an ABS mandrel instead of a steel mandrel.

In accordance with the proposed modular design outlined in Table 4-10, the mandrel's geometrical dimensions are shown in

Table 5-1. Since an ABS pipe fitting the required dimensions was not available, a grade of PVC was used instead. PVC has a similar CTE to ABS (i.e., 58×10^{-6}/°C) and a lower unit cost (VYCOM, n.d.).

Table 5-1 Dimensions of the mandrel.

	Length (mm)	Top diameter (mm)	Bottom diameter (mm)
Mandrel	1200	50	41.6

5.1.2. Mandrel fabrication

A solid PVC rod measuring 76.2 mm in diameter and 1200 mm in length underwent a turning process, as depicted in Figure 5-1. The PVC rod was secured in place by a chuck and live center, as shown in Figure 5-2, and excess material was removed until the desired shape was achieved.

Figure 5-1 The PVC cylinder is ready for turning

Figure 5-2 PVC rod being turned on Lathe.

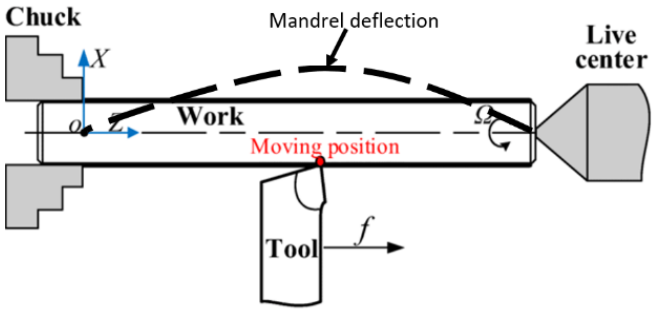

Figure 5-3 Schematic mandrel deflection during the turning (Lu et al., 2019)

Upon completion of the machining process, it was discovered that the resulting mandrel did not have the required constant taper rate. This issue arose due to the mandrel deflecting away from its constraints as the cutting tool exerted lateral force during material removal (see Figure 5-3). To address this issue, a mitigatory strategy was implemented. For that, a straight bar was secured along the mandrel, and a strip of the sanding belt was inserted between the bar and the mandrel. As the mandrel turned, the abrasive action of the sanding belt automatically straightened the mandrel by sanding out the excess material that was affecting the taper rate, as shown in Figure 5-4. The proposed mandrel dimensions were achieved after this alleviative process.

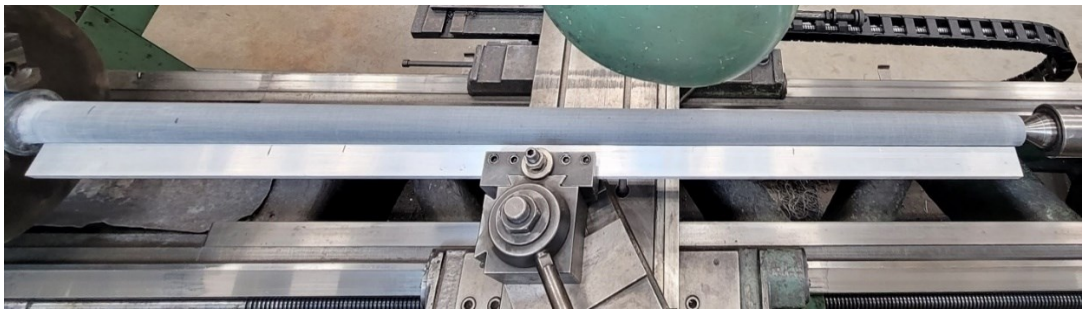

Figure 5-4 The method of resolving the inconsistent taper rate

5.2. Fabrication of the 2D poles

5.2.1. Trial and error hand layup

Axisymmetric structural members such as poles are customarily fabricated using a filament winder. With a filament winder, the fibers are placed exactly at predetermined angles using a computer-controlled process, thereby rendering a uniformly consolidated part with the desired fiber angles. However, a filament winder was not available to us. As a result, the poles had to be fabricated using the hand layup method.

The fabrication of the poles using hand layup required extensive practice and trial and error. To determine the best fabrication solution, small cylindrical specimens were first fabricated before the designed poles. The fabrication process involved several steps. Firstly, mold-release agents were applied to the mandrel, followed by the application of three layers of PVA onto the mandrel. Each layer was allowed to dry for two hours before applying the next layer. Once the PVA layers were dried, an additional layer of wax was applied for added release assurance.

The next step was to wrap the E-glass/epoxy fabric around the mandrel in the order of the designed layups, with each layer being allowed to partially cure for 45 minutes before applying the next layer. The partial curing stage allows the adhesion of the next layer onto the partially cured tacky substrate. Once all the layers had been wrapped around, a polyester shrink tape was then wound around the fabricated pole, and a heat gun was used to shrink the tape while rotating the mandrel at a constant speed to consolidate the layers as

uniformly as possible. The heat gun was kept at a distance of at least 50 mm from the tape and was moved continuously to avoid overheating the resin. In the meantime, the mandrel was continually rotated at a constant speed, slowly, until the resin was extruded through the shrink tape overlapping boundaries. The next step was to allow the resin to cure for 24 hours at room temperature. Once the resin was cured, the specimen and mandrel were placed in a chest freezer for about 30 minutes. Finally, the specimen over the mandrel was retrieved from the refrigerator, and the specimen could be released from the mandrel effortlessly by pulling and twisting them in the opposite direction.

Based on the previously proposed thickness for the modular pole, a pole with 2.6 mm, the thickness was attempted to be fabricated in the lab. First, A specimen with a layup sequence of $[+/0_4/+]$ was fabricated, and the resulting thickness was measured at 3.4 mm. Then a $[+/0_2/+]$ laminate was fabricated whose thickness was measured as 2.7 mm. However, the [+/0/+] layup with 2.3 mm thickness was selected as the final design. This was because both $[+/0_2/+]$ and [+/0/+] produced acceptable thicknesses; however, according to Equation 4-5, the modular overlap length is decreased as the thickness increases. Therefore, the [+/0/+] design could provide more tolerance in the thickness increment in the scaled poles to accommodate a sufficient overlap length. Figure 5-5 shows the variation in thicknesses of the six, four and three-layer designs. A small unevenness (bump) was developed in the [+/0/+] design by inadvertently overlapping all the layers along the same line. In the subsequent optimal layup, the overlaps were distributed alternatively at a 120° angle around the circumference as schematically shown in Figure 5-7. Finally, Figure 5-6 displays the local surface wrinkle caused by overheated shrink tape, while Figure 5-8 depicts both sides (a) and top (b) views of the final version specimen.

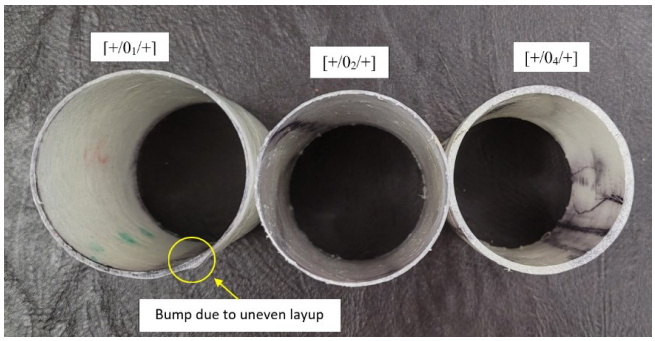

Figure 5-5 Thickness variation in the three layup designs and the overlap-induced bump.

Figure 5-6 Local surface wrinkle caused by the overheated shrink tape.

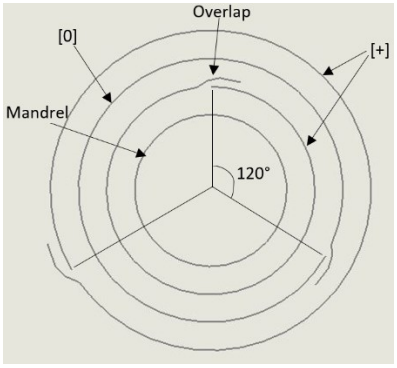

Figure 5-7 Schematic representation of staggering the overlaps in fabric layers.

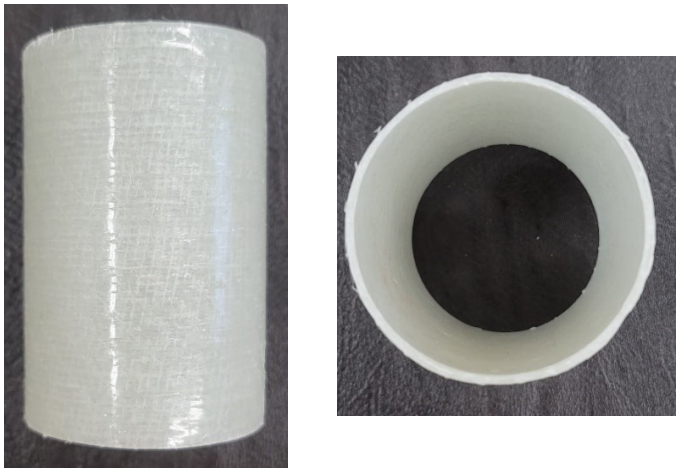

(a) (b)

Figure 5-8 (a) side view and (b) front view of the final specimen.

5.3. An innovative solution using in-house-fabricated prepreg

Winding resin-wet fabric layers around the mandrel is a time-consuming, cumbersome, and messy task. The use of prepregs would significantly alleviate the issue and allow for the wrapping of longer fabric lengths around the mandrel without the need for splicing or overlapping the fabric pieces, as was required in the attempted wet layups. However, conventional prepregs must be cured at a very high temperature, requiring a suitable oven. Since an oven capable of accommodating the pole lengths was not available at the university, an innovative solution was sought, in that pseudo-prepreg layers of fabric were developed in the lab.

The procedure started by first cutting a layer of E-glass fabric to the desired dimensions. The fabric was then weighed in order to calculate the required amount of resin, which was 1.3 times the weight of the fabric plus an additional 20 grams of waste during the application process. West System 105 resin and 206 slow hardener were mixed at a 5-to-1 ratio. The hardener provides a working time of approximately 20 minutes (WEST SYSTEM, 2014)

Next, two layers of plastic sheets, with dimensions slightly larger than the fabric dimensions, were prepared. The cut fabric was then placed onto one layer of the plastic

bagging material and the prepared resin was brushed evenly to the fabric. Given the large size of the fabric, it was necessary to apply the resin swiftly and carefully before exhausting its pot life. Subsequently, the other layer of the plastic sheet was placed on top of the resin-infused fabric, as shown in Figure 5-9(a). It was imperative to label each prepreg immediately after its preparation to avoid confusion regarding the fabric fiber orientation. Finally, the prepreg was rolled and stored in a chest freezer. Figure 5-9(b) shows the partially frozen prepreg.

(a)

(b)

Figure 5-9 Wet fabric sandwiched between two plastic sheets; (b) a view of the partially frozen prepreg.

The prepregs were then trimmed to their final dimensions, which were 1200 mm in length and 200 mm in width for the top poles and 1000 mm in length and 200 mm in width for the bottom prepregs.

Since the top and bottom circumferences of the tapered modules were different, each prepreg layer was trimmed to the approximate equivalent unwrapped trapezoidal footprint instead of a rectangular shape before laying up each module's fabrics. Templates with appropriate dimensions were prepared for cutting each layer of the prepreg, as shown in Figure 5-10.

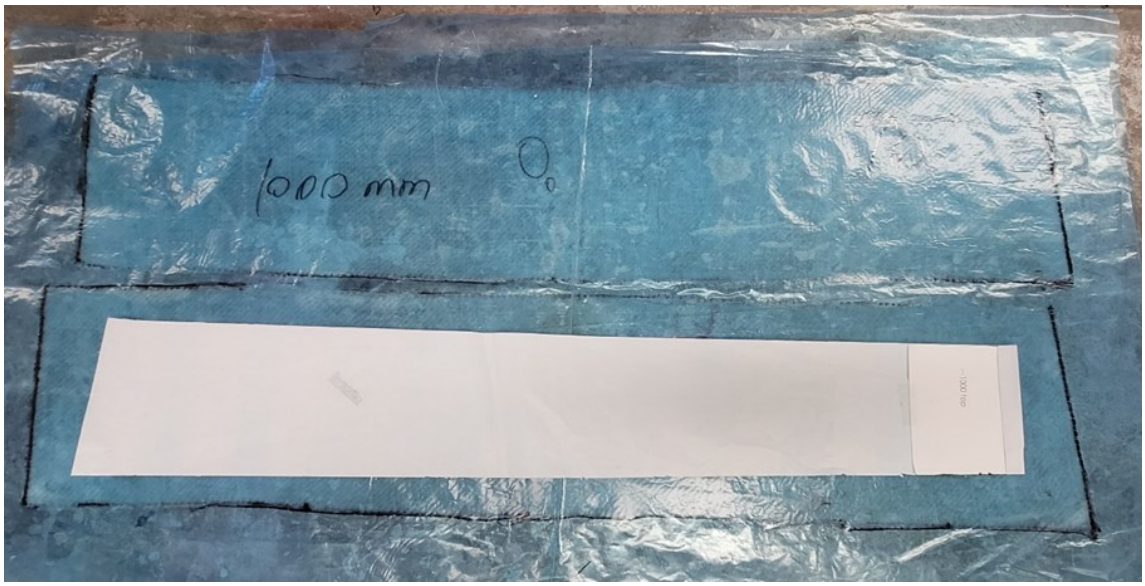

Figure 5-10 Prepreg for the top module was ready to be trimmed with a guiding template on top of it.

The following discussion applies to both the top and bottom modules of the 2D pole. The machined mandrel was prepared with PVA and wax, as described earlier. The surface finish of the mandrel after applying the release agents had a matt appearance, as shown in Figure 5-11. Since the proposed final layup was [+/0/+], a layer of biaxial prepreg was first trimmed into the exact dimensions guided by a prepared template. The fabrication procedure required two persons to wrap the trimmed prepreg onto the mandrel, as shown in Figure 5-19. The wrapping procedure involved laying the prepreg flat and removing the plastic bagging on top, carefully aligning the mandrel along the edge of the fabric, firmly pressing the mandrel to the fabric while slowly rolling it and removing its lower plastic sheet accordingly until the entire fabric was wound around the mandrel. Then, the final fabricated part was carefully inspected for wrinkles and air bubbles, which were removed

by applying additional tension to the fabric. This procedure was followed for the fabrication of each module.

Figure 5-11 Prepreg was rolled up to the surface-prepared mandrel.

The biaxial fabric was left to cure for 45 minutes until the resin thickened enough to prevent movement during the rolling of the next layer. The next layer, [0], was rolled onto the mandrel, however, the fabric edge needed to be aligned 120° around the circumference of the mandrel away from the overlap of the previous layer. The final layer of biaxial fabric was rolled using the same procedure.

A certain amount of practice was also required to successfully wrap the shrink tape along the pole to avoid any wrinkling that may occur on the surface of the pole. Figure 5-12 shows the shrink tape as being wrapped around the top module that was secured on a lathe. Finally, the module was left to cure after being heated using a heat gun, as described in the last section.

Figure 5-12 A top module wrapped with shrink tape.

A total of four modules were fabricated by repeating the above steps; these modules will be assembled to produce two poles. The top module was designed to have a tight tolerance with respect to the lower module, thereby tightly overlapping over the bottom module, especially once the pole undergoes loading. However, for better load transfer between the modules, a thin layer of epoxy was used to join them together. Using two poles to reflect the performance of the proposed design could be justified if the experimental results would be consistent. The measured dimensions of these modules are reported in Table 5-2.

5.3.1. Fabrication of 3D poles

A total of two 3D poles were fabricated. The fabric was turned into prepreg following the same procedure described previously, except the 3D fabric was cut into 1200 mm x 192 mm. The poles were also fabricated by the same procedure discussed in the last section with one difference in that before the WC3DFRP prepreg was wrapped onto the mandrel, a layer of resin was brushed on the mandrel to ensure better wetting of the inner surface of the pole. The prepared WC3DFRP prepreg before being wrapped on the mandrel is shown in Figure 5-13. Figure 5-14 shows the final step of the fabrication after the shrink tape was wound around the pole and heated with a heat gun. The process was repeated to fabricate the second pole. The physical dimensions of the two poles are shown in Table 5-3. Finally, Figure 5-15 shows the fabricated 2D and 3D poles.

Table 5-2 Measured dimensions of the fabricated FRP pole modules.

	Length (mm)	D_T (mm)	D_B (mm)	Thickness (mm)	Weight (g)	Overlap length (mm)
Pole 1 top module	1002	48.2	53.9	2.5	395.5	160
Pole 1 bottom module	882	49.1	53.5	2.3	374.5	
Pole 2 top module	1002	48.1	53.8	2.4	391.4	160
Pole 2 bottom module	882	49.1	53.5	2.3	359.6	

Figure 5-13 Fabrication of the WCGFRP before rolling on the mandrel.

Figure 5-14 A 3D pole wrapped with shrink tap after heating.

Table 5-3 Measured dimensions of the fabricated 3D poles.

	Length (mm)	OD (mm)	Thickness (mm)	Weight (g)
3D pole 1	1,005	56.0	3.8	435.7
3D pole 2	1,005	55.8	3.7	409.1

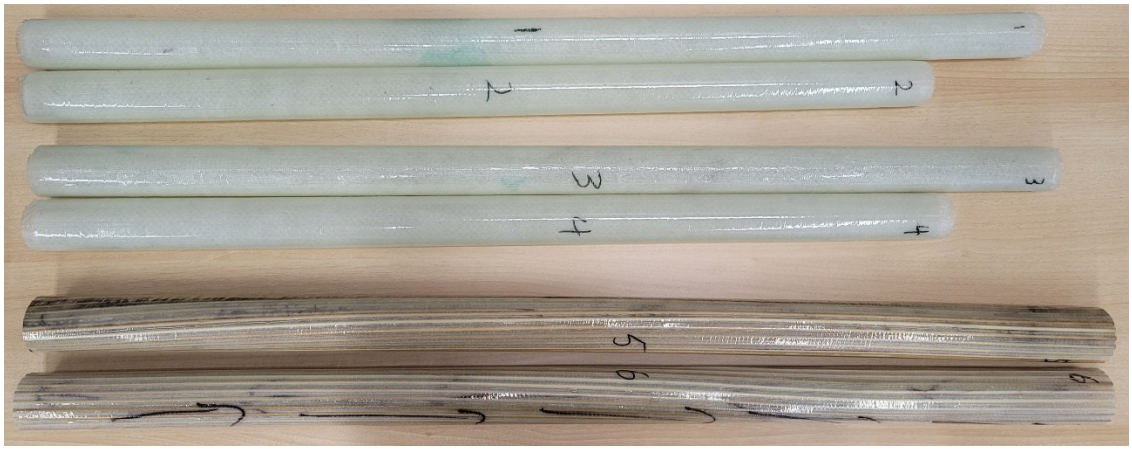

Figure 5-15 The fabricated 2D and 3D poles.

5.4. Load attachment

During the cantilever pole tests, the applied load was applied to each pole through a scissor jack attached to a load cell. The jack facilitated gradual and speed-controlled loading, and it could travel a reasonable distance as the pole deflected. A load attachment device was designed to allow the arc motion at the poles' tip while being loaded and undergoing large deflection. The load attachment device consisted of a loading ring attached to the pole and a loading knob attached to the load cell, which was screwed on the jack. The working principle of the load attachment is that the loading nob with a half-cylinder shape fits into the groove underneath the loading ring. The grove on the rings was adequately large to accommodate easy movement/rotation of the pole on the loading knob. The loading ring's inner diameter was equal to the outside diameters of the 2D, mounted at 110 mm below tip of the poles. The details of the load transfer nobs can be found in the

CAD drawings included in Appendix D. The loading rings and loading knob made of hardwood are shown in

Figure 5-16. Then, the rings were assembled on the 2D and 3D poles at 110 mm and 40 mm from the tips, respectively.

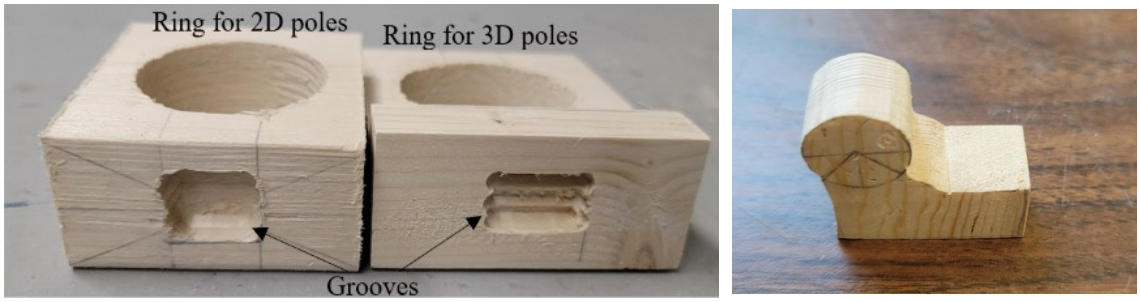

(a) (b)

Figure 5-16 Fabricated (a) load rings and (b) loading nob.

5.5. Poles restraining fixture

To replicate the actual in-situ boundary conditions, the poles were embedded in concrete. The bottom portions of both 2D and 3D poles were first infilled with concrete up to their respective fixed (cantilever) lengths of 235 mm and 140, respectively. Figure 5-17 illustrates the end-filled portion of the poles' cross-sections, with numbers 2 and 4 representing the 2D poles, and numbers 5 and 6 representing the 3D poles.

To poles were subsequently embedded in the cavities of hollow concrete blocks measuring 190.5 mm high and were used as external fixtures. The poles were inserted into the blocks, and the surrounding space was filled with concrete. Since the height of the blocks exceeded the fixture length of the 3D poles, the hollow space was filled to the appropriate level. In the case of 2D poles, the block height was less than the 235 mm restraining length. However, the concrete inside the poles provided sufficient stiffness and strength to constrain the poles at the desired length. Therefore, the constraint heights

represent the in-service poles' embedded groundline. Please refer to Figure 5-18 and Figure 5-19 for a complete illustration of the fixture setup for the 2D and 3D poles, respectively.

Figure 5-17 Cross-sectional view of the partially concrete-filled poles.

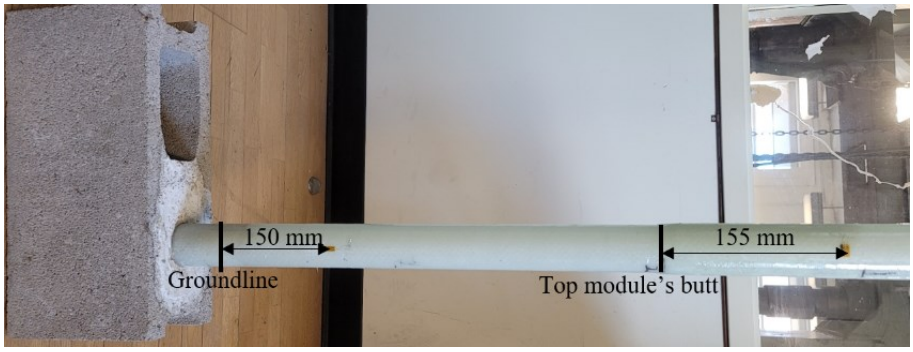

Figure 5-18 The strain gauges' locations along the 2D poles.

Figure 5-19 The strain gauges' locations along the 3D poles.

5.5.1. Data acquisition

5.5.2. Strain gauges

Individual 350 Ω strain gauges (OMEGA SGD-10/350-LY41) were implemented to measure the tensile and compressive strains developed on all the poles and hoop strains on the 2D poles. The hoop strain in the 3D poles was not monitored due to the relatively thick-wall configuration of the 3D poles, which makes local buckling failure unlikely. The strain was measured by connecting each strain gauge to a strain measurement module NI 9237 Strain/Bridge Input Module (National Instruments, Austin, TX), through a screw terminal. The strain gauges used in this experiment were quarter-bridge type; therefore, the bridge completion was accommodated using NI 9944 terminal blocks before connecting the gauges to the Bridge Input Module. The complete wiring configuration for the strain measurement and the pin layout of the NI 9237 Voltage Input Module is shown in Appendix E. Two strain gauges were placed 150 mm above the groundline on the tensile and compressive sides of the 2D poles. The strain gauge measuring the strain change in the hoop direction due to the compressive load was placed 155 mm above the lower end of the top module. Figure 5-18 shows strain gauge locations for the 2D poles, where the black line represents the top module's lower end. The strain gauges were placed 135 mm above the groundline on the tensile and compressive sides of the 3D poles, as shown in Figure 5-19.

5.5.3. Load cell

A 100 Kgf capacity OMEGA LCM/111-100 load cell (Omega Engineering, St-Eustache QC), was used to measure the applied load. As the load cell operates on the same principle as the strain gauge, the NI 9237 module was used to power and receive the output voltage signal from the load cell. However, since the resistors of the load cell were configured as the full bridge instead of quarter bridge, the wires of the loadcell were connected to an NI 9949 RJ50 screw terminal, which routes the input and output signals to the RJ50 receptacles in NI 9237, which is subsequently hosted by Compact DAQ NI Chassis cDAQ-9172, which is connected to a laptop. The pin layout of NI 9949 and the

full bridge connection configuration can be found in Appendix F. As previously mentioned, the load cell was installed between the jack and the load knob to measure the reaction loads from the pole's tips. Figure 5-20 shows the load cell fastened on the jack connected to the NI 9949.

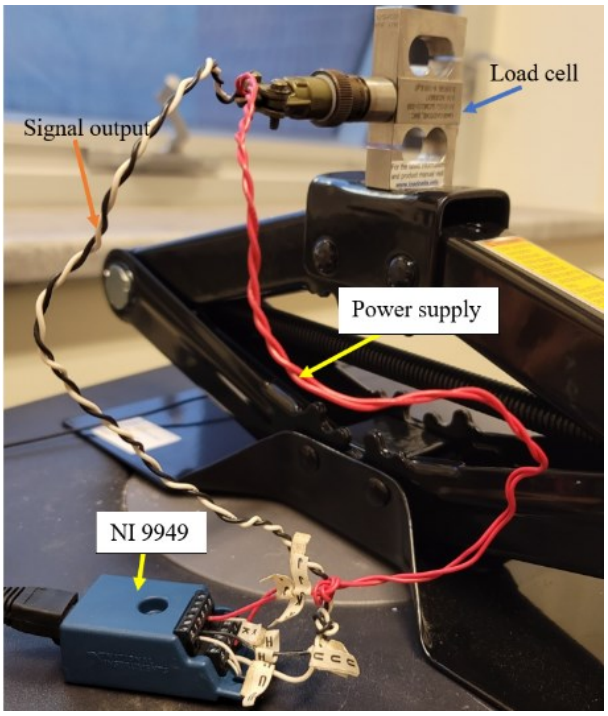

Figure 5-20 Load cell fastened on the jack connected to the NI 9949.

Chapter 6: Tests of Scaled Poles and Performance Comparison

This chapter describes the experimental investigation conducted to examine the performance of the 2D and 3D poles and their respective FE models' calibration based on the experimental results. Finally, a 3D pole with comparable weight to the 2D pole is modelled using LS-DYAN. The numerically evaluated performance of this pole will be compared with the performance of the 2D prismatic pole obtained numerically using the finite element method (FEM). The experimentally acquired displacement, load and strain data are used to verify the integrity of the numerical models. During the tests, displacement values were manually recorded by projecting the laser pointers from the desired locations of the poles to whiteboards. Meanwhile, the load and strain data were automatically collected using the data acquisition (DAQ) system in conjunction with LabView software with a minimum sampling rate of 1612.9 Hz.

6.1. 2D scaled poles

6.1.1. Experimental investigation

The experimental setups of the 2D and 3D poles are very similar. Therefore, only one pole's setup is discussed here.

Firstly, the block holding the pole was clamped on a steel-frame workbench which was bolted to the ground. A metal plate was placed on top of a concrete block to avoid damage to the block due to clamping forces. Four heave-duty clamps were used as illustrated in Figure 6-1. On the other end, the pole's tip was secured through the load transfer knob and load cell to a scissor jack with a 384 mm lifting limit, as discussed in section 5.5.3. and illustrated in Figure 6-2. The jack was secured in a vise, which sat on five metal blocks.

Figure 6-1 Fixture setup for 2D poles

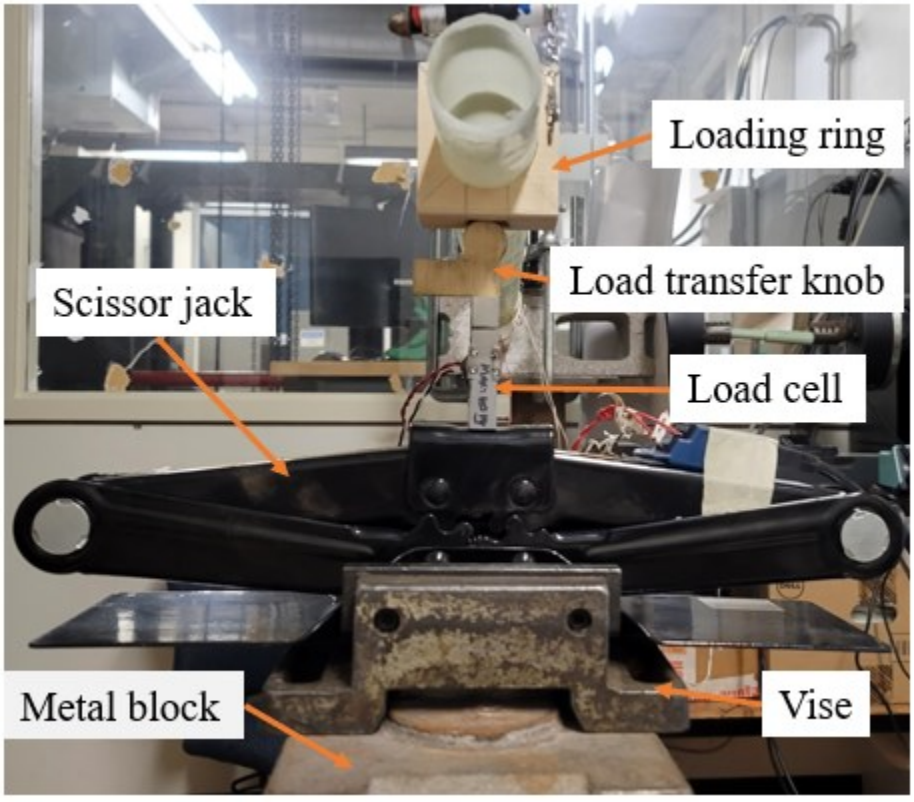

Figure 6-2 Loading setup near the tip of the 2D pole

Displacements were manually recorded during the test at the tip and midspan of the pole using laser pointers. Specifically, the midspan coincides with the butt-end of the top module of the pole (see

Figure 6-3) The laser pointers were glued orthogonally at those locations. During the test, the lasers were projected onto two whiteboards, and their travelled trajectories were manually marked at specific load increments using a pin.

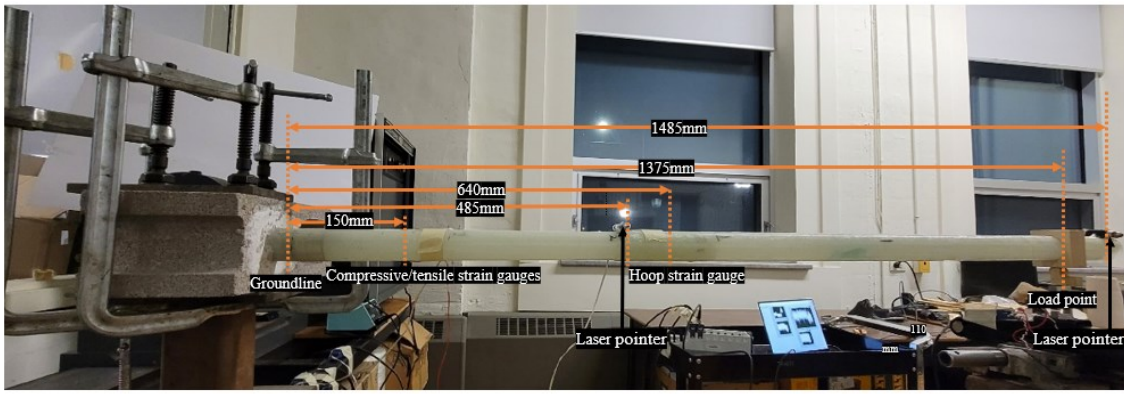

Figure 6-3 An overall view of the experimental setup of the 2D poles

Then, the strain gauges were wired and connected to the NI 9944 quarter-bridge adapter and subsequently to NI 9237 module which was hosted by the DAQ chassis 9172 as discussed in section 5.5.2. Figure 6-4 shows the strain gauge mounted for measuring the strain in the hoop direction. The load cell was also connected to the same module. A LabView program was used to control the data acquisition process, including the start and end of the acquisition, sampling rate, data saving, and the transducers' calibration. The program's flowchart can be found in Appendix G. All the transducers were calibrated and offset to zero readings before the test began.

Figure 6-4 The strain gauge mounted for measuring the hoop strain.

Two persons were required to perform this test; one raised the jack, and another one recorded the displacement. The pole's tip was steadily raised at a constant speed at an approximate rate of 0.25 mm/sec, and stopped at a predetermined interval. The lead screw inside the jack ensures the jack's slow and smooth motion. The operation was stopped to record the displacements and their corresponding loads after every three complete rotations of the jack's crank until the test ended. Due to the quite large slenderness ratio of the pole, the pole did not fail when the jack's lifting limit was reached. A clamp was used between the vise and steel blocks to maintain jack's stability as it raised, as seen in Figure 6-5. Once the jack reaches its travel limit, the test was interrupted, and three additional steel blocks and one concrete block were placed underneath the vise to extend the pole's displacement. Note that the pole underwent linear elastic displacement, thus, the test could be followed accordingly. However, despite the additional imposed displacement, the failure of the pole could not be achieved as the jack reached its travel limit once again. The process was repeated for testing the second pole.

Figure 6-5 Jack reached its lifting limit.

6.1.2. FE model

An FE model was constructed to simulate the described test in LS-DYNA FE software environment. Due to the symmetry, only half of the pole was modelled using the Tshell element of LS-DYNA. The model was constructed with the actual dimensions of the tested poles, tabulated in Table 6-1. To apply the boundary condition, all the inner surface nodes within 235 mm distance measured from the bottom edge of the pole were fully constrained (identified with red triangular symbols in Figure 6-6(a)). The loading ring was meshed using rigid elements and was put in contact with the pole mesh using an appropriate contact algorithm (CONTACT_AUTOMATIC_TIE_BREAK). The pole was loaded laterally using applied displacement of 550 mm applied to the appropriate location on the loading ring to simulate the real condition. The nodes between the top and bottom modules within the overlap region were merged because no failure was observed within the overlap regions at the end of the experiments. Figure 6-6(b) shows how the overlap region was conducted in the FE model, where the meshes in blue and red represent the bottom and top modules, respectively. The thicknesses of each biaxial and UD fabric layer were assumed as 0.8 mm and 0.65 mm, respectively. The damage model MAT_054_ENHANCED_COMPSOITE_DAMAGE was implemented, and the values of mechanical properties are estimated based on the data provided by Ekşi and Genel (2017), as shown in Table 6-2.

Table 6-1 Dimensions for each module of the 2D pole.

Module	Length (mm)	D_T (mm)	D_B (mm)	Thickness (mm)	Overlap Length (mm)
Top	1000	48	54	2.3	155
Bottom	880	49	54		

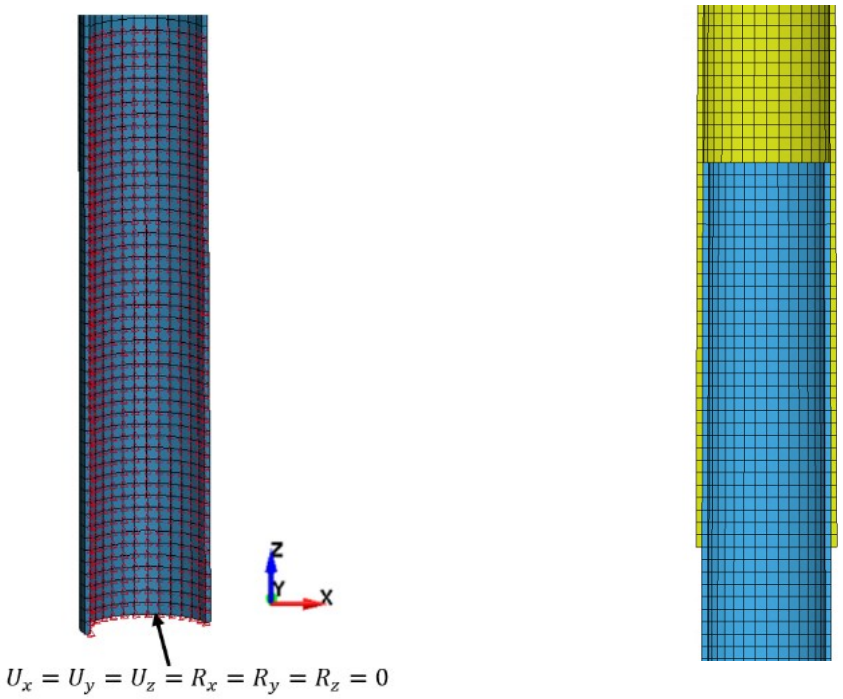

(a) (b)

Figure 6-6 (a) Illustration of boundary conditions accounting for the fixture and (b) the overlap region's mesh.

Table 6-2 Mechanical properties used in the FE model.

Fabric Type	$\boldsymbol{\rho}$ $(\boldsymbol{g/mm^3})$	$\boldsymbol{E_{11}}$ (M$\boldsymbol{Pa}$)	$\boldsymbol{E_{22}}$ (M$\boldsymbol{Pa}$)	$\boldsymbol{\upsilon_{21}}$	$\boldsymbol{G_{12}}$ (M$\boldsymbol{Pa}$)	$\boldsymbol{G_{23}}$ (M$\boldsymbol{Pa}$)	$\boldsymbol{G_{31}}$ (M$\boldsymbol{Pa}$)
	0.00175	15,560	6,749	0.11	3,310.8	2,595.8	3,310.8
UD	$\boldsymbol{X_C}$ (M$\boldsymbol{Pa}$)	$\boldsymbol{X_T}$ (M$\boldsymbol{Pa}$)	$\boldsymbol{Y_C}$ (M$\boldsymbol{Pa}$)	$\boldsymbol{Y_T}$ (M$\boldsymbol{Pa}$)	$\boldsymbol{S_{12}}$ (M$\boldsymbol{Pa}$)		
	343.3	572.2	80.1	78	30.9		
	$\boldsymbol{\rho}$ $(\boldsymbol{g/mm^3})$	$\boldsymbol{E_{11}}$ (M$\boldsymbol{Pa}$)	$\boldsymbol{E_{22}}$ (M$\boldsymbol{Pa}$)	$\boldsymbol{\upsilon_{21}}$	$\boldsymbol{G_{12}}$ (M$\boldsymbol{Pa}$)	$\boldsymbol{G_{23}}$ (M$\boldsymbol{Pa}$)	$\boldsymbol{G_{31}}$ (M$\boldsymbol{Pa}$)
Biaxial	0.00175	9,336	4,049.4	0.11	1,986.4	1,557.5	1,655.4
[+]	$\boldsymbol{X_C}$ (M$\boldsymbol{Pa}$)	$\boldsymbol{X_T}$ (M$\boldsymbol{Pa}$)	$\boldsymbol{Y_C}$ (M$\boldsymbol{Pa}$)	$\boldsymbol{Y_T}$ (M$\boldsymbol{Pa}$)	$\boldsymbol{S_{12}}$ (M$\boldsymbol{Pa}$)		
	223.1	343.3	48.1	46.8	18.5		

6.1.3. Results and discussion

A sampling rate of 1613 Hz was set for data collected by all the transducers, which facilitates reasonable data management. It should be noted that while load cell data was continually recorded by the DAQ, the displacement and also the load were manually recorded at each lading increment (i.e., after three revolutions of the jack crank). A Python code was developed to identify the exact load values and their corresponding strain values based on the manually recorded input load increment data since the recorded output files were too large to be viewed by MS Excel, despite the lowest allowable sampling rate was set in NI 9237. The program's flowchart for post-processing the strain results is included in Appendix H. Figure 6-7 shows the displacement trajectories recorded at the two locations during the test. The displacements were measured vertically with respect to the first marked point (lowest point).

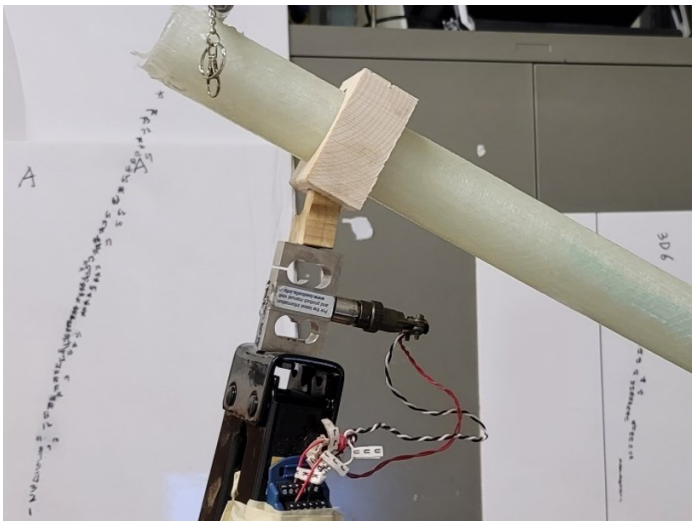

Figure 6-7 Trajectory of the tip displacement recorded on a whiteboard during the tests

Figure 6-8 shows comparisons of the load-deflection response of the 2D poles obtained at the tip and mid-span experimentally and numerically. As can be seen, the numerical results closely agree with the experimental results, and the responses of the two tested poles are also quite consistent. The predicted pole stiffness by FEM is slightly lower than the

stiffness of the actual poles up to a deflection value of 310 mm, after which it shows a slightly stiffer response. It is believed that the actual pole experiences slight softening due to the development of microcracks within the layer interfaces, which cannot be accounted for by the model.

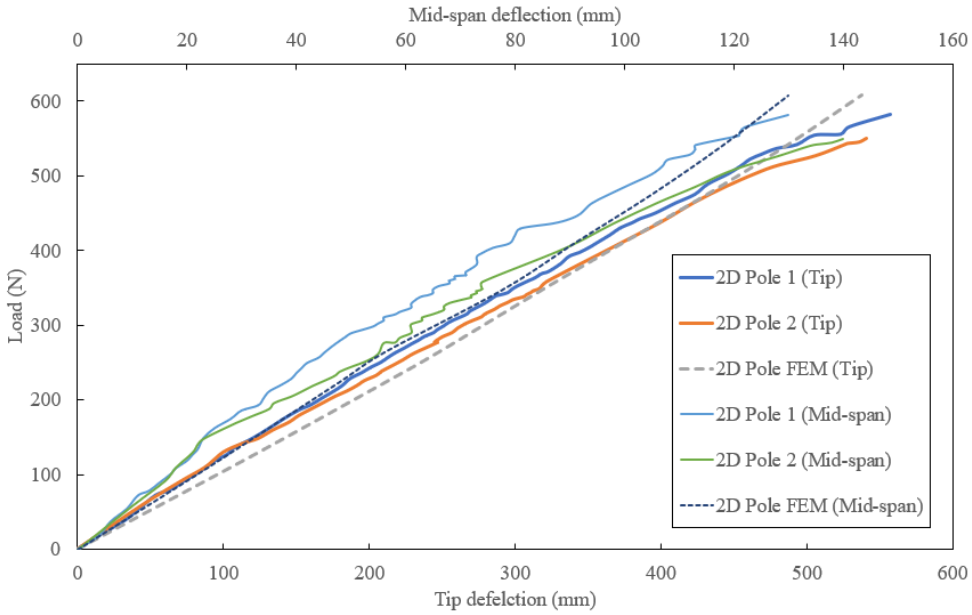

Figure 6-8 Comparison of the experimental and numerical load-deflection curves of the 2D poles at the tip and mid-span.

It should be noted that the more nonlinear responses in the mid-span curves are partially due to the measurement resolution. That is, at such low values of deflection, the change in the deflection at each measurement increment was smaller than the projected radius of the laser beam on the whiteboard. Hence, the manually pinned locations were less accurate than those at the tip, where the displacement increments were larger. The use of a Linear Variable Differential Transformer (LVDT) or a laser pointer with a more focused beam could have resolved this issue. While an LVDT was available in the lab, however, the deflection range observed would have surpassed the stroke limit of the LVDT.

The average experimental and numerically predicted stiffness values are obtained based on the load to tip-deflection and reported in Table 6-3. The percentage error of the numerically predicted stiffness is only 3.1%, which is very low, thus, validating the numerical model's integrity. The noted moment of inertia values were calculated based on

an equivalent prismatic pole, using Equation 4-3, with D_o and D_i taken as the average diameters at the top and bottom of the fabricated poles as noted in Table 5-2. The equivalent elastic modulus is then calculated using Equation 4-2.

Table 6-3 Comparison of the averaged experimental and the numerical results.

	Moment of inertia, I (mm^4)	E_x (MPa)	Stiffness (N·mm^2)	% Error in E_x
Experiment	105,765.6	9,117.9	9.64E+8	3.1
FEM	100,395.9	9,399.1	9.43E+8	

Figure 6-9 shows the comparison of the experimental and numerically predicted compressive and tensile strains as a function of the tip deflection. Both strains were measured at a location 150 mm above the groundline, as illustrated in

Figure 6-3, and numerically predicted strains were sampled at the same locations. For compressive strains, overall, Pole 1 shows slightly higher strains compared with pole 2. The numerically predicted compressive strains agree very closely with the results of pole 2 until about 240 mm of deflection, after which, the predicted strain is slightly higher. The maximum numerical strain reaches -0.018 mm/mm at approximately 540 mm deflection compared with the experimental strain of -0.015 mm/mm at the same deflection value.

As seen the tensile experimental strain-deflection curves seen in the same figure are quite consistent. The numerically predicted strains are slightly higher than the experimental values up to tip deflection of 190 mm tip deflection after which the actual poles undergo inelastic deformation. This is due to the nature of the finite element method, which predicts the response of structural components slightly stiffer than the actual cases. Moreover, the values of the maximum compressive and tensile strains are about the same for both the experimentally measured and the numerically predicted values.

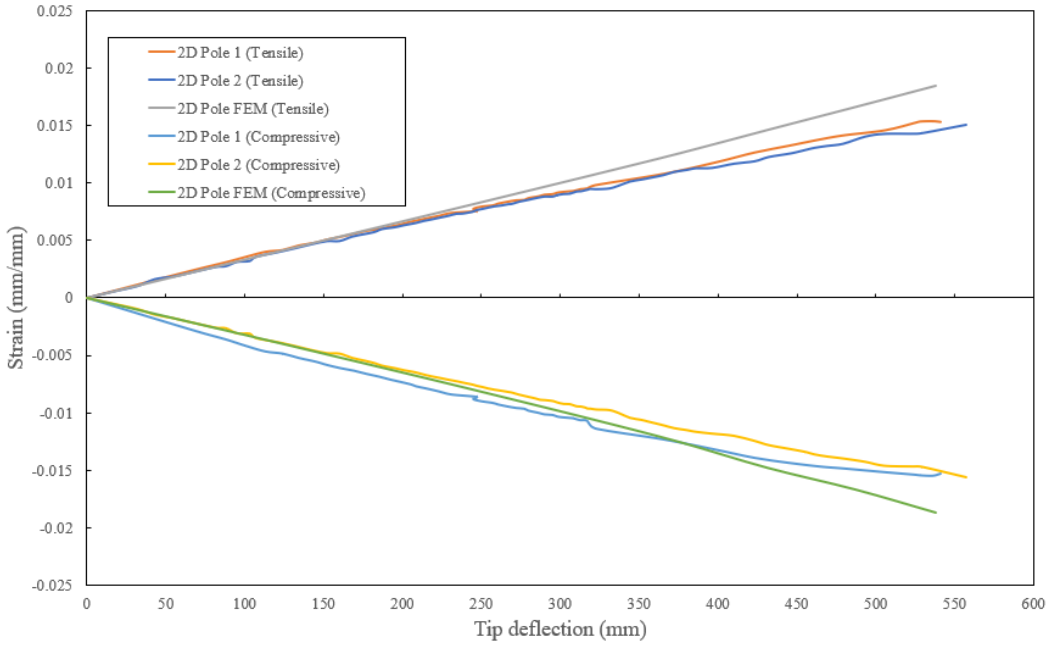

Figure 6-9 Comparison of experimental and FE tensile-tip deflection curves for 2D poles.

Variation of the hoop strain against the tip deflection is plotted in Figure 6-10. The predicted numerical values agree well with the experiment values up to a stage where the poles undergo inelastic deformation. Moreover, based on the variation of the hoop strain in the two poles, the poles exhibit somewhat of a different inelastic response as the applied deflection (load) increases. This noticeable strain difference between the two poles reaches approximately 0.0002 mm/mm at 528mm deflection, or 24% in difference. The difference is postulated to be due to the slight difference in the overlap length between the poles modules and the inevitable factors such as voids and their nonuniform distribution, and the potential local fiber misalignment, which often occurs in non-vacuum assisted hand layup process. Therefore, minimizing the inevitable uncertainties in the modular pole's manufacturing process is crucial. It should be noted that the filament-wound automated manufacturing process, which is commercially employed, resolves a great portion of such anomalies.

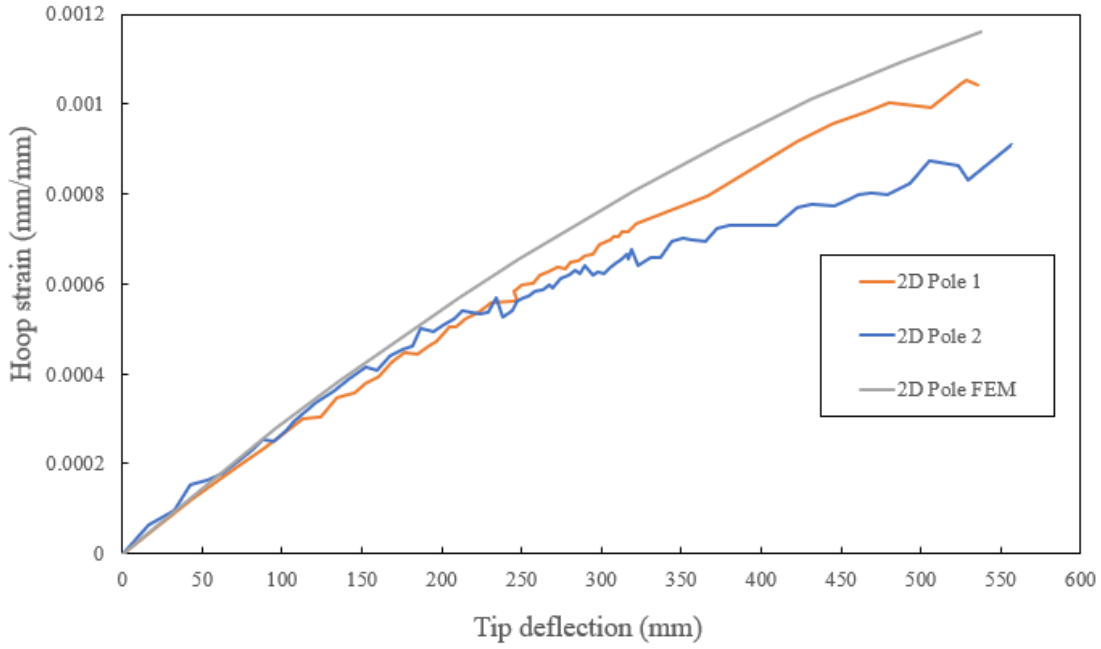

Figure 6-10 Comparison of the experimental and numerically predicted hoop strain of the 2D poles.

6.2. 3D scaled poles

6.2.1. Experimental investigation

The test method of the 3D poles followed the same procedure as the 2D poles, as discussed in section 6.1.1. During the tests, only the deflection at the tip was measured in these poles. Figure 6-11 shows the test setup for the 3D poles. As discussed in section 5.5.2. two strain gauges, measuring tensile and compressive strains, were mounted on the unreinforced channels of the poles as illustrated in Figure 6-12. Pole 1 was tested until it was damaged (though not failed entirely), and pole 2 was tested until its total failure.

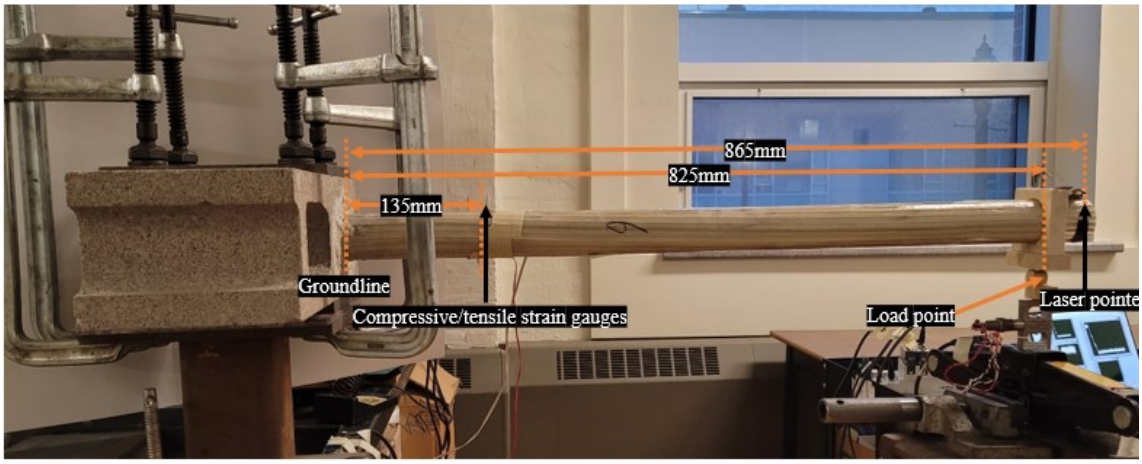

Figure 6-11 Experimental setup of 3D poles.

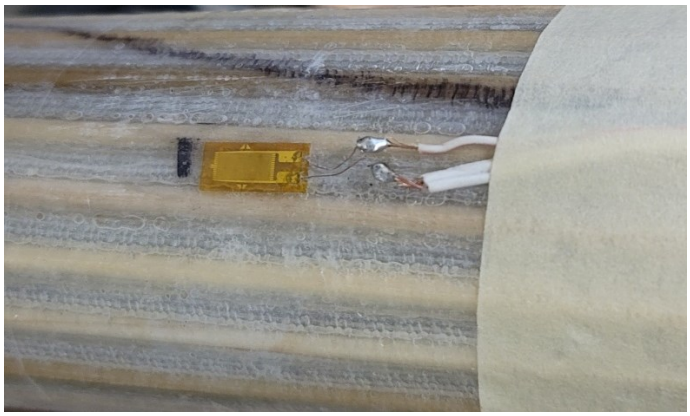

Figure 6-12 Strain gauge mounted on the unreinforced channel of the 3D pole.

6.2.2. FE model

A FE model was constructed to simulate the 3D poles' response using the implicit solution. Due to symmetry, half of the pole was modelled for computational efficiency. The dimensions of the 3D pole used in the FE model are shown in

Table 6-4. The geometry of the WC3DFRP was constructed according to Figure 3-6, except that the upper and lower plies were 0.3 mm thick. The dowel supporting the channels' height can be estimated as the incompressible material under the 17.2 MPa maximum compressive stress that could be developed by the shrink tape (Road, 2013). Hence, the fabric plies are considered to be slightly more

consolidated than the 3D composite from which the coupons were extracted. The pole was fixed along 140 mm measured from its end, as discussed in section 5.5. ; therefore, only the nodes at the inner surface of the pole were fully constrained (identified by yellow triangular symbols in Figure 6-13). In the 2D pole's model, a slid ring was also added near the tip to which displacement was applied to load the pole. Figure 6-14 illustrates how the loading ring was attached to the pole using the surface-to-surface contact algorithm of LS-DYNA. The rest of the model (i.e., the element type, material properties, etc.) follows the FE model of the WC3DFRP coupon as discussed in section 3.2.2. However, the contract relations between the dowels/plies and dowel/pillars were removed to resolve the instability issue prompted by LS-DYNA implicit solver. Besides, the compressive strain (ε_{C1}) property of the composite was reduced to -0.02 to compensate for the fabrication induced flaws of the pole as briefly discussed in the last section.

Table 6-4 Dimensions of the 3D pole used to develop the FE model

	Length (mm)	OD (mm)	Thickness (mm)
3D Pole	1005.0	52.0	3.8

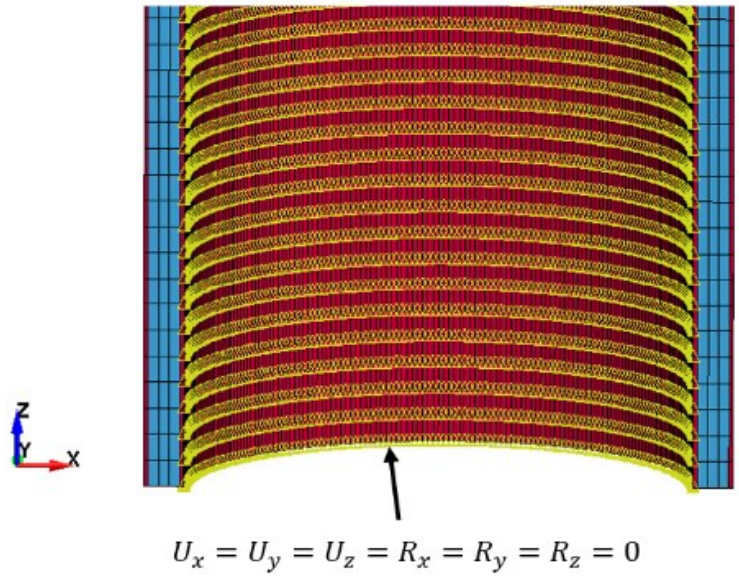

Figure 6-13 Nodes fully constrained on the inner surface of the pole.

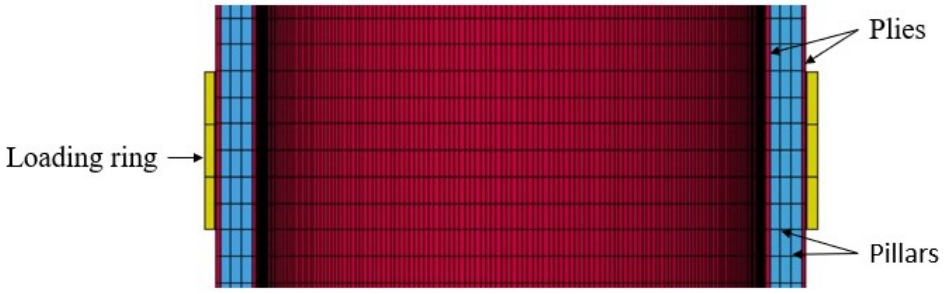

Figure 6-14 Illustration of load ring attached to the pole using contact algorithm.

6.2.3. Results and discussion

The comparison of the experimental and numerically predicted load-tip deflection curves is shown in Figure 6-15. The predicted response matched closely to the experimentally observed, up to the poles' failure. Pole 1 has a slightly higher failure strength of 384 N at 79 mm tip deflection, while pole 2 revealed its failure strength of 371 N at 77 mm deflection. The FE model's prediction indicates the pole's failure at a slightly lower deflection (75.2 mm) compared with the experimental results, and its failure load magnitude of 380 N is in between the failure strength of the two experimental poles. Following the procedure discussed in section 6.1.3. , the Effective elastic modulus, E_x, values of the actual poles and FE pole were computed and reported in Table 6-5. As can be seen, the difference is 0.89%. Due to the complexity of the cross-sectional geometry, the moment of inertia was obtained from SolidWorks. In comparison with the experimental elastic modulus of the flexural and compression tests, the pole's E_x is only 5.3% lower and 8.5% higher, respectively, which is expected.

As seen in Figure 6-15, Pole 2's endures significant load after attaining its ultimate strength and its ultimate strength gradually decreased to 262 N before it was fully fractured at 220mm deflection. This occurred concurrently with the development of ply failure at a distance 30 mm above the groundline along an empty channel on the compression side, as seen in Figure 6-16 (a) followed by a compression failure observed at the groundline after the fracture, shown in Figure 6-16 (b).

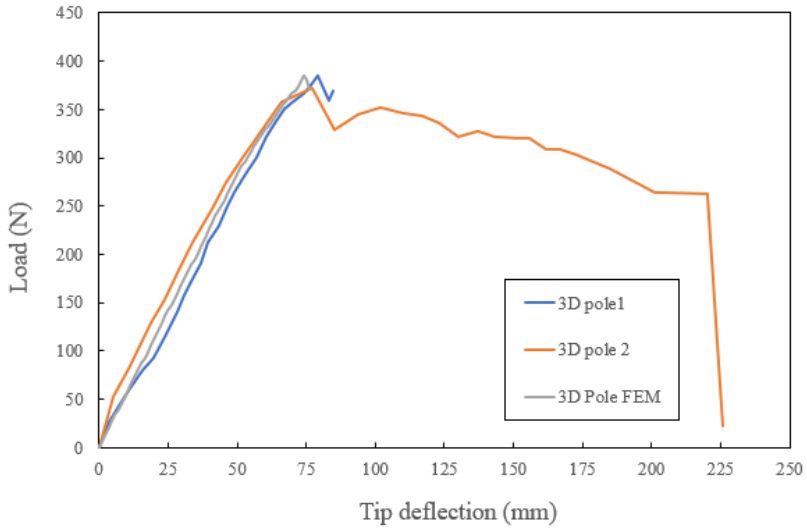

Figure 6-15 Comparison of the experimental and numerically predicted load-deflection curves.

Table 6-5 Comparison of the averaged elastic modulus calculated based on the experimental and numerical results.

	Moment of inertia, I (mm^4)	E_x (MPa)	Stiffness (N·mm^2)	% Error in E_x
Experiment	115,149.5	9,726.5	1.12E+9	0.89
FEM		9,639.6	1.11E+9	

(a) (b)

Figure 6-16 Typical experimentally observed (a) Ply failure and (b) pole failure.

Figure 6-17 shows the compressive and tensile strain versus tip deflection curves for the actual poles and the numerically predicted results. For compressive strains, pole 2's strain values are slightly higher than pole 1's from the beginning until it fails at the ultimate compressive strain of 0.0049 mm/mm, which is very close to pole 1's ultimate compressive strain of 0.0051mm/mm. The compressive strain values for both actual poles begin to decrease at approximately the same deflections at which the load also decreased. The compressive curve for the FE model has a similar trend to the experimental curves with about the same strain value and noticeably closer to the second pole.

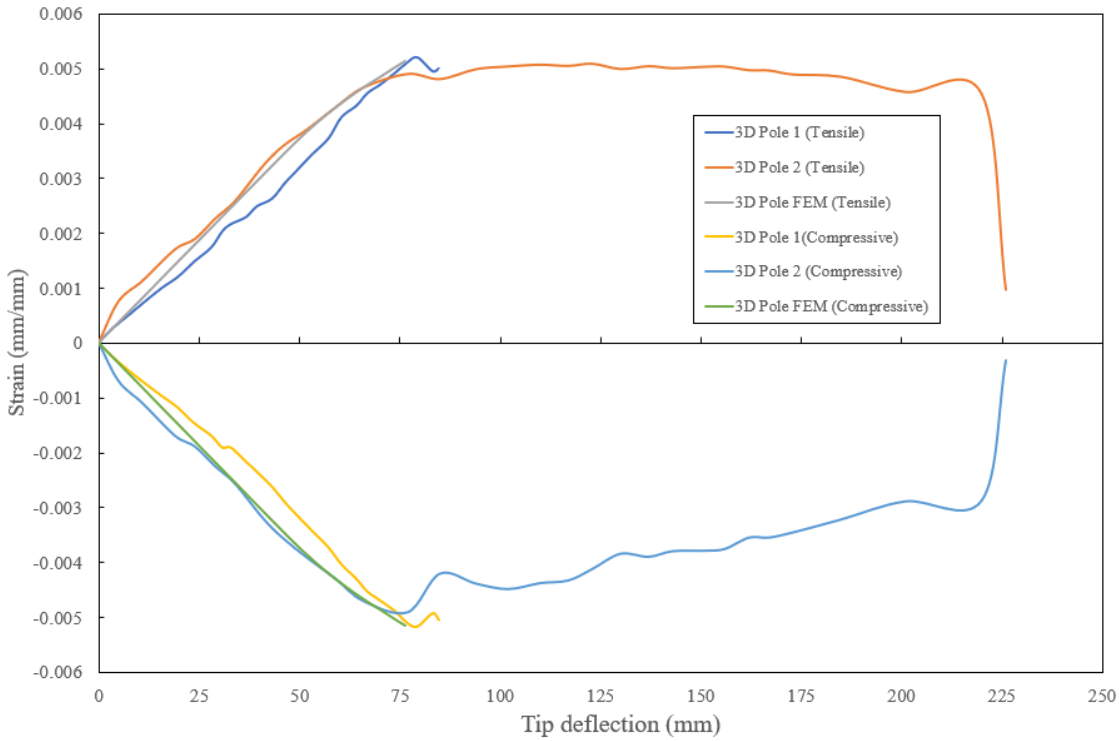

Figure 6-17 Comparison of experimental and FE strain-tip deflection curves for 3D poles.

As for the tensile strains, also seen in

Figure 6-17, the numerically predicted tensile strain values compare very closely to the experimental values. The ultimate experimental and FE strains and their corresponding deflections are almost identical to that observed on the compression side of the poles. Unlike the variation in the compressive strain, pole 2's tensile strain remains almost

constant after reaching its ultimate value up to a deflection of 185 mm. This suggests that the damage on the compression side of the pole was greater than on its tensile side, which is apparent in Figure 6-16 (b). This is due to the inherent nature of this hybrid 3D composite, whose tensile load-bearing capacity is greater than its compressive capacity, a response similar to aramid reinforced composites.

6.3. Comparison of the performances of 2D and 3D poles

The performances of the two types of poles are compared by normalizing their ultimate strength to their masses. Since the tested 3D poles were shorter and prismatic and the 2D poles were longer and non-prismatic, they could not be compared directly. Therefore, the response of a 3D pole with the same length as the 2D pole is simulated using LS-DYNA. The outside diameter of this 3D pole is the average of the outside top and bottom diameters of the 2D pole. Additionally, for more consistency, an equivalent prismatic 2D pole is also considered to investigate the effect of the modular design of the 2D pole in comparison to the monolithic pole. The length and outside diameter of this prismatic 2D pole are the same as the longer 3D pole. The exact geometric values for both the longer 3D and prismatic 2D poles are reported in Table 6-6.

Table 6-6 Summary of dimensions used in extruded 3D and 2D prismatic pole FE models.

	Length (mm)	OD (mm)	Thickness (mm)
Long prismatic 3D Pole	1735	48	3.6
Prismatic 2D Pole	1735	48	2.3

Since the 2D poles' failure mode could not be obtained in the experiments, their failure load was predicted using the FE simulation, as tabulated in Table 6-8. A performance comparison between the 2D and 3D poles conducted using FE models is shown in

Figure 6-18. As can be seen, the modular 2D and the longer 3D poles respond with similar initial stiffness, while, as expected, the prismatic 2D pole's stiffness was slightly lower. Ironically, the 3D pole's ultimate strength is noticeably lower than both the 2D poles. The 3D pole suffers some damage starting at a load of 195 N, at a tip deflection of 190 mm compared to the 2D poles that seemingly suffer no damage until reaching their

ultimate strength. Tapered and prismatic 2D poles failed at similar deflection values of 537 mm and 551 mm, respectively, while the ultimate deflection of the 3D pole was 482 mm.

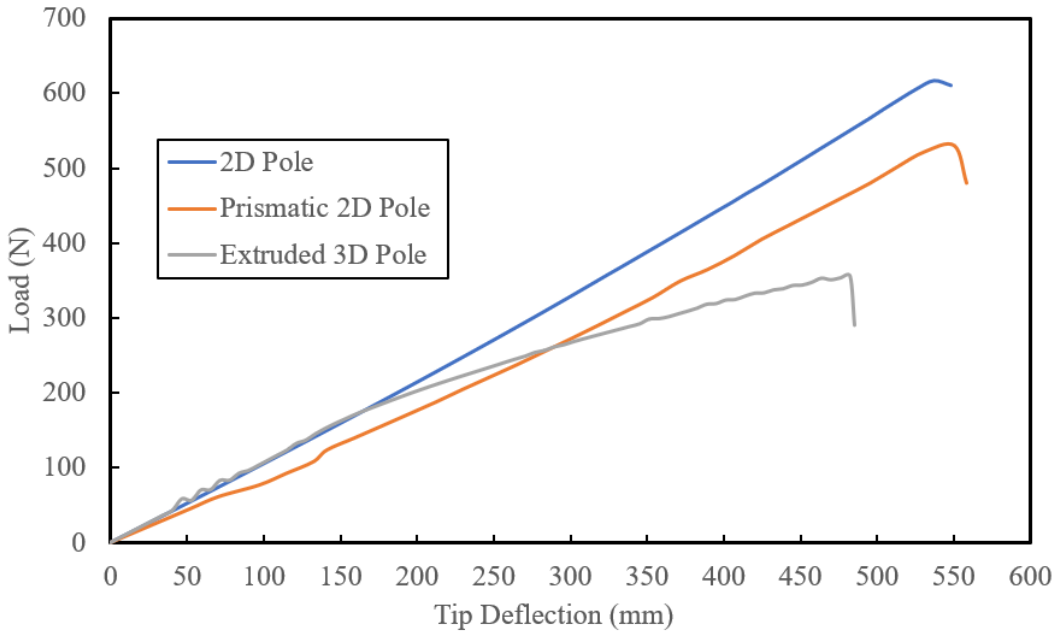

Figure 6-18 Numerically predicted response of equal-length prismatic 2D and 3D and non-prismatic modular 2D poles

The densities of 2D (FRP) and 3D (WC3DFRP) poles were determined using the fundamental mass-to-volume ratio formula with the masses of 2D and 3D poles estimated by taking the tested poles' average masses, as reported in Table 5-2 and Table 5-3, respectively.

The volume of the 3D pole is obtained using SolidWorks and the volume of the prismatic 2D pole is calculated using:

$$V_p = \frac{\pi(D_O^2 - D_i^2)}{4} L \qquad \text{Equation 6-1}$$

where V_p is the volume of the prismatic poles.

The volume of the non-prismatic 2D poles, V_{NP}, can be calculated by using the following equation:

$$V_{NP} = \frac{\pi L}{12}(D_B^2 - d_B^2 + D_B D_T - d_B d_T + D_T^2 - d_T^2) \quad \text{Equation 6-2}$$

where d and D are the inner and outer diameters of the pole, respectively and indices B and T refer to the bottom and top location of the pole, respectively.

Table 6-7 summarizes the calculated physical parameters for the 2D and 3D FE models. As can be seen, the poles are extremely lightweight, weighing less than a kilogram. The 3D WC3DFGF pole has about the same density as the 2D FRP, an advantage facilitated by the empty channels of the 3D fabric.

Table 6-7 Summary of the fundamental physical parameters of the FE models.

	Volume (mm^3)	Mass (g)	Density ($\frac{g}{mm^3}$)
2D Pole	68,6711	760.5	0.0011
2D Prismatic Pole	57,2920	634.5	0.0011
Long prismatic 3D Pole	66,9842	729.2	0.0011

Table 6-8 reports some of the critically important values that signify the performances of the 2D and 3D poles. As can be seen, the 3D pole has a slightly larger normalized stiffness than the two 2D poles. In contrast, the 2D poles exhibit a noticeable superiority over the 3D Pole in terms of their normalized ultimate load-bearing capacity. In fact, the non-prismatic (tapered) and prismatic 2D poles sustained 35.3% and 37.2% more load compared to the 3D pole. This is postulated to be due to the 3D pole's unsupported ply segments (those over the empty channels, as seen in Figure 6-16 (a)), making it more prone to premature comparison governed failure under a flexure load compared to the segments supported by wood dowels and pillars, respectively. It is believed that significant improvement could be attained by stacking a few layers of 2D-FRP on the 3D-FRP to lessen the chance of empty channels buckling. A more cost-effective alternative would be to have a dowel reinforcement inserted in every channel of the 3D fabric. With such a configuration, the pole section can be fully consolidated during its manufacturing process as was done with the 2D poles and generate much stronger and lighter weight 3D poles with faster fabrication and processing speeds. It should be noted that dowel inserts could

be easily automated during the automated manufacturing of the 3D fabric. It is worth noting that the slightly higher normalized load-bearing capacity of the prismatic 2D pole cannot justify one to dismiss the various advantages of the modular design of the non-prismatic pole, as discussed in Chapter 1.

Table 6-8 Comparison of the normalized parameters of the 2D and 3D poles.

Pole type	Stiffness ($N \cdot mm^2$)	Ultimate Load Capacity (N)	Normalized Ultimate Load Capacity (*N/kg*)
Prismatic 2D Pole	1.02E+09	616.0	0.81
Non-prismatic 2D Pole	9.02E+08	530.0	0.84
3D Pole	1.06E+09	355.8	0.49

A simple hand-calculation procedure has been developed to aid practicing engineers in quickly estimating the stiffness of 3D poles without incorporating Equation 4-1. First, the moment of inertia of the 3D pole is calculated as discussed in section 6.2.3. As discussed in section 4.1.2. , the pole's performance is governed by the extensional elastic modulus of its material. Then, one could estimate the extensional modulus of the WC3DFGF, $E_{3D,1}$, in the principal material 1 direction, by considering a representative unit cross-section of the material, as illustrated in Figure 3-6. The established formula is as follows:

$$E_{3D,x} \approx E_{3D,1}(exact) = \frac{2A_{Ply}E_{Ply} + A_{Pillar}E_{Pillar} + A_{Dowel}E_{Dowel}}{2A_{Ply} + 2A_{Pillar} + A_{Dowel}} \qquad \text{Equation 6-3}$$

where A_{Ply}, A_{Pillar} and A_{Dowel} are the total cross-sectional areas of the ply, pillar, dowel and empty channels, respectively; E_{Ply}, E_{Pillar} and E_{Dowel} are the elastic modulus of the plies, pillars and dowels in the principal material direction 1, respectively. By inserting the appropriate material properties as tabulated in Table 3-3, and the corresponding cross-section areas, as shown in Figure 3-6, in Equation 6-3, the value of the extensional elastic modulus, $E_{3D,x}$, is established as 8,686 MPa, which agrees very closely to the experimentally established value as seen in Table 6-9. However, the use of the above equation requires the exact cross-section of the materials. Given the fact that the 3D poles cross-section has several empty channels, calculation of the exact net cross-section area

would be a time-consuming task. However, one can use the gross cross-section are (i.e., the area bounded by the inner and outer ply, which can be easily obtained), in combination with the following equation, yielding the value of extensional elastic modulus, $E_{3D,x}$, of 5,296.0 MPa.

$$E_{3D,x} \approx E_{3D,1}(approx) = \frac{2A_{Ply}E_{Ply} + A_{Pillar}E_{Pillar} + A_{Dowel}E_{Dowel} + A_{air}E_{air}}{2A_{Ply} + 2A_{Pillar} + A_{Dowel} + A_{air}} \qquad \text{Equation 6-4}$$

where and E_{Air} is the elastic modulus of the air in the empty channels (equal to zero) and A_{Air} is the total cross-section area of the empty channels.

It should be noted that the multiplication of this value with the gross cross-section area would yield exactly the same extensional stiffness, AE_x, value as would be obtained by multiplying the exact value of $E_{3D,x}$ (8,682 MPa), by the net cross-section area. Obviously, the use of the net area would significantly exceedances the calculations.

The detailed calculations can be found in Appendix I. The estimated value of 8,682 MPa is compared with the experimentally evaluated modulus obtained from the compression test in Table 6-9.

Table 6-9 Comparison of experimental Young's modulus and those predicted by the established formula.

	Extensional elastic modulus (MPa)	Stiffness ($N \cdot mm^2$)	% Error in Stiffness
Experimental value (Compression Test)	8,963.5	152,208	
Equation 6-3	8,682.0	152,058	0.03
Equation 6-4	5,296.0	152,058	

As stated earlier, the actual 3D pole ply thickness was evaluated to be 0.3 mm thick as opposed to the 0.4 ply thickness in the dry fabric (i.e., Figure 3-6). Therefore, the 3D poles E_x was evaluated using Equation 6-3 as 8,682 MPa, which is 10.7% higher than the experimentally obtained value, as reported in Table 6-5. It should be noted that the numerically predicted maximum deflection at failure was only about 10% lower than the actual experimentally observed deflection. Therefore, one can appreciate that one can

easily use Equation 6-4 combined with the gross cross-section area of the pole in conjunction with mechanics or materials equations to predict the deflection of such complex poles without resorting to time-consuming numerical (FEM) analysis.

Equation 6-4, can be further simplified for the 4 mm nominal thick ply used in this study, considering that parameters related to the 3DFRP are constant and the only variable would be the dowel's elastic modulus as an unknown. Therefore, the following simplified equation could be used instead of the more elaborate version, Equation 6-3.

$$E_{3D,x} = 3562.2 + 0.45E_{dowel} \qquad \text{Equation 6-5}$$

It is worth noting that Equation 6-5 is applicable only to the configuration that was considered in this study; however, the simplified procedure can be tuned for any fabric thickness or pole cross-section configuration.

Chapter 7: Conclusion and Recommendations

7.1. Summary and Conclusions

This thesis focused on the development of a new utility pole made of a novel combination of 3D glass fabric-epoxy composite reinforced with wood dowels, referred to as wood dowel-reinforced 3D hybrid composite (WC3DFRP). The objective was to develop a pole that could perform comparably to the conventional and commercially available modular 2D FRP poles with higher stiffness at the same cost or even less expensive overall cost. The performances of 2D modular poles and 3D poles were experimentally investigated under a laterally applied bending load, which is a standard primary test used for validating the stiffness, strength and integrity of such poles. The standardized flexural and compression tests conducted on WC3DFRP coupons indicated that the WC3DFRP's stiffness and strength were significantly superior to its non-dowel-reinforced base 3DFRP composite (by as much as 300% and 500%, respectively). Experimental results revealed a difference of 13% between the flexural modulus and compressive modulus (10.3 and 8.9 GPa, respectively). Additionally, robust finite element models were constructed with their input mechanical properties calibrated based on the experimental results. The models were proven to be accurate and reliable, thus, could be confidently used to examine the influence of different materials combinations.

The development of the scaled 2D poles started by optimizing the layup stacking sequence of its laminate subjected to bending through finite element analyses conducted using two commercially available finite element software, NISA and LS-DYNA. The optimization results obtained through NISA OPT (the optimization module of NISA), indicated that the optimum pole design could be attained by a laminate consisting of uniaxial laminae laid along the pole's axial direction. Since a purely uniaxial pole would not perform reliably when other factors such as axial loads, fatigue and environmental loadings are considered, therefore, the performance of poles having various stacking sequences was further examined using LS-DYNA FE software. The analysis results showed that the optimized designs would be achieved by either $[+/0_9/+]$ or $[90/0_{11}/90]$ layup sequences. In summary, both NISA and LS-DYNA results indicated the dominant

role of the extensional stiffness of the material in the pole's bending performance. Subsequently, the performances of models constructed with solid and Tshell elements of LS-DYNA were examined, and the results were compared against the theoretical solutions to establish the computational efficiency for future more demanding combined loading analyses. The Tshell constructed model showed a larger discrepancy (15.5%) in evaluating the maximum flexural stress against the theoretical solution compared to the model built using the solid elements (with a 3.2% discrepancy); however, the Tshell model revealed a 3,856% saving in CPU time over its counterpart model. Hence, Tshell element was used to construct the two poles model for further investigations.

The development methods of both the 3D and 2D poles were also presented. Two modular tapered 2D poles with 1485 mm in length and two prismatic 3D poles with 1005 mm in length were fabricated using the hand-layup process and were tested under bending in a cantilever configuration. The results of the tests were used to calibrate the FE models so that the performances of equal-length 2D and 3D (made of WC3DFRP) could be evaluated numerically. The numerical results revealed that while the extruded 3D pole exhibited higher stiffness (i.e., 1.06E+09N·mm^2) compared to the 2D pole, it exhibited lower normalized loading capacity (0.52 N/kg) (355.8 N and 616 N for the 3D and 2D poles, respectively). The lower loading capacity is attributed to the unsupported ply segments, which are prone to premature failure under bending.

Finally, a hand-calculation procedure was established for quickly estimating the stiffness of the 3D pole without going through complicated FE analysis. The estimated extensional elastic modulus (8.69 GPa) was only 3.1% less than the results produced by the compression test (i.e., 8.96 GPa).

In closing, the results of the research indicate that the developed 3D pole is promising, especially when other loading types which would cause the pole response to be more stiffness governed (such as axially applied dynamic loading states) are considered. Therefore, further investigations would be required.

7.2. Recommendations for Future Works

The hybrid 3D material system introduced in this thesis is in its infancy. Consequently, its database and performance measurement are quite limited, and further studies should be conducted to expand the database. These studies should focus on different types of loading and environmental conditions to achieve a comprehensive understanding of the material's response. A series of recommendations are therefore offered in this section, which aims to further improve the overall response of poles made of such lightweight and stiff hybrid material.

- As stated, utility poles become subjected to combined axial and lateral loadings as a result of their wiring connection and the consequence of guy wires used for their stability. Such combined loading will induce significant compressive axial load on the column, which in turn may cause premature buckling of a comparable 2D column as opposed to a 3D column having comparatively stiffer material. Besides, wind and hurricanes would cause the vibration of the poles. The vibration could significantly benefit from the significant stiffness and more importantly, the damping characteristics of WC3DFRP. The result of such investigation is strongly believed to justify and promote the use of the developed material for manufacturing lightweight and resilient poles.
- The above critical states could be further exasperated due to fatigue, and environmental loading states. Therefore, additional experiments would have to be performed to further explore the structural responses of 3D poles under such combined loading states.
- It is believed lightweight hollow plastic profiles would be as light (or lighter than) wood dowels with the potential of making the pole perform more resiliently. Therefore, attempts should be made to explore the viability of such alternative reinforcing inserts.
- Further improvement in the performance of 3D poles could be attained by supporting the empty channels in WC3DFRP to prevent premature failure. An optimal alternative is believed to be achieved by the insertion of a dowel in every channel of the 3D fabric. This could be effectively done during the manufacturing (weaving) of the fabric.
- Moreover, the implementation of additional layers of 2D FRP to the 3DFGF could also be attempted to explore the gain in the strength and stability of the empty channels.
- Finally, as stated, the reinforced inserted fabric could be produced using an automated weaving process. Successful attempts have already been made to manufacture integral

foam 3D fabric. Moreover, it is believed that instead of the hand-lay-up process used in this investigation, the entire pole manufacturing process could feasibly be automated. This can be facilitated by automated manufacturing of reinforcement-inserted 3D prepreg fabric, making the rolling process easier and at a much faster speed. Moreover, the prepreg nature of the fabric will further enhance the response and consolidation of such poles by preventing fiber misalignment and reducing the presence of voids in the composite.

Bibliography

AISC. (1994). *Load and Resistance Factor Design Specification for Structural Steel Buildings* (Second, Vol. 2). https://www.oaxaca.gob.mx/sinfra/wp-content/uploads/sites/14/2016/02/manual_of_steel_construction-load_and_resistance_factor_design-2nd_edition.pdf

Al-Falah, S. C., Chaturvedi, S. K., & Kumar, S. (2014). Evaluation of Thermal Properties of E-Glass/Epoxy Composites Filled by Different Filler Materials. *International Journal of Advances in Engineering & Scientific Research*, *1*(3), 1–07. http://www.arseam.com/content/volume-1-issue-2-june-2014-0

ALT composite Pty Ltd. (n.d.). *Reinforcements NCF E-Glass /Biaxial 0/90*. Retrieved March 29, 2023, from https://atlcomposites.com.au/icart/products/102/images/main/Biaxial.pdf

Altanopoulos, T. I., Raftoyiannis, I. G., & Polyzois, D. (2021). Finite element method for the static behavior of tapered poles made of glass fiber reinforced polymer. *Mechanics of Advanced Materials and Structures*, *28*(20), 2141–2150. https://doi.org/10.1080/15376494.2020.1717691

ANSI. (2019). *Standard Specification for FRP Composite Utility Poles* (1st ed.). American National Standards Institute.

ASCE. (2019). Recommended practice for fiber-reinforced polymer products for overhead utility line structures. In Galen Fecht (Ed.), *Recommended Practice for Fiber-Reinforced Polymer Products for Overhead Utility Line Structures* (2nd ed.). American Society of Civil Engineers (ASCE). https://doi.org/10.1061/9780784415443

ASTM. (2017). *Static Tests of Wood Poles*. American National Standards Institute.

ASTM Standards. (2015). *Standard Test Method for Flexural Properties of Polymer Matrix Composite Materials: Vol. 15.03* (2015th ed.). ASTM International. https://doi.org/10.1520/D7264_D7264M-21

ASTM Standards. (2017). Standard Test Method for Compressive Properties of Polymer Matrix Composite Materials Using a Combined Loading Compression (CLC) Test Fixture: Vol. 15.03. ASTM International. https://doi.org/10.1520/D6641_D6641M-16

Chen, Y., Yang, J., Wang, F., & Peng, J. (2022). Short beam shear damage analysis of GLARE laminates based on digital image correlation and finite element analysis. *International Journal of Damage Mechanics*, *31*(4), 623–642. https://doi.org/10.1177/10567895211056679/ASSET/IMAGES/LARGE/10.1177_10567895211056679-FIG20.JPEG

China Beihai Fiberglass Co., Ltd. (n.d.). *3D Fiberglass Woven Fabric*. Retrieved April 21, 2023, from https://www.fiberglassfiber.com/3d-fiberglass-woven-fabric-product/

CSA. (2015). *Wood utility poles and reinforcing stubs* (4th ed.). Canadian Standard Association. https://www.csagroup.org/store/product/2700529/

CSA. (2020). *Overhead systems C22.3* (CSA, Ed.). National Standard of Canada.

Daniel, I. M., & Ishai, O. (2005). *Engineering Mechanics of Composite Materials* (2nd ed.). Oxford University Press, Inc. https://global.oup.com/academic/product/engineering-mechanics-of-composite-materials-9780195150971?cc=ca&lang=en&#

Ekşi, S., & Genel, K. (2017). *Comparison of Mechanical Properties of Unidirectional and Woven Carbon, Glass and Aramid Fiber Reinforced Epoxy Composites*. Acta Physica Polonica A 132. https://doi.org/10.12693/APhysPolA.132.879

EL-Fiky, A. M., Awad, Y. A., Elhegazy, H. M., Hasan, M. G., Abdel-Latif, I., Ebid, A. M., & Khalaf, M. A. (2022). FRP Poles: A State-of-the-Art-Review of Manufacturing, Testing, and Modeling. *Buildings*, *12*(8). https://doi.org/10.3390/buildings12081085

Forest Service, U., & Products Laboratory, F. (2010). *Wood Handbook, Wood as an Engineering Material*. www.fpl.fs.fed.us.

Hibbeler, R. C. (2016). *Mechanics of Materials* (10th ed.). Pearson.

Ibrahim, S. M. (2000). *Performance Evaluation of Fiber-Reinforced Polymer Poles For Transmission Lines* [Doctor of Philosophy, The University of Manitoba]. https://www.collectionscanada.gc.ca/obj/s4/f2/dsk1/tape3/PQDD_0025/NQ51638.pdf

Jackson, E. (2012, June 2). *Wood Utility Poles and Preservative Choices | Utility Products*. Utility Products. https://www.utilityproducts.com/line-construction-maintenance/article/16002743/wood-utility-poles-and-preservative-choices

Love, L., Post, B., Tekinalp, H., Wang, P., Atkins, C., Xianhui, A. R., Zhao, A., & Rencheck, M. (2021). *Assessment of Commercial Composite Power Pole Performance*. http://www.osti.gov/scitech/

Lu, K., Wang, Y., Gu, F., Pang, X., & Ball, A. (2019). Dynamic modeling and chatter analysis of a spindle-workpiece-tailstock system for the turning of flexible parts. *International Journal of Advanced Manufacturing Technology*, *104*(5–8), 3007–3015. https://doi.org/10.1007/S00170-019-04224-W/FIGURES/10

Ma, Q., Kumar, N. M., Quanjin, M., Rejab, R. M., & Zhang, B. (2019). Filament winding technique: SWOT analysis and applied favorable factors. *SCIREA Journal of Mechanical Engineering*, *3*(1). http://www.scirea.org/journal/Mechanical

MacDonald, M., & Alam, H. (2022, October 5). Prolonged power outages in Nova Scotia and P.E.I. leaving residents exasperated | Globalnews.ca. *The Canadian Press*. https://globalnews.ca/news/9178114/prolonged-power-outages-nova-scotia/

Mankowski, M., Hansen, E., & Morrell, J. (2002). Wood pole purchasing, inspection, and maintenance: A survey of utility practices - ProQuest. *Forest Products Journal*, *52*(11), 43–50. https://www.proquest.com/docview/214640466/fulltext/2DB38A6A439A4974PQ/1?accountid=10406

Mazumdar, S. K. (2002). *Composites Manufacturing : Materials, Product, and Process Engineering* (1st ed.). CRC Press, Boca Raton, Florida.

McClearn, M. (2023, January 29). Climate-minded electrical companies look to improve their weakest link: the wooden utility pole - The Globe and Mail. *The Globe and Mail*. https://www.theglobeandmail.com/canada/article-climate-change-lectricity-utility-poles/

Mognhod, B. Y., Paramasivam, V., Tilahun, S., & Selvaraj, S. K. (2021). A review on failure mechanisms and analysis of multidirectional laminates. *Materials Today: Proceedings*, *46*, 7380–7388. https://doi.org/10.1016/J.MATPR.2020.12.1121

Mohamed, M., & Taheri, F. (2017). Influence of graphene nanoplatelets (GNPs) on mode I fracture toughness of an epoxy adhesive under thermal fatigue. *Journal of dhesion Science and Technology*, *31*, 2105–2123. https://doi.org/10.1080/01694243.2016.1264659

Morrell, J. J. (2012). *Wood Pole Maintenance Manual: 2012 edition*. www.forestry.oregonstate.edu/

Morrell, J. J., Freitag, C., Chen, H., & Love, C. (2007). *Oregon State University Utility Pole Research Cooperative 27th Annual Report*. https://utilpole.forestry.oregonstate.edu/system/files/publicfiles/Annual%20Report%202007.pdf

Murray, J., & Sipler, B. (n.d.). *What is an "Attachment"? ... that's easy!* [PowrPoint Slides] Oregon Public Utility Commission. Retrieved April 8, 2023, from https://www.ojua.org/wp-content/uploads/2018/09/WhatsAnAttachmentPresentation.pdf

NATIONAL INSTRUMENTS CORP. (2022). *Connecting Strain Gauges and Shunt Resistors to the NI-9237*. https://knowledge.ni.com/KnowledgeArticleDetails?id=kA00Z000000PA73SAG&l=en-CA

North American Wood Pole Council. (n.d.). *How Wood Utility Poles Are Made*. Retrieved April 3, 2023, from https://woodpoles.org/Why-Wood-Poles/How-Poles-Are-Made

Palucka, T., & Bensaude-Vincent, B. (2002, October 19). *History of composites - overview*. https://authors.library.caltech.edu/5456/1/hrst.mit.edu/hrs/materials/public/composites/Composites_Overview.htm

Polymershapes. (n.d.). *ABS (Acrylonitrile Butadiene Styrene) Plastic Products*. Retrieved March 7, 2023, from https://www.polymershapes.com/product/abs/

Rey, J., & Morrell, J. (2016). *Estimated Service Life of Wood Poles*. https://woodpoles.org/portals/2/documents/TB_ServiceLife.pdf

Riedel, U. (2012). Biocomposites: Long Natural Fiber-Reinforced Biopolymers. *Polymer Science: A Comprehensive Reference: Volume 1-10*, *1–10*, 295–315. https://doi.org/10.1016/B978-0-444-53349-4.00268-5

Road, S. (2013). *A 575/ A 575 RC Data Sheet Polyester shrink tape*. www.airtechonline.com

RS Technologies Inc. (n.d.). *RS PowerON™ Modular Poles Brochure*. Retrieved April 5, 2023, from https://www.rspoles.com/resources/literature

VYCOM. (n.d.). *Typical Physical Properties: Vintec I*. Retrieved March 7, 2023, from https://www.polymershapes.com/wp-content/uploads/2020/04/Polymershapes_Vycom_Data-Sheet-Vintec-I.pdf

WEST SYSTEM. (2014). *05 Epoxy Resin® / 206 Slow Hardener®*. https://www.westsystem.com/wp-content/uploads/105-206-Epoxy-Resin-1.pdf

Ye, J., & Zhang, D. (2012). Prediction of failure envelopes and stress–strain curves of fiber composite laminates under triaxial loads. *Journal of Composite Materials*, *46*(19–20), 2417–2430. https://doi.org/10.1177/0021998312449678

Appendix A Calculation of overlap length

$$overlap\ length = L - \frac{t}{\tan(\theta)}$$

where L=880mm, t=2.6mm, θ=0.2°.

$$overlap\ length = 880 - \frac{2.6}{\tan(0.2°)} = 135.2mm$$

Appendix B Calculations of upper diameter, D_T, of modular pole

For each module

$$D_T = D_B - 2L\,tan(\theta)$$

for the top module: D_B=54.2mm, L=1000mm, θ=0.2°.

$$D_T = 54.2 - 2 \times 1000 \times tan(0.2°) = 47.2mm$$

for bottom modulus: D_B=54.2mm, L=880mm, θ=0.2°.

$$D_T = 54.2 - 2 \times 880 \times tan(0.2°) = 48.1mm$$

Appendix C Calculation of pole's taper

$$Taper = \frac{(D_B - D_T) \times 1000}{L}$$

for top module D_B=54.2mm, D_T=47.2mm, L=1000mm

$$Taper = \frac{(54.2 - 47.2) \times 1000}{1000} = 7mm$$

for bottom module D_B=54.2mm, D_T=48.1mm, L=880mm

$$Taper = \frac{(54.2 - 48.1) \times 1000}{880} = 6.9mm$$

Appendix D CAD drawing of the load transfer knob

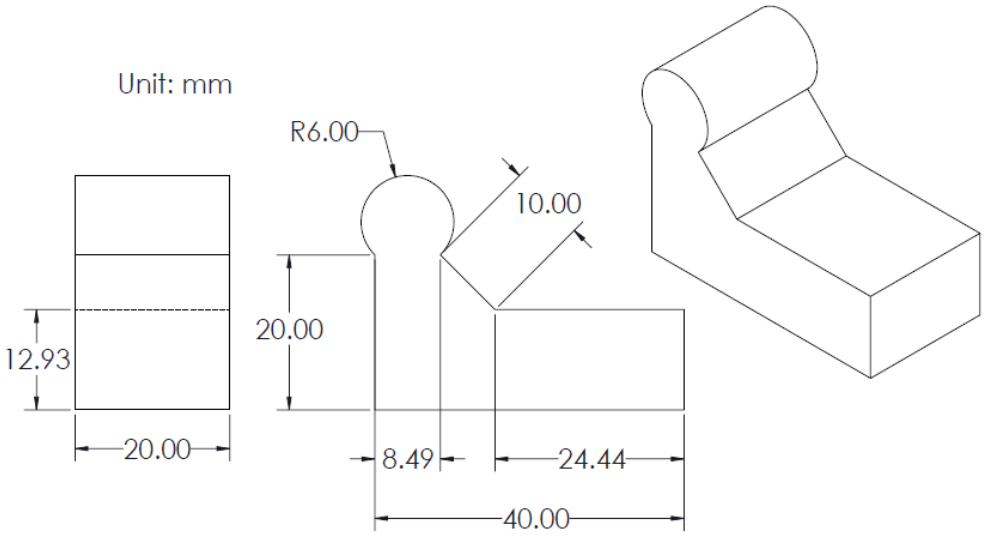

Figure D-1 CAD drawing of load transfer knob.

Appendix E Complete wiring configuration for quarter-bridge strain gauge using NI 9944 and NI 9237

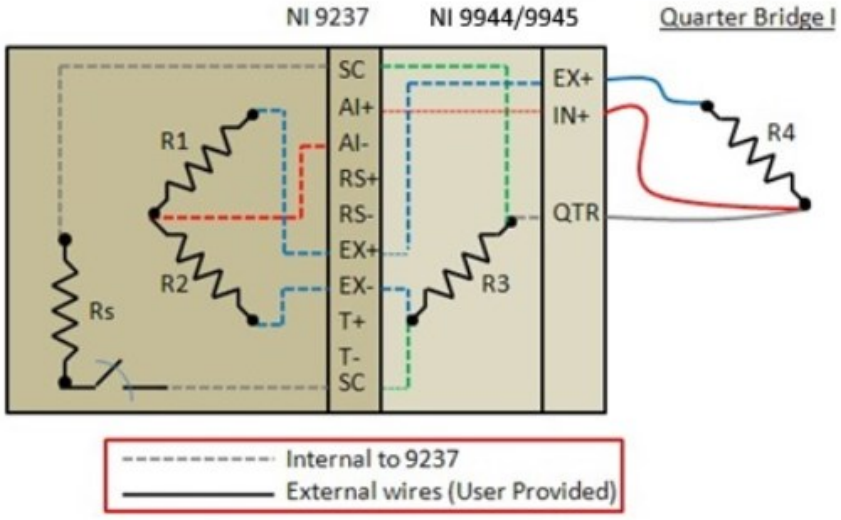

Figure E-1 Wiring configuration for a quarter-bridge strain gauge (NATIONAL INSTRUMENTS CORP., 2022).

Appendix F Complete wiring configuration for full-bridge load cell

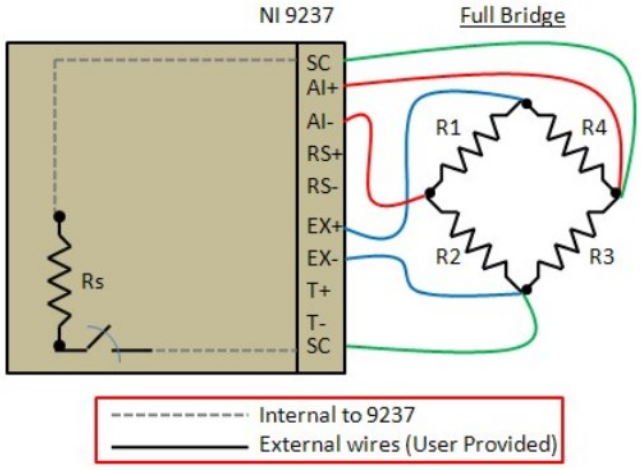

Figure F-1 Wiring configuration for the load cell (NATIONAL INSTRUMENTS CORP., 2022).

Appendix G Flowchart of the LabView program

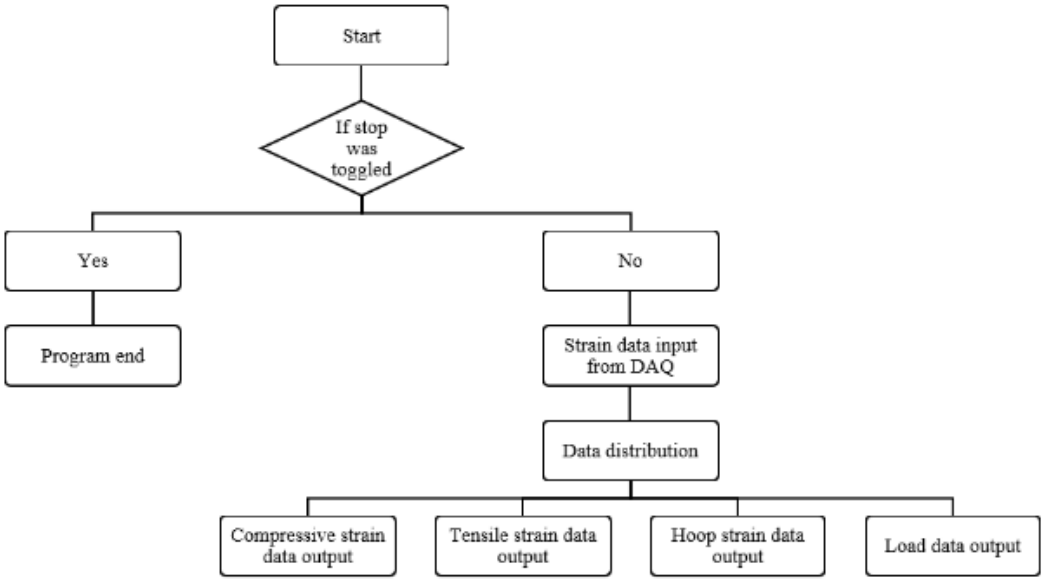

Figure G-1 Flowchart of the LabView program for data acquisition.

Appendix H Flowchart of the Python program

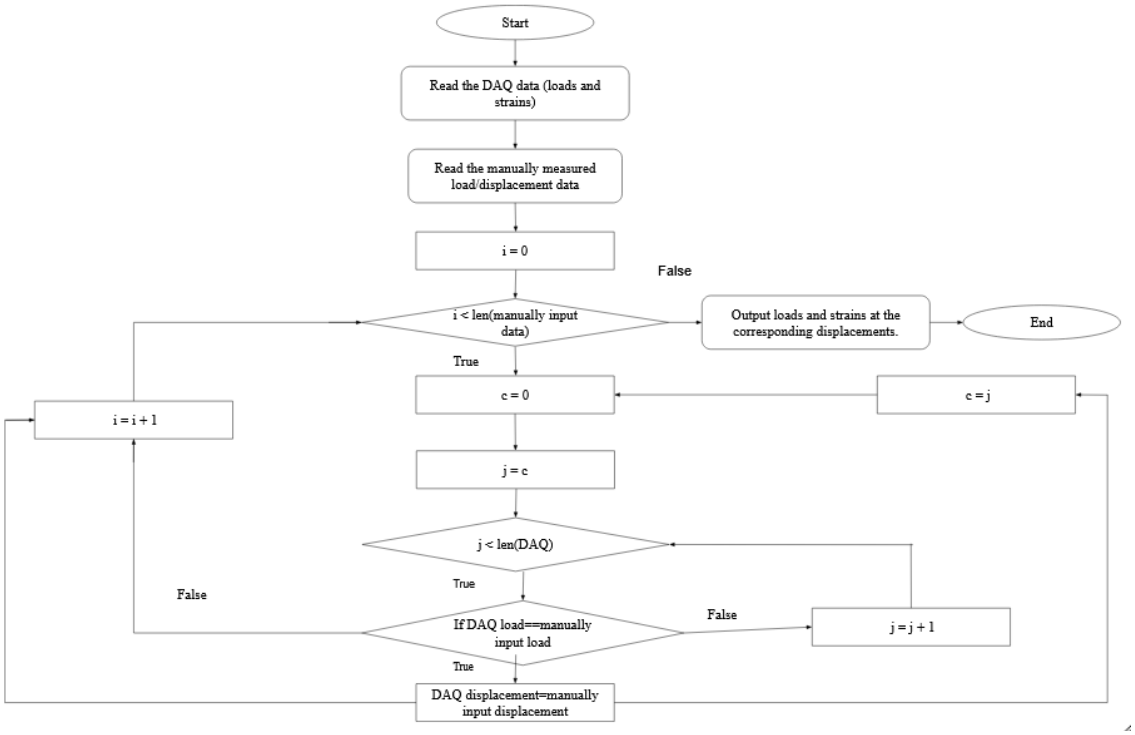

Figure H-1 Flowchart for post-processing data obtained from the DAQ.

Appendix I Calculation of extensional elastic modulus using Equation 6-3 and Equation 6-4

Equation 6-3:

$$E_{3D,x} = \frac{2A_{Ply}E_{Ply} + A_{Pillar}E_{Pillar} + A_{Dowel}E_{Dowel}}{2A_{Ply} + 2A_{Pillar} + A_{Dowel}}$$

where $E_{Ply} = 9000$Mpa, E_{Pillar}=1500Mpa, E_{Dowel}=11330Mpa

Equation 6-4:

$$E_{3D,x} = \frac{2A_{Ply}E_{Ply} + A_{Pillar}E_{Pillar} + A_{Dowel}E_{Dowel} + A_{Air}E_{Air}}{2A_{Ply} + 2A_{Pillar} + A_{Dowel} + A_{Air}}$$

where $E_{Air} = 0$Mpa

The area for each component is calculated based on the geometric dimensions of the unit cell shown in Figure I-1.

$$A_{Ply} = 0.4 \times 8 = 3.2mm^2$$

$$E_{Ply} = 3.2 \times 0.5 = 1.6mm^2$$

$$A_{Dowel} = A_{Air} = 3.5 \times 3.2 = 11.2$$

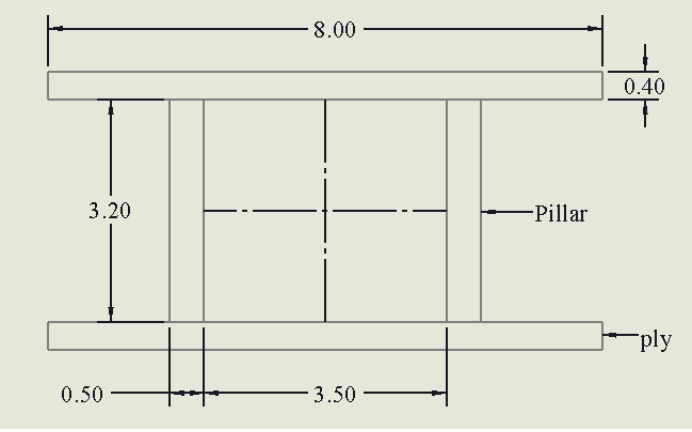

Figure I-1 The dimensions of the 3D fabric unit cell used in the numerical model.

For Equation 6-3:

$$E_{3D,x} = \frac{2 \times 3.2 \times 9000 + 3.2 \times 1500 + (\frac{3.175}{2})^2 \times 3.14 \times 11330}{2 \times 3.2 + 3.2 + (\frac{3.175}{2})^2 \times 3.14} = 8682Mpa$$

For Equation 6-4:

$$E_{3D,x} = \frac{2 \times 3.2 \times 9000 + 3.2 \times 1500 + (\frac{3.175}{2})^2 \times 3.14 \times 11330 + 11.2 \times 0}{2 \times 3.2 + 3.2 + (\frac{3.175}{2})^2 \times 3.14 + 11.2} = 5296Mpa$$